

Electronic Thesis and Dissertation Repository

11-30-2018 2:00 PM

Propane Oxidative Dehydrogenation Under Oxygen-free Conditions Using Novel Fluidizable Catalysts: Reactivity, Kinetic Modeling and Simulation Study

Samira Rostom
The University of Western Ontario

Supervisor
Hugo I. de Lasa
The University of Western Ontario

Graduate Program in Chemical and Biochemical Engineering
A thesis submitted in partial fulfillment of the requirements for the degree in Doctor of Philosophy
© Samira Rostom 2018

Follow this and additional works at: <https://ir.lib.uwo.ca/etd>

 Part of the [Catalysis and Reaction Engineering Commons](#)

Recommended Citation

Rostom, Samira, "Propane Oxidative Dehydrogenation Under Oxygen-free Conditions Using Novel Fluidizable Catalysts: Reactivity, Kinetic Modeling and Simulation Study" (2018). *Electronic Thesis and Dissertation Repository*. 5875.
<https://ir.lib.uwo.ca/etd/5875>

This Dissertation/Thesis is brought to you for free and open access by Scholarship@Western. It has been accepted for inclusion in Electronic Thesis and Dissertation Repository by an authorized administrator of Scholarship@Western. For more information, please contact wlsadmin@uwo.ca.

Abstract

Propane oxidative dehydrogenation (PODH) was studied using $\text{VO}_x/\gamma\text{Al}_2\text{O}_3$ and $\text{VO}_x/\text{ZrO}_2-\gamma\text{Al}_2\text{O}_3$ (1:1 wt. %) catalysts, as well as consecutive propane injections under oxygen-free conditions. These catalysts were synthesized with 2.5, 5 and 7.5 wt. % vanadium loadings, and prepared using a wet saturation impregnation technique. Different characterization techniques were used to establish catalyst properties including NH_3 -TPD, pyridine FTIR and NH_3 -TPD kinetics. As well, PODH runs in the CREC Riser Simulator were developed under oxygen free atmospheres at 500-550°C, close to 1 atm., 10-20 s and 44.0 catalyst/propane weight ratio (g/g). Propylene selectivity obtained were up to 94%, at 25% propane conversion.

Using this data, a “parallel-series” model was established based on a Langmuir-Hinshelwood rate equation. Adsorption constants were defined independently, with this leading to a 6-independent intrinsic kinetic parameter model. These parameters were calculated via numerical regression with reduced spans, for the 95% confidence interval and low cross-correlation coefficients. A larger $2.82 \times 10^{-5} \text{ mol.gcat}^{-1}\text{s}^{-1}$ frequency factor for propylene formation versus the $1.65 \times 10^{-6} \text{ mol.gcat}^{-1}\text{s}^{-1}$ frequency factor for propane combustion was obtained. The calculated energies of activation (55.7 kJ/mole for propylene formation and 33.3 kJ/mole for propane combustion) appeared to moderate this effect, with the influence of frequency factors prevailing. Furthermore, propylene conversion in CO_x oxidation appeared as a non-favoured reaction step, given the 98.5 kJ/mole activation energy and $4.80 \times 10^{-6} \text{ mol.gcat}^{-1}\text{s}^{-1}$ frequency factor.

This kinetic model was considered for the development of a scaled-up twin fluidized bed reactor configuration. For this, a hybrid computational particle-fluid dynamic (CPFD) model featuring either “Particle Clusters” or “Single Particles” was employed. Results obtained in a 20-m length downer unit showing a 28% propane total conversion and a 93% propylene selectivity using the “Single Particle” model. However, and once the more rigorous particle cluster flow was accounted for, propane conversion was limited to 20%, with propylene selectivity staying at 94% level. Thus, the obtained results show that a PODH simulation using CPFD requires one to account for “Particle Clusters”. This type of comprehensive model is needed to establish unambiguously the PODH downer reactor performance, being of critical value for the development of downflow reactors for other catalytic processes.

Keywords: Propane Oxidative Dehydrogenation, Propylene, Selectivity, Vanadium Oxide, Lattice Oxygen, Successive Injection, CREC Riser Simulator, Kinetic Modeling, Simulation.

Dedication

This dissertation is dedicated to:

My Father (Md. Rostom Ali)

And

My Mother (Shaheen Afroz)

(উৎসর্গ করলাম আমার আবু ও আম্মু কে)

Acknowledgements

I would like to thank to the Almighty Allah who has blessed me and gave me the opportunity, strength, courage and patience to finish my PhD.

I owe much gratitude to my supervisor Dr. Hugo de Lasa who gave me this opportunity to join his group and work on an interesting project. His knowledge, experiences, guidance and encouraging discussions made this study successful.

I gratefully acknowledge the contribution of the Natural Sciences and Engineering Research Council of Canada who supported this research financially. Also my thanks go to Florencia de Lasa for helping me in the editing of the final version of my all publications.

My appreciations go to my colleagues at CREC, for their inspirations during my hard time. My sincere gratitude goes to Jose Munoz and Pastor Solano from CREC Lab, for their valuable technical support. I am especially thankful and indebted to Imtiaz Ahmed, my husband and also my colleague, who was always with me and provided support through fruitful technical discussion. His love, patience, understanding and care allowed me to finish this journey smoothly.

Last but not least, my deep gratitude and appreciation go to my family members in Bangladesh for their sincere prayers, support and encouragement. May Almighty Allah bless them all.

Table of Contents

Abstract	ii
Acknowledgements	v
List of Figures	x
List of Tables	xiii
Nomenclatures	xiv
Chapter 1: Introduction	1
1.1 Propylene Demand	1
1.2 Traditional Processes for Propylene Productions	1
1.3 Oxidative Dehydrogenation (ODH) Process	2
1.3.1 ODH with Molecular Oxygen.....	2
1.3.2 ODH with Mild Oxidants.....	3
1.3.3 ODH with Catalyst's Lattice Oxygen.....	4
Chapter 2: Literature Review on Propane Oxidative Dehydrogenation under Gas Phase	
Oxygen-free Conditions	5
2.1 Thermodynamics Study	5
2.2 Vanadium-Based Catalyst Development for Propane ODH	9
2.2.1 VO _x Surface Coverage	10
2.2.2 Active Lattice Oxygen Species	11
2.2.3 Effect of Support (Acid/Base Properties)	11
2.2.4 Red-Ox Properties of Supported VO _x Catalysts	12
2.2.5 Vanadium-based Propane ODH Catalysts under Oxygen-free Atmosphere	13
2.3 Kinetics and Reaction Mechanisms of Propane ODH over Vanadium-based Catalysts	14
2.4 Reactor Concepts for ODH	16
2.4.1 Fixed-bed Reactors	16

2.4.2	Twin Circulating Fluidized-bed Reactors for PODH	17
2.4.3	Circulating Fluidized-bed Reactors Models for PODH.....	17
2.4.4	Experimental Laboratory Reactor for PODH	18
2.5	PODH Industrial Prospects	19
2.6	Computational Particle Fluid Dynamic Study for Propane ODH Process	20
2.7	Conclusions	22
Chapter 3: Scope of Research		24
3.1	Objectives	24
3.2	Accomplishments of Research Objectives	25
Chapter 4: Experimental Methods and Apparatus		26
4.1	Catalysts Preparation	26
4.2	Catalyst Characterizations	27
4.2.1	Brunauer–Emmett–Teller (BET) Surface Area.....	27
4.2.2	X-ray Diffraction (XRD)	27
4.2.3	Temperature-Programmed Reduction (TPR).....	27
4.2.4	Temperature-Programmed Desorption of Ammonia (NH ₃ -TPD)	27
4.2.5	Pyridine Fourier Transform Infrared Spectroscopy (FTIR).....	28
4.2.6	Laser Raman Spectroscopy (LRS).....	28
4.2.7	X-ray Photoelectron Spectroscopy (XPS)	28
4.3	PODH Catalytic Test	29
4.3.1	Experimental Apparatus.....	29
4.3.2	Experimental Procedures	31
4.3.3	Thermal Runs	32
4.3.4	Analytical System	32
4.3.5	Conversion and Selectivity Calculations	33

4.4	Conclusions	33
Chapter 5: Results and Discussion of the Experiments		34
5.1	Catalyst Characterizations	34
5.1.1	BET Surface Area	34
5.1.2	XRD	37
5.1.3	H ₂ -TPR and Degree of Reduction	39
5.1.4	NH ₃ -TPD	42
5.1.5	Pyridine FTIR	45
5.1.6	Laser Raman Spectroscopy	46
5.1.7	X-Ray Photoelectron Spectroscopy (XPS)	47
5.2	TPD Kinetics and Heat of Desorption	49
5.3	PODH in the CREC Riser Simulator	52
5.3.1	Thermal Runs	53
5.3.2	Consecutive Propane Injections in PODH Experiments	54
5.4	Conclusions	64
Chapter 6: Kinetic Modeling		66
6.1	Kinetic Model Development	67
6.2	Kinetic Modeling in the CREC Riser Simulator	70
6.3	Estimation of Kinetic Parameters	72
6.4	Conclusions	77
Chapter 7: CPFDP Simulation of the PODH Process		78
7.1	Catalysts Used	78
7.2	Computational Particle Fluid Dynamic (CPFDP) Modeling	79
7.2.1	CPFDP Model Description	79
7.2.2	Numerical Set-up and Simulation Conditions	81

7.2.3	Drag Model Used	86
7.2.4	Chemical Reactions	87
7.3	Results and Discussion	87
7.3.1	Mesh and Discrete Time Selection and Model Validation	87
7.3.2	Entry and Exit Cyclones in the Downer Model	88
7.3.3	Radial Velocity and Solid Concentration Profiles in Downer with Entry and Exit Cyclones	91
7.3.4	Particle Cluster and Gas Flows and PODH in a Downer Reactor	94
7.3.5	Temperature Changes due to Reactions.....	97
7.3.6	Downer Simulation Results with the “Single Particle” Model.....	99
7.4	Conclusions	102
Chapter 8: Conclusions and Recommendations		103
8.1	Conclusions	103
8.2	Recommendations	105
9	Appendices	123
9.1	Appendix A: GC Calibration Curves	123
9.2	Appendix B: Conversion and Products Distribution Results	126
9.3	Appendix C: Internal and External Mass Transfer Limitations	127
9.4	Appendix D: Adsorption Constant Calculation	130
9.5	Appendix E: Grid Discretization Analysis	132
9.6	Appendix F: Gas and Particle Cluster Flow in Entry and Exit Cyclones	133
9.7	Appendix G: Copyright/Permission from Journals	134
Curriculum Vitae		137

List of Figures

Figure 1: Chemical Equilibrium Constant as a Function of Temperature for Propane ODH under an O ₂ -Free Atmosphere. Total pressure: 1 atmosphere.	8
Figure 2: (a) Isolated VO ₄ species on support (s); (b) Polymeric VO ₄ species on support (s).	11
Figure 3: Schematic PODH Process Flow Sheet ⁵⁹ . The process components inside the red marked section are considered in the simulation study (Details in Chapter 7).	22
Figure 4: Schematic diagram of CREC Riser Simulator reactor system ⁵⁹	30
Figure 5: Schematic of GC column connections.	32
Figure 6: N ₂ Adsorption-desorption isotherms for VO _x /γAl ₂ O ₃ catalysts.	34
Figure 7: N ₂ Adsorption-desorption isotherms for VO _x /ZrO ₂ -γAl ₂ O ₃ catalysts.	34
Figure 8: Pore Size Distribution of the γAl ₂ O ₃ Support and the VO _x /γAl ₂ O ₃ Catalyst Samples as determined from Nitrogen Desorption Isotherms.	36
Figure 9: Pore Size Distribution of the γAl ₂ O ₃ and ZrO ₂ -γAl ₂ O ₃ Supports and the VO _x /ZrO ₂ -γAl ₂ O ₃ Catalyst Samples as Determined from Nitrogen Desorption Isotherms.	36
Figure 10: XRD patterns for the γAl ₂ O ₃ and the ZrO ₂ - γAl ₂ O ₃ supports as well as those for the VO _x /ZrO ₂ -γAl ₂ O ₃ catalysts with different vanadium loadings.	37
Figure 11: XRD patterns for the spent VO _x /γAl ₂ O ₃ catalysts with different vanadium loadings after 10 consecutive propane injections.	38
Figure 12: XRD patterns for the spent VO _x /ZrO ₂ -γAl ₂ O ₃ catalysts with different vanadium loadings after 10 consecutive propane injections.	38
Figure 13: H ₂ -TPR profile of calcined VO _x /γAl ₂ O ₃ catalyst samples for the first reduction cycle.	39
Figure 14: H ₂ -TPR profile of the calcined VO _x /ZrO ₂ -γAl ₂ O ₃ catalyst samples for the first reduction cycle.	40
Figure 15: Consecutive TPR/TPO for the 7.5% V/ZrO ₂ -γAl ₂ O ₃ Catalyst.	42
Figure 16: NH ₃ -Temperature Programmed Desorption profiles for γAl ₂ O ₃ and various VO _x /γAl ₂ O ₃ Catalyst Samples (Heating rate: 15°C/min; NH ₃ adsorbed at 100°C).	43
Figure 17: NH ₃ -Temperature Programmed Desorption profiles for γAl ₂ O ₃ , ZrO ₂ -γAl ₂ O ₃ and various VO _x /ZrO ₂ -γAl ₂ O ₃ Catalyst Samples (Heating rate: 15°C/min; NH ₃ adsorbed at 100°C).	43
Figure 18: Pyridine FTIR Spectra of the 7.5% V/γAl ₂ O ₃ and 7.5% V/ZrO ₂ -γAl ₂ O ₃ Catalysts.	45

Figure 19: Dehydrated Raman Spectra for $\gamma\text{Al}_2\text{O}_3$, 7.5%V/ $\gamma\text{Al}_2\text{O}_3$, $\text{ZrO}_2\text{-}\gamma\text{Al}_2\text{O}_3$ and 7.5%V/ $\text{ZrO}_2\text{-}\gamma\text{Al}_2\text{O}_3$. Note: All reported intensity data are in the same linear scale.....	47
Figure 20: XPS Analysis of the 7.5%V/ $\gamma\text{Al}_2\text{O}_3$ Catalyst (fresh and spent catalysts).	48
Figure 21: XPS Analysis of the 7.5% V/ $\text{ZrO}_2\text{-}\gamma\text{Al}_2\text{O}_3$ Catalyst (fresh and spent catalysts).....	48
Figure 22: Pressure Profile in the CREC Riser Simulator for a Propane ODH Reaction.	53
Figure 23: Propane Conversions during consecutive ODH Cycles over Various $\text{VO}_x/\gamma\text{Al}_2\text{O}_3$ Catalysts.....	55
Figure 24: Propylene and CO_x Selectivities during consecutive ODH injections using various $\text{VO}_x/\gamma\text{Al}_2\text{O}_3$ Catalysts.	55
Figure 25: Propane Conversion during Consecutive ODH Cycles over $\text{VO}_x/\text{ZrO}_2\text{-}\gamma\text{Al}_2\text{O}_3$ Catalysts.....	57
Figure 26: Propylene and CO_x Selectivities during Consecutive ODH Cycles using $\text{VO}_x/\text{ZrO}_2\text{-}\gamma\text{Al}_2\text{O}_3$ Catalysts.....	57
Figure 27: Propane Conversion during 10 Consecutive PODH Cycles using a 7.5V/ $\text{ZrO}_2\text{-}\gamma\text{Al}_2\text{O}_3$ Catalyst at T=500, 525 and 550°C and Reaction Time= 20 sec.	61
Figure 28: Propylene and CO_x Selectivities during 10 Consecutive PODH Cycles using a 7.5V/ $\text{ZrO}_2\text{-}\gamma\text{Al}_2\text{O}_3$ Catalyst at T=500, 525 and 550°C and Reaction Time= 20 sec.....	62
Figure 29: Propane Conversions Obtained with Different Reaction Times and Temperatures. Reported data are the average of 4-10 injections.....	63
Figure 30: Propylene Selectivities Obtained with Different Reaction Times and Temperatures. Reported data are the average of 4-10 injections.....	63
Figure 31: CO_x Selectivities Obtained with Different Reaction Times and Temperatures. Reported data are the average of 4-10 injections.....	64
Figure 32: Proposed Reaction Network for Propane Oxidative Dehydrogenation using a $\text{VO}_x/\text{ZrO}_2\text{-}\gamma\text{Al}_2\text{O}_3$ Catalyst in the CREC Riser Simulator.....	66
Figure 33: Comparison between Experimental Data and Model Predictions over a 7.5V/ $\text{ZrO}_2\text{-}\gamma\text{Al}_2\text{O}_3$ Catalyst at T=500, 525 and 550°C.....	75
Figure 34: Overall Comparison between the Experimental Results and Model Predictions. Data points for three repeats are reported. Standard deviation on repeats is 1.5%.	76
Figure 35: Volume Weighted Particle Size Distribution of PODH Catalyst Particles.	78

Figure 36: Distribution of the Number of Particles in Clusters for $U_g=1.5$ m/s, $G_s=34$ kg/m ² s ¹⁵⁴	79
Figure 37: Schematic Dimensions of the Entry Cyclone (Feeding Cyclone) of the Downer Unit.	82
Figure 38: Schematic Diagram of Downer Unit Showing the Boundary Conditions for CPFDF Calculations and the Propane Injector.	84
Figure 39: Axial Fluid and Particle Cluster Velocities along the Downer Length; (A) Downer unit only and (B) Downer unit Equipped with Feeding and Terminator cyclones.	89
Figure 40: Average Axial Particle Cluster Volume Fraction along the Downer. (A) Downer unit only and (B) Downer equipped with entry and exit cyclones.	89
Figure 41: Simulated Average Pressure Profile along the Downer for a Particle Cluster Flow. (A) Downer unit only and (B) Downer equipped with entry and exit cyclones.	90
Figure 42: Average Pressure Gradient Profile along the Downer with Entry and Exit Cyclones.	90
Figure 43: (a) Radial Velocity Profile for Both Gas and Particle Clusters and (b) Radial Particle Volume Fraction Profile for Particle Clusters.	93
Figure 44: Propane Mass Flowrates through a Downer Bottom at Various Simulation Times.	94
Figure 45: Products Molar Flowrates at the Downer Bottom at Various Simulation Times.	95
Figure 46: Chemical Species Molar Fractions along the Downer unit.	96
Figure 47: Total Fluid Mass Flowrates at the Downer Reactor Top and Bottom at Various Simulation times.	96
Figure 48: Fluid and Particle Temperature Increases along the Downer Length.	98
Figure 49: Radial Temperature Profiles for Fluid and Cluster Particle in the Downer.	99
Figure 50: Axial Velocity Profiles for Fluid and Particles using the “Single Particle” (absent of particle clusters) Flow along the Downer Unit.	100
Figure 51: Particle Volume Fraction for the “Single” Particle Flow Model along the Downer.	100
Figure 52: Chemical Species Molar Fraction along the Downer Using the “Single Particle” (absent of particle cluster) Flow Model.	101
Figure 53: Fluid and Particle Temperature Profile along the Downer using the “Single Particle” (absent of particle cluster) Flow Model.	101

List of Tables

Table 1: Gibbs Free Energy and Enthalpy Changes for propane DH and ODH Reactions.....	7
Table 2: Vanadium-based Propane ODH Catalysts under Oxygen-free Atmosphere.....	14
Table 3: Activation Energies and Activity Decay Parameter Values for the Main Products from PODH Reported in Literature.	15
Table 4: BET Specific surface area, pore volume and average pore diameter for the bare γ -Al ₂ O ₃ and the various prepared catalysts.	35
Table 5: TPR data comparing hydrogen consumption in the first reduction cycle using catalysts with varying amounts of vanadium (wt. %). All TPR analyses were repeated at least 3 times. ..	41
Table 6: Temperature Programmed Desorption of NH ₃ for VO _x / γ -Al ₂ O ₃ and VO _x /ZrO ₂ - γ -Al ₂ O ₃ catalyst samples. The γ -Al ₂ O ₃ and ZrO ₂ - γ -Al ₂ O ₃ Supports are provided as a reference.....	44
Table 7: Acid Properties of 7.5%V/ γ -Al ₂ O ₃ and 7.5%V/ZrO ₂ - γ -Al ₂ O ₃ Catalyst Samples Using Pyridine FTIR.	46
Table 8: XPS Data of the 7.5%V/ γ -Al ₂ O ₃ and 7.5%V/ZrO ₂ - γ -Al ₂ O ₃ Catalysts (fresh and spent)..	49
Table 9: Estimated Desorption Kinetic Parameters for NH ₃ -TPD Kinetics (NH ₃ adsorption at 100°C). Activation energies and k_{des0} are reported with the spans for the 95% confidence intervals.....	52
Table 10: Propane Conversions and Product Selectivities during Thermal Runs.	54
Table 11: Performance of the VO _x / γ -Al ₂ O ₃ catalysts after 10 consecutive cycles.	56
Table 12: Performance of Various VO _x /ZrO ₂ - γ -Al ₂ O ₃ Catalysts after the 10 th Consecutive Cycle.	58
Table 13: Carbon Content Analysis on a per Injection Basis for the 7.5% V/ γ -Al ₂ O ₃ and 7.5% V/ZrO ₂ - γ -Al ₂ O ₃ Catalysts. Reported coke values represent average values.	59
Table 14: Adsorption Parameters for Various Species.	73
Table 15: Intrinsic Kinetic Parameter Summary for the Proposed Kinetic Model with 95% Confidence Intervals (CIs).....	74
Table 16: Governing Equations for an Adapted CPFD Model Including the PODH Reaction. ..	80
Table 17: Input Parameters in the CPFD Simulation.....	85
Table 18: Drag Models Used in the CPFD Simulation.....	86
Table 19: Reactions, Kinetic Parameters and Thermodynamics Properties for the PODH Considered in the Present Calculations.....	87

Nomenclatures

A_p	Particle acceleration
C_d	Drag coefficient
C_i	Concentration (mol/cm ³) of species “i”
CO_x	Carbon Oxides
$C_{C_3H_8b}$	Propane concentration in the bulk fluid (mol/m ³)
$C_{C_3H_8s}$	Propane concentration at the catalyst outer surface (mol/m ³)
C_{WP}	Weisz-Prater criterion (dimensionless)
D_{AB}	Diffusivity of propane in argon (m ² /s)
D	Turbulent mass diffusion rate which is related to viscosity
D'	Diameter of the oxygen carrier particle (μm)
D_{eff}	Effective diffusivity (m ² /s)
D_p	Drag function
E_{des}	Activation Energy of Desorption (KJ/mol)
E_i	Activation energy (kJ/mol)
f_p	Function of the particle spatial location
F	Rate of momentum exchange per unit volume between the gas and solid phase
g	Acceleration due to gravity
h_g	Gas enthalpy
k_d	Desorption Constant, $(\frac{cm^3}{g_{cat} \times min})$
k_{des0}	Pre-Exponential Factor, $(\frac{cm^3}{g_{cat} \times min})$
k_i	Reaction rate constant (mol/g _{cat} .sec)
k_i^0	Intrinsic kinetics constant pre-exponential factor (mol/g _{cat} .sec)
K_i	Adsorption constant for component ‘i’ (atm ⁻¹)
K_i^0	Adsorption constant pre-exponential factor (atm ⁻¹)
m-ZrO ₂	Monoclinic Zirconia

m_p	Mass of the particle
n_i	Moles of gaseous carbon containing product 'i';
n_{propane}	Moles of unconverted propane in the product stream;
$N_{\text{C}_3\text{H}_8}$	Number of moles of propane injected (mole)
p_g	Gas pressure (Pa)
P_i	Partial pressure of species "i" (atm)
$-r_{\text{C}_3\text{H}_8\text{obs}}$	Observed rate of the reduction reaction ($\text{mol}/\text{m}^2 \text{ s}$)
\mathbf{q}	Gas heat flux
q_D	Enthalpy diffusion term
\dot{Q}	Energy source per unit volume
r_{des}	Rate of Desorption, ($\frac{\text{cm}^3}{\text{g}_{\text{cat}} \times \text{min}}$)
r_i	Reaction rate ($\text{mol}/\text{g}_{\text{cat}} \cdot \text{sec}$)
r_p	Particle radius
R	Universal gas constant
Re	Reynolds number (dimensionless)
ρ_{OC}	Oxygen carrier particle density (kg/m^3)
S_{BET}	Brunauer–Emmet–Teller Specific Surface area (m^2/g)
Sc	Schmidt number (dimensionless)
Sh	Sherwood number (dimensionless)
S_i	Selectivity of Component i (%) based on propane conversion into gas phase carbon containing products
T_m	Centering Temperature which Minimizes the Cross-Correlation between Parameters (k)
$t\text{-ZrO}_2$	Tetragonal Zirconia
u_g	Fluid velocity (m/s)
u_p	Particle velocity (m/s)
$\overline{\mathbf{u}}_p$	Local mass averaged particle velocity (m/s)
V_{des}	Volume of ammonia desorbed ($\text{cm}^3/\text{g}_{\text{cat}}$)
V_m	Volume of monolayer coverage ($\text{cm}^3/\text{g}_{\text{cat}}$)
V_i^A	Species volume adsorbed on the catalyst ($\text{cm}^3/\text{g}_{\text{cat}}$)

V_{pore}	Pore Volume (cm^3/g)
VO_x	Vanadium Oxide Surface Species
V 2p _{3/2}	XPS spectra for vanadium 2p _{3/2}
w	Weight of the oxygen carrier sample tested (g)
$W_{\text{C}_3\text{H}_8\text{r}}$	Radial flux of propane ($\text{mol}/\text{m}^2 \text{ s}$)
$X_{\text{C}_3\text{H}_8}$	Propane Conversion (%) based on gas phase carbon containing products
$Y_{\text{C}_3\text{H}_6}$	Propylene Yield (%) based on propane conversion into gas phase carbon containing products

Greek Symbols

β	Degree of Reduction of Catalyst
β'	Rate of temperature increase, $^{\circ}\text{C}/\text{min}$
$\delta\dot{m}_p$	Gas mass production rate per volume
$\delta\dot{m}_{i,\text{chem}}$	Net production rate of species due to gas phase chemical reactions
ε_g	Gas volume fraction
ε_p	Particle volume fraction
γ	Cross-Correlation Coefficient in Cross-Correlation Matrix
λ	Decay Constant (-)
μ_g	Fluid viscosity (Pa.s)
ν_i	Number of carbon atoms in gaseous carbon containing product 'i';
φ	Degree of Oxidation of the Catalyst
ρ_g	Fluid density (kg/m^3)
ρ_p	Particle density (kg/m^3)
θ_{ads}	Fraction of surface covered by adsorbed species
τ_g	Stress tensor
τ_p	Contact normal stress
$-\Delta H_i$	Heat of Adsorption (kJ/mol)

Abbreviations

CFB	Circulating Fluidized Bed
-----	---------------------------

CPFD	Computational Particle Fluid Dynamics
CREC	Chemical Reactor Engineering Center
DH	Dehydrogenation
FCC	Fluid Catalytic Cracking
FID	Flame Ionization Detector
FTIR	Fourier Transform Infrared Spectroscopy
MP-PIC	Multi-Phase Particle-in-Cell
LRS	Laser Raman Spectroscopy
PODH	Propane Oxidative Dehydrogenation
PSD	Particle Size Distribution
TCD	Thermal Conductivity Detector
TPD	Temperature Programmed Desorption
TPO	Temperature Programmed Oxidation
TPR	Temperature Programmed Reduction
XPS	X-ray Photoelectron Spectroscopy
XRD	X-ray Diffraction

Chapter 1: Introduction

1.1 Propylene Demand

Propylene is one of the most important building blocks in the petrochemical industry ¹⁻³. It is employed industrially to produce polypropylene, which is used extensively for packaging and labeling, textile products, laboratory equipment, loudspeakers and automotive components. Propylene is also used for the manufacturing of acrylonitrile, propylene oxide derivatives and other substances ^{4,5}. According to the IHS Chemical World Analysis, the current global propylene demand is the range of 90 million metric tons (MMT) per year. It is estimated this demand will rise up to 130 MMT per year by 2023. ^{6,7}

1.2 Traditional Processes for Propylene Productions

The traditional olefin processes involve steam cracking, fluid catalytic cracking (FCC) and catalytic dehydrogenation (CDH) ^{1,3,8-10}. Typical feedstocks for the steam cracking are ethane, LPG (light petroleum gas) and naphtha. These olefin production processes include homogeneous reactions where the hydrocarbon species are steam cracked into smaller olefins³. For FCC, commonly used feedstocks are vacuum gas oil, residues and de-asphalted oil, which are converted into light and higher value products such as gasoline. Cracking processes are endothermic, consume large amounts of heat and require adequate designs to be operated at high temperatures.⁹ As well, significant undesirable amounts of coke are formed, imposing severe operating constraints with frequent plant shutdown ^{1,10,11}.

Catalytic dehydrogenation (CDH) is an economical route to upgrade low-cost saturated alkanes, such as ethane and propane, into the more valuable olefin feedstocks (e.g. ethylene, propylene) ¹². Furthermore, and given the recent increase of shale gas availability ¹³⁻¹⁵, there is a renewed interest in efficient and economical routes to convert alkanes into olefins. One should note that, CDH is thermodynamically limited ^{3,8,16}. At the present time, CDH is mainly considered for propane and butane dehydrogenation. In this respect, one can list the several industrial scale processes ^{8,17} for propane dehydrogenation. These include CATOFIN from ABB Lummus, OLEFLEX from UOP, Fluidized Bed Dehydrogenation (FBD) from Snamprogetti, and Steam Active Reforming (STAR) from Phillips Petroleum. These technologies differ with respect to the catalyst type used, the

reactor design employed, and the selected operating conditions. These processes include a dehydrogenation section and a catalyst regeneration section^{18,19}. CDH display however, similar constraints such as steam cracking and FCC do, with these being: a) involve endothermic reactions and b) require operating temperatures in the 450-700°C range. At these high temperatures, cracking and coking can occur, limiting the use of potentially valuable catalysts such as Cr₂O₃/Al₂O₃ and Pt/Sn/Al₂O₃. Due to these issues, and given that in catalytic cracking (FCC), olefins are by-products only, existing processes are insufficient to satisfy increasing olefin market demands.^{8,14}

1.3 Oxidative Dehydrogenation (ODH) Process

1.3.1 ODH with Molecular Oxygen

Thus and to alleviate the issues associated with the dehydrogenation process, oxygen can be added to the reaction medium, promoting ODH (oxidative dehydrogenation)². As a result the reaction becomes exothermic and irreversible reaction overcoming the thermodynamic limitations of dehydrogenation (DH)^{5,8,20,21}. Here, water is formed as a stable product. ODH displays large and positive equilibrium constants, with these equilibrium constants decreasing at higher temperatures. Furthermore, the presence of oxygen limits coking and therefore extends catalyst usage. It is in fact at the 650°C thermal level where ODH provides an opportunity versus thermal or the non-oxidative catalytic dehydrogenation (CDH)⁹.

Most ODH reactions are carried out in the presence of gaseous oxygen between 400 and 700°C²²⁻²⁵. Catalytic ODH with gas phase oxygen faces several challenges: (i) co-feeding gaseous oxygen with alkanes leads to potential safety hazards; (ii) oxygen produced from cryogenic air separation is costly and energy-intensive; (iii) electrophilic surface oxygen species such as O⁻ and O²⁻, formed from surface adsorbed gaseous oxygen can limit the selectivity of the ODH reaction²⁶⁻²⁹, iv) Undesired CO_x may also be formed either by direct alkane combustion or by deep oxidation of the product olefins, limiting olefin selectivity^{29,30}. Major issues as well, in alkanes, there are only sigma bonds like C-C single bonds (bond energy is around 347 kJ/mol) and C-H bonds (308-435 kJ/mol). But in alkenes, C-C double bond contains both a sigma bond plus a pi-bond. The bond energy of an average C-C pi bond is 264 kJ/mol which is remarkably lower than that of a C-C sigma bond. This helps alkene for rapid combustion^{8,31-33}.

Other than CO_x formation, a comparatively important product in ODH is H_2 ^{20,34}. Non-oxidative dehydrogenation becomes thermodynamically favored at 650°C and above, with hydrogen formation yielding coke and free radicals ^{34,35}. In this respect, when O_2 is near depletion, non-oxidative processes dominate ODH, with the CO_2 and H_2O formed also being consumed. These conditions enhance the overall H_2 yields observed ³⁶.

Regarding the contribution of homogeneous gas phase reactions to the ODH of light alkanes, it has been shown that they can play a significant role above 600°C ^{15,20,36–38}. Thus, the heterogeneous and homogeneous ODH reactions may be highly coupled at such conditions. Furthermore, it has also been suggested that, catalytic surface reactions may also contribute to accelerating ignition, supplying heat to the gas phase propylene formation. Reactions are initiated at the catalyst surface via C–H bond splitting with the formation of radicals. These radicals may subsequently undergo homogeneous gas phase reactions³⁹.

The oxidative dehydrogenation of light alkanes does not have many of the disadvantages of the endothermic pyrolytic processing of hydrocarbons with high energy consumption, coking and the formation of a considerable amount of by-products ². Major challenges in its implementation at the pilot and demonstration scale remain however, the following: i) removal of the heat of reaction, ii) control of consecutive oxidation reactions leading to the formation of undesired by-products ^{29,40,41}, iii) keeping paraffins and oxygen mixtures under explosive limits, preventing reaction run-aways ^{2,42}.

1.3.2 ODH with Mild Oxidants

While gas phase molecular oxygen may oxidize the deposited carbon on the catalyst surface, it also decreases olefin selectivity via deep oxidation to CO_x . As a result, and due to these various issues, alternative processes converting paraffins more efficiently in the absence of gaseous oxygen are highly desirable ¹³. To avoid total oxidation of alkanes, the use of mild oxidants have also been proposed ^{43–48}.

Among all the mild oxidants recently studied, carbon dioxide (CO_2) has been used as a soft oxidant for the ODH of various alkanes (ethane, propane) ^{15,30,44,49,50}, ethylbenzene⁵¹ and methane coupling for ethene production ⁴⁴. CO_2 is used due to its advantages in controlling the exothermicity of the

reaction⁵² and due to its role as a chemical species diluent. Furthermore, it offers high equilibrium conversion conditions, improving olefin selectivity, reducing coke formation and maintaining longer catalyst life. Such a strategy for the utilization of CO₂ for commercial purposes is attractive and promising, as CO₂ can be used for the synthesis of valuable products rather than releasing it into the atmosphere^{44,53}.

However, the use of CO₂ suffers from its inherent inertness³⁰. It is anticipated that the application of a suitable catalyst instead could help to overcome the unfavorable thermodynamics and kinetic barrier of CO₂ activation. In this respect, the foremost challenging aspect of CO₂ utilization is the activation of a CO₂ molecule with a Gibbs Energy of Formation of -394.4 kJ/mole³⁰. Furthermore, a kinetic barrier also plays a key role due to its inertness. Therefore, it is anticipated that the interaction of the CO₂ with a metal complex in a homogeneous reactor or with a solid surface in a heterogeneous reaction may help to overcome the kinetic barrier. In spite of these findings, even mild oxidants are proposed to replace gaseous oxygen, as they still lead to a significant deep oxidation of alkanes.

1.3.3 ODH with Catalyst's Lattice Oxygen

Several researchers^{3,9,10,12,54-59} have studied ethane and propane ODH. These researchers^{12,59-63} have investigated light alkane ODH under an oxygen-free atmosphere with the source of oxygen being the catalyst lattice oxygen only. Catalyst lattice oxygen instead of gas phase molecular oxygen or other mild oxidants prevents deep oxidation, limiting CO_x. This process can lead in principle to higher olefin selectivity.

Given these interesting prospects, ODH under an oxygen-free atmosphere is nowadays focused on: a) The development of new and stable ODH catalysts providing lattice oxygen at low temperatures (e.g. 400-550° C) and very limited carbon oxides, b) Taking full advantage of the favorable thermodynamics facilitating temperature reactor control^{2,8,64-68}. In considering these interesting scenarios that the present PhD research was initiated.

Chapter 2: Literature Review on Propane Oxidative Dehydrogenation under Gas Phase Oxygen-free Conditions

2.1 Thermodynamics Study

At chemical equilibrium, a reacting system achieves a condition where the total Gibbs Free Energy is minimized⁶⁹. To assess chemical equilibrium, stoichiometric approach is the one considered for PODH. The “stoichiometric” approach requires a defined stoichiometry involving all reactants and products with their molecular formulae^{70,71}.

One can notice in this respect that, if the PODH with gaseous oxygen, Equation (11) of Table 1 is the reaction driving the ODH, the equilibrium constant can be calculated as:

$$K_r = \frac{[C_3H_6][H_2O]}{[C_3H_8][O_2]^{\frac{1}{2}}} \quad (1)$$

where, $[C_3H_6]$, $[H_2O]$, $[C_3H_8]$ and $[O_2]$ represent thermodynamic activities of the gaseous products and reactants. At high temperatures and low pressure conditions however, the activities of gaseous reactants/products can be considered as equivalent to their partial pressures. Therefore, the equilibrium constant K_r can be expressed as:

$$K_r = \frac{[P_{C_3H_6}][P_{H_2O}]}{[P_{C_3H_8}][P_{O_2}]^{\frac{1}{2}}} \quad (2)$$

The partial pressures can further be expressed in terms of total pressure P and the gases mole fractions as:

$$K_r = \frac{[y_{C_3H_6}][y_{H_2O}]}{[y_{C_3H_8}][y_{O_2}]^{\frac{1}{2}}} P^{(1+1-1-0.5)} \quad (3)$$

$$K_r = \frac{[y_{C_3H_6}][y_{H_2O}]}{[y_{C_3H_8}][y_{O_2}]^{\frac{1}{2}}} P^{0.5} \quad (4)$$

Therefore, for each independent reaction, one equilibrium expression can be formulated. Following the above sequence, the equilibrium constant for the PODH reaction, involving a lattice oxygen is mentioned below where the dominant equation is Equation (21) in Table 1:

:

$$K_r = \frac{[y_{C_3H_6}][y_{H_2O}]}{[y_{C_3H_8}]} P \quad (5)$$

As the activities of the solid reactants and products under standard conditions considered one, we can therefore ignore the solids in Equation (5).

Thus, one can notice as well that these differences in equilibrium constants not only influence the main PODH reaction, yielding propylene, but also affect all the other secondary reactions.

Table 1 reports ΔG_R and ΔH_R at the reference condition of 298K, for the various reactions involved in the propane ODH, under both O_2 rich and O_2 -free atmospheres. One can thus observe, that the PODH reactions with gaseous oxygen are more exothermic than the PODH reactions using the lattice oxygen. Data of Table 1 can be considered to establish the intrinsic advantage from thermodynamics for PODH reactors with the PODH reaction being driven by the lattice oxygen. These PODH reactors will likely provide conditions for the better controllability of undesired reactions, as a result of the better management of temperature runaways.

Table 1: Gibbs Free Energy and Enthalpy Changes for propane DH and ODH Reactions.

Possible Reactions	Chemical Reactions	$\Delta G_{f(298)}^0 \left[\frac{\text{kJ}}{\text{mol}} \right]$	$\Delta H_{f(298)}^0 \left[\frac{\text{kJ}}{\text{mol}} \right]$
Dehydrogenation (DH) ⁷²	$\text{C}_3\text{H}_8(\text{g}) \leftrightarrow \text{C}_3\text{H}_6(\text{g}) + \text{H}_2(\text{g})$ (6)	86.2	124.3
	$\text{C}_3\text{H}_8(\text{g}) \rightarrow \text{CH}_4(\text{g}) + \text{C}_2\text{H}_4(\text{g})$ (7)	41.0	81.4
	$\text{C}_2\text{H}_4(\text{g}) + \text{H}_2(\text{g}) \rightarrow \text{C}_2\text{H}_6(\text{g})$ (8)	-101.3	-137.2
	$\text{C}_3\text{H}_8(\text{g}) + \text{H}_2(\text{g}) \rightarrow \text{CH}_4(\text{g}) + \text{C}_2\text{H}_6(\text{g})$ (9)	-60.2	-55.7
	$\text{C}_3\text{H}_8(\text{g}) = 3\text{C}(\text{s}) + 4\text{H}_2(\text{g})$ (10)	23.4	103.9
O ₂ -Rich Atmosphere ^{5,8,68,72,73}	$\text{C}_3\text{H}_8(\text{g}) + 0.5\text{O}_2(\text{g}) \rightarrow \text{C}_3\text{H}_6(\text{g}) + \text{H}_2\text{O}(\text{g})$ (11)	-142.4	-117.6
	$\text{C}_3\text{H}_8(\text{g}) + 5\text{O}_2(\text{g}) \rightarrow 3\text{CO}_2(\text{g}) + 4\text{H}_2\text{O}(\text{g})$ (12)	-2074.2	-2044.0
	$\text{C}_3\text{H}_8(\text{g}) + 3.5\text{O}_2(\text{g}) \rightarrow 3\text{CO}(\text{g}) + 4\text{H}_2\text{O}(\text{g})$ (13)	-1302.7	-1195.1
	$\text{C}_3\text{H}_6(\text{g}) + 4.5\text{O}_2(\text{g}) \rightarrow 3\text{CO}_2(\text{g}) + 3\text{H}_2\text{O}(\text{g})$ (14)	-1931.8	-1926.4
	$\text{C}_3\text{H}_6(\text{g}) + 3\text{O}_2(\text{g}) \rightarrow 3\text{CO}(\text{g}) + 3\text{H}_2\text{O}(\text{g})$ (15)	-1160.2	-1077.5
	$\text{CO}(\text{g}) + 0.5\text{O}_2(\text{g}) \rightarrow \text{CO}_2(\text{g})$ (16)	-257.2	-283.0
	$\text{C}_3\text{H}_8(\text{g}) + 1.5\text{O}_2(\text{g}) \rightarrow \text{C}_2\text{H}_4(\text{g}) + \text{CO}(\text{g}) + 2\text{H}_2\text{O}(\text{g})$ (17)	-502.6	-437.9
	$\text{C}_3\text{H}_8(\text{g}) + 2\text{O}_2(\text{g}) \rightarrow \text{C}_2\text{H}_4(\text{g}) + \text{CO}_2(\text{g}) + 2\text{H}_2\text{O}(\text{g})$ (18)	-759.8	-720.8
	$\text{C}_3\text{H}_6(\text{g}) + \text{O}_2(\text{g}) \rightarrow \text{C}_2\text{H}_4(\text{g}) + \text{CO}(\text{g}) + \text{H}_2\text{O}(\text{g})$ (19)	-360.2	-320.3
	$\text{C}_3\text{H}_6(\text{g}) + 1.5\text{O}_2(\text{g}) \rightarrow \text{C}_2\text{H}_4(\text{g}) + \text{CO}_2(\text{g}) + \text{H}_2\text{O}(\text{g})$ (20)	-617.4	-603.3
O ₂ -Free Atmosphere ^{10,12}	$\text{C}_3\text{H}_8(\text{g}) + \text{V}_2\text{O}_5(\text{s}) = \text{V}_2\text{O}_4(\text{s}) + \text{C}_3\text{H}_6(\text{g}) + \text{H}_2\text{O}(\text{g})$ (21)	-41.5	5.9
	$\text{C}_3\text{H}_8(\text{g}) + 10\text{V}_2\text{O}_5(\text{s}) = 10\text{V}_2\text{O}_4(\text{s}) + 3\text{CO}_2(\text{g}) + 4\text{H}_2\text{O}$ (22)	-1065.2	-809.7
	$\text{C}_3\text{H}_8(\text{g}) + 7\text{V}_2\text{O}_5(\text{s}) = 7\text{V}_2\text{O}_4(\text{s}) + 3\text{CO}(\text{g}) + 4\text{H}_2\text{O}(\text{g})$ (23)	-596.3	-331.1
	$\text{C}_3\text{H}_6(\text{g}) + 9\text{V}_2\text{O}_5(\text{s}) = 9\text{V}_2\text{O}_4(\text{s}) + 3\text{CO}_2(\text{g}) + 3\text{H}_2\text{O}(\text{g})$ (24)	-1023.6	-815.6
	$\text{C}_3\text{H}_6(\text{g}) + 6\text{V}_2\text{O}_5(\text{s}) = 6\text{V}_2\text{O}_4(\text{s}) + 3\text{CO}(\text{g}) + 3\text{H}_2\text{O}(\text{g})$ (25)	-554.8	-337.0
Catalyst Regeneration ¹⁰	$2\text{V}_2\text{O}_4(\text{s}) + \text{O}_2(\text{g}) \rightarrow 2\text{V}_2\text{O}_5(\text{s})$ (26)	-201.8	-246.9

The equilibrium constant K_r for each of these reactions can be related to the ΔG_r , according to the following equation:

$$K_r = \exp \left[-\frac{\Delta G_r}{RT} \right] \quad (27)$$

where, R is the universal gas constant $8.314 \text{ J}/(\text{mol K})$.

Figure 1 reports the changes of the equilibrium constants for PODH (propane ODH) under an oxygen-free atmosphere.

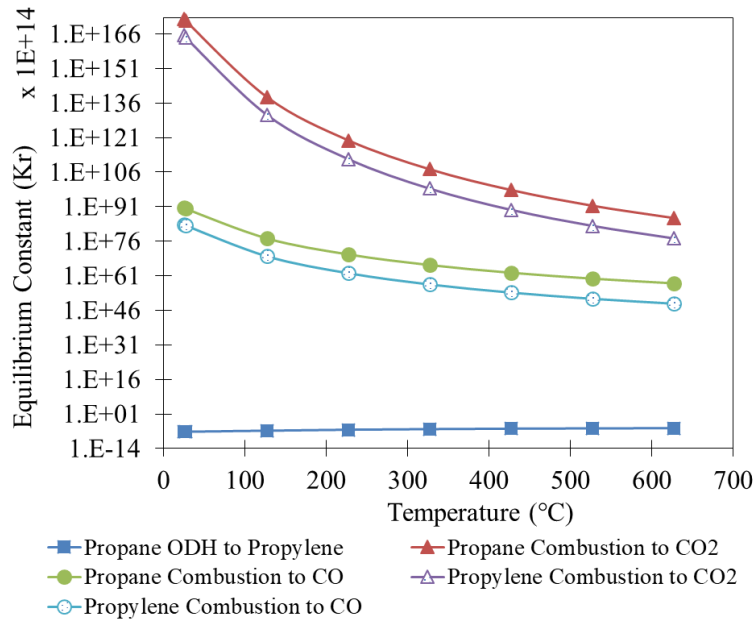


Figure 1: Chemical Equilibrium Constant as a Function of Temperature for Propane ODH under an O_2 -Free Atmosphere. Total pressure: 1 atmosphere.

One can observe from Figure 1 that, the reactions involved in the PODH under oxygen-free atmospheres are all thermodynamically favored, with equilibrium constants not being hindered by thermodynamics.

Regarding the ODH process under an O_2 -free atmosphere, the catalyst regeneration reaction ($2\text{V}_2\text{O}_4 + \text{O}_2 = 2\text{V}_2\text{O}_5$) is both spontaneous and exothermic. Therefore, the energy for the ODH reaction under an O_2 -free atmosphere (propane ODH to propylene) is recovered from the regeneration reaction.

2.2 Vanadium-Based Catalyst Development for Propane ODH

Catalyst development for ODH reactions has focused on variety of metal oxides alone or metal oxides combined with additives (alkali metals and halides), supported on a variety of metal oxide supports. First, research studies used metal oxides as catalysts. However, supported catalysts show several advantages over the unsupported catalysts⁷⁴ given that they provide : a) better control of metal loading and metal dispersion, and b) added flexibility to adjust physicochemical properties. For example, TiO₂ supported VOPO₄ catalysts give higher ethylene selectivity than the unsupported VO_x and (VO)₂P₂O₇ catalysts⁷⁵. Authors^{28,50} focused on the addition of promoters, that can also improve the catalyst performance. The promoters isolate the active species and form secondary metal oxides on the support surface.

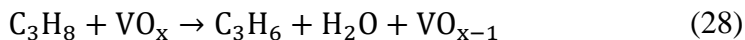
Research on the catalysts of the ODH process usually fall into two operating thermal levels: above or below the temperatures at which significant gas phase reactions take place. High temperature catalysts mainly contain alkali-metal and/or alkaline-earth-metal oxides supported on transition-metal oxides, rare-earth-metal oxides and other catalytic materials. Low temperature catalysts on the other hand, usually consist of reducible transition metal oxides.^{12,59}

As alkali and alkaline earth-based catalysts contain non-reducible ions and oxides, temperatures in excess of 600°C are needed. However, higher reaction temperatures are less favorable for high olefin selectivity. Therefore, reducible transitional metal oxide catalysts are considered. This catalyst group can activate the paraffins at low temperatures. However, while catalytic activity is usually higher with this class of catalysts, lower alkene selectivities are frequently found. The oxides of these metals contain removable oxygen (lattice oxygen) which participates in the ODH reactions under oxygen-free atmosphere conditions. However, lattice oxygen is also involved in the unselective pathways of ODH, forming carbon oxides. Therefore, different catalyst groups are analyzed to find the optimum catalyst that will give high selectivity of olefins.^{10,12,27,54,59,76-78}

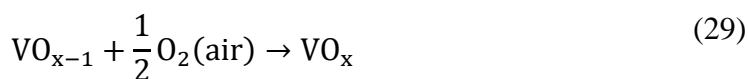
Vanadium is the most frequently considered element for ethane and propane ODH. In particular, the VO_x shows promising results for olefin production under an oxygen-free environment^{12,54,59,61}. VO_x has a suitable geometric and electron structure. Furthermore, the V⁴⁺ and V⁵⁺ valence states make Vanadium valuable for many catalytic reactions⁷⁹. Moreover, supported vanadium oxides

have attracted much attention due to their higher performance, better thermal stability, and large specific surface areas.

In this respect, the stoichiometric equation for the conversion of propane ODH to propylene over vanadium-based catalysts (this reaction occurs in the downer reactor which is described later) can be represented as:



This reduced vanadium species is regenerated via molecular oxygen (this reaction occurs in the regenerator) following the stoichiometry described below:



So, by adding (28) and (29) equations, for the complete downer and regenerator PODH process, overall reaction will be: $\text{C}_3\text{H}_8 + \frac{1}{2}\text{O}_2(\text{air}) \rightarrow \text{C}_3\text{H}_6 + \text{H}_2\text{O}$

The redox behavior of supported vanadia catalysts in ODH is generally controlled by three main factors: (i) the VO_x surface structure (ii) the acid-base character of the metal and support and (iii) the redox properties of the VO_x species. These three properties are influenced by the support type and vanadium loading^{80,81}.

2.2.1 VO_x Surface Coverage

The molecular structures of surface vanadia species on metal oxide supports have been reported in the technical literature^{82–85}. These studies suggest that depending on the vanadium loading on the support, four kinds of VO_x surface species are present on the catalyst surface: (a) isolated VO_4 species (monovanadate); (b) polymeric VO_4 species (polyvanadates); (c) a mix of both isolated and polymeric VO_4 surface species, and (d) V_2O_5 crystals. Some studies^{80,85–88} showed that, at low vanadium loading, a highly dispersed isolated VO_4 surface species (monovanadates) is formed. As the VO_x surface density increases with vanadium loading, surface structures evolve from isolated monovanadates to polymeric polyvanadate. In this respect, it appears polymeric polyvanadate dominates until a monolayer surface coverage is reached. At high vanadium loadings, crystalline V_2O_5 nanoparticles form on top of the vanadia monolayer. It is generally

accepted in alkane ODH, that isolated tetrahedral VO_x species (which are obtained at low vanadium loading) are more selective but less active than polymeric VO_x species.

2.2.2 Active Lattice Oxygen Species

Other than the ODH catalyst structure, the variation of the binding strength of the surface lattice oxygen in the VO_x surface species is a main parameter that governs activities and selectivities of alumina-supported vanadia catalysts. In extensive structural studies of supported vanadium oxide catalysts^{84,89,90}, three types of lattice oxygen bonds were identified (Figure 2): a) terminal $\text{V}=\text{O}$ bonds, b) bridging $\text{V}-\text{O}-\text{V}$ bonds, and c) $\text{V}-\text{O}-$ support bonds. Each type of lattice oxygen has a different binding strength. The studies were aimed at determining which type is responsible for the oxidation activity which occurs in various catalytic oxidation reactions^{89,91}. It was determined that, the oxygen in the $\text{V}-\text{O}-$ Support bond rather than the terminal $\text{V}=\text{O}$ or $\text{V}-\text{O}-\text{V}$ bonds is the one involved in this catalytic oxidation reaction.

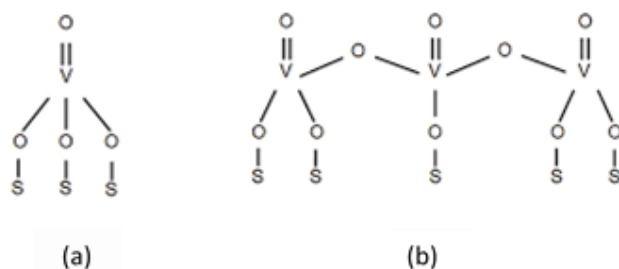


Figure 2: (a) Isolated VO_4 species on support (s); (b) Polymeric VO_4 species on support (s).

2.2.3 Effect of Support (Acid/Base Properties)

Metal oxides are composed of redox metal cations and lattice oxygen anions which are Lewis acid and basic sites, respectively. The acid-base support characteristics contribute with several effects, namely on:

- (a) The dispersion of the active species;
- (b) The specific structure of the active species;
- (c) The reactant molecule activation;
- (d) The rates of competitive pathways of transformation;
- (e) The rate of adsorption and desorption of reactants and products.

Furthermore, the support acid-base can influence the vanadium-based catalyst reactivity or selectivity^{80,90–93}. For instance, the interaction between the acidic V_2O_5 species and a basic support may be strong (e.g., MgO , La_2O_3 , Sm_2O_3). This may lead to the formation of highly dispersed VO_x species, which are responsible for the high selectivities to alkenes. In contrast, the interaction between the acidic V_2O_5 and an acidic support (e.g., SiO_2 , Al_2O_3) may be weak. This may lead to a less dispersed vanadium species, which favors formation of a less active V_2O_5 crystalline phase^{92,94,95}.

Moreover, on acidic catalysts, basic reactant adsorption and acidic product desorption are favored. This thereby protects chemical species from further oxidation to carbon oxides. For instance, higher selectivities to ethylene have been obtained using acidic based catalysts like the $VO_x/\gamma-Al_2O_3$ catalysts. These findings were justified given that higher support acidity decreases the interaction between the ethylene product and the catalyst^{55,94}. In addition, dominant Brønsted acid sites was considered desirable and this to facilitate rapid olefin desorption, limiting the complete alkane oxidation to CO_x . Thus, catalyst acidity and acid site type have to be kept at acceptable levels and this not to interfere with overall catalytic activity and selectivity⁹³.

2.2.4 Red-Ox Properties of Supported VO_x Catalysts

The reducibility of vanadium oxide is considered as one of the main factors influencing its activity in partial oxidation and in the ODH reactions of alkanes. There is a parallel relationship between catalyst reducibility and VO_x surface structure on a given metal oxide support. In this respect, the reducibility of the surface VO_x species increases with surface VO_x coverage. Thus, the following trend for the reducibility of the different supported vanadia species can be considered: polymeric surface $VO_x >$ isolated surface $VO_x >$ crystalline V_2O_5 nanoparticles^{80,93,96}. Moreover, the extent of the reducibility of supported vanadium oxide catalysts is affected by the type of support used.

Redox properties are also affected by the support acid-base character with decreasing reducibility of V species for more basic support oxides⁹⁷. Moreover, propane ODH reaction runs conducted at 450–550°C, showing that, the V_2O_5/TiO_2 catalyst which is less basic and easier to reduce is the most active catalyst, while V_2O_5/Al_2O_3 which is more acidic and difficult to reduce is the most selective in propylene production. This variation of vanadium oxide reducibility on different metal

oxide supports could be related to the reducibility of the different V-O-Support bonds existing on different support types^{80,94,97}.

Thus, one can conclude that the catalytic activity and selectivity of the supported vanadium oxide catalysts are significantly affected by the properties of the support oxide material, the interaction of the surface VO_x species with the oxide support and the vanadium loading. The redox sites are in charge of transferring the lattice oxygen to the adsorbed propane to form propylene. The acid sites catalyze the condensation of the intermediates. Therefore, to enhance the efficiency of such a process, it is necessary to investigate the synergistic effect of the redox and acidic properties of a catalyst as well as their dependence on the catalyst composition and reaction conditions.

2.2.5 Vanadium-based Propane ODH Catalysts under Oxygen-free Atmosphere

Several vanadium-based catalysts have been studied so far for PODH where the only oxygen source is the catalyst lattice oxygen. Table 2 shows literature reported reaction conditions and conversion, selectivities value from propane ODH under oxygen-free atmosphere.

Hossain et al.^{61,98} developed a vanadium-based CaO- γ -Al₂O₃ support for propane ODH. They prepared CaO to γ -Al₂O₃ weight ratios of 1:4 and 1:1 and achieved best results with the 1:1 weight ratio. They performed ODH at a 550-640°C temperature range and achieved 25.5% propane conversion, 94.2% propylene selectivity and 5.8% CO_x selectivity at 640°C. At this high temperature, the thermal reaction has a negative impact on the ODH reaction.

Ghamdi et al.¹² reported different PODH catalysts prepared with different vanadium loadings on γ -Al₂O₃ (5, 7 and 10 wt. % V) of catalysts for propane ODH at a reaction temperature range of 475-550°C and reaction times of 5-20 sec. As γ -Al₂O₃ is acidic in character, re-adsorption of propylene product was assigned to methane, ethane and ethylene cracking. Therefore, the maximum selectivity of propylene that these authors achieved was 85.94% at 11.73% propane conversion. The rest of the products were CO_x, CH₄, C₂H₄ and C₂H₆.

Fukudome et al.^{62,63} incorporated VO_x species into an SiO₂-frame to obtain a higher concentration of isolated VO_x species. This catalyst was synthesized by an alkoxy exchange between a metal alkoxides and polyethylene glycol. Following this, PODH using VO_x lattice oxygen was performed in a fixed-bed reactor at a 450°C temperature under atmospheric pressure. These

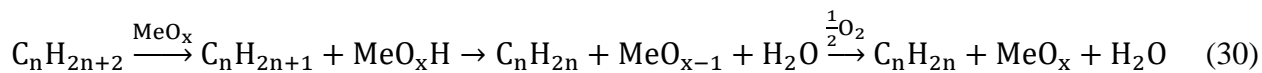
researchers found that VO_x incorporated into SiO₂ showed higher propylene selectivity than VO_x loaded onto SiO₂. This could be ascribed to the isolated VO₄³⁻ species in the silica framework.

Table 2: Vanadium-based Propane ODH Catalysts under Oxygen-free Atmosphere.

ODHP Catalyst	Feed	Reactor	Method	T (°C)	Time	X _{C₃H₈}	Selectivity (%)		Y _{C₃H₆}	Year
							S _{C₃H₆}	S _{CO_x}		
VO _x /CaO- γAl ₂ O ₃	C ₃ H ₈	Fluidized-bed	Successive	550- 640	10-31 s	10.30- 25.50	78.30- 94.20	5.80- 21.70	8.10- 24.00	2017 ⁶¹
5% VO _x /γAl ₂ O ₃	C ₃ H ₈	Fluidized-bed	Successive	475- 550	5-20 s	2.35-11.73	70.89- 85.94	86.49- 96.90	2.76-5.41	2014 ¹²
7% VO _x /γAl ₂ O ₃	C ₃ H ₈	Fluidized-bed	Successive	475- 550	5-20 s	3.24-13.36	60.73- 75.34	10.43- 35.81	2.57-7.21	2014 ¹²
10% VO _x /γAl ₂ O ₃	C ₃ H ₈	Fluidized-bed	Successive	475- 550	5-20 s	3.73-15.05	55.12- 67.77	15.01- 41.52	2.48-8.72	2014 ¹²
V(1.0)- PEG25	C ₃ H ₈	Fixed-bed	Single	450	8 min	2.00	94.80	1.90	1.90	2013 ⁶²
VO _x /SiO ₂	C ₃ H ₈	Fixed-bed	Single	450	8 min	3.00	88.30	7.00	23.90	2011 ⁶³

2.3 Kinetics and Reaction Mechanisms of Propane ODH over Vanadium-based Catalysts

Baerns et al. reported⁹⁹ the mechanism for the initial activation of the free radicals in the alkane ODH reaction over transitional metal oxides catalysts (i.e. VO_x, MoO_x etc.). According to this, oxygen of the metal oxide abstracts hydrogen from the alkane. The OH groups formed are then removed from the surface by dehydration. Thus, in the formation of propylene and total oxidation products, the catalyst surface is reduced. Thus, and as a result the catalyst has to be subsequently re-oxidized by gas phase oxygen. This type of mechanism is known as ODH redox-mechanism as described by Equation (30).



PODH has been extensively studied with vanadium-based catalysts and this in order to understand the selective pathways for propylene production¹⁰⁰⁻¹⁰⁵. Recent literature contributions reported Mars van Krevelen^{101,106} and Langmuir Hinshelwood^{60,61} mechanisms for gas phase oxygen-free

PODH. Mars van Krevelen method has little controversy for this kind of reaction whereas Langmuir-Hinshelwood can fit rate data better than Mars van Krevelen rate expression ¹⁰⁷. It was hypothesized that the dominant reaction mechanism for catalytic alkanes ODH reactions is with transition metal oxides. These reaction intermediates involve the reduction of the catalyst by adsorbed alkanes, from the gas phase with the participation of the lattice oxygen and forming olefins through several possible intermediate species. Gas phase molecular oxygen can then re-oxidize the reduced catalyst surface.

Table 3 displays literature reported activation energies value for propane ODH reactions under gas-phase oxygen-free conditions. Hossain ⁶¹ compared the kinetics of oxidative dehydrogenation (ODH) of propane to propylene over VO_x/CaO and VO_x/CaO- γ -Al₂O₃ catalysts in the absence of gas phase oxygen through the Langmuir–Hinshelwood mechanism. This author found that propylene formation using a VO_x/CaO- γ -Al₂O₃ catalyst involves a lower activation energy (120.3 kJ/mol) than the one for the VO_x/CaO (126.7 kJ/mol) catalyst. In contrast, VO_x/CaO- γ -Al₂O₃ requires higher activation energies (55.2 kJ/mol) for the undesired CO₂ formation and this while compared to the ones for VO_x/CaO catalyst (32.8 kJ/mol). These values are consistent with the product selectivity as observed in the catalyst evaluation experiments.

Ghamdi et al. ¹⁰¹ reported the kinetic modeling of propane oxidative dehydrogenation (ODH) via a Mars van Krevelen mechanism. The calculated pre-exponential factors (k_1^0 , k_2^0 , and k_3^0) increased as the vanadium loading was augmented. In addition, the activation energies for CO_x formation (E_2 and E_3) were consistently smaller than the one for propylene formation (E_1).

Table 3: Activation Energies and Activity Decay Parameter Values for the Main Products from PODH Reported in Literature.

Catalyst	Activation energy of formation (kJ/mol)		Decay Parameter (λ)	Year
	C ₃ H ₆	Carbon Oxides		
10% VO _x /CaO- γ -Al ₂ O ₃ (1:1)	120.3	(CO ₂) 55.1 ^a (CO ₂) 53.7 ^b	$1.6 \times 10^{-3} \pm 0.6 \times 10^{-3}$	2017 ⁶¹
5% VO _x / γ -Al ₂ O ₃	124.92	(CO _x) 52.81 ^a (CO _x) 52.54 ^b	0.01–0.053	2014 ¹⁰¹

7% VO _x /γAl ₂ O ₃	115.08	(CO _x) 51.07 ^a	(CO _x) 52.73 ^b	0.017-0.056	2014 ¹⁰¹
10% VO _x /γAl ₂ O ₃	109.42	(CO _x) 45.58 ^a	(CO _x) 53.75 ^b	0.015-0.047	2014 ¹⁰¹

^a Formation from propane; ^b Formation from propylene.

2.4 Reactor Concepts for ODH

Adsorption and desorption during PODH reactions are governed by phases residence time, chemical species interaction with each other and with the catalyst. These matters are in turn determined by the reactor type and the operation mode. Given that PODH is an exothermic reaction, efficient heat removal from the PODH process is a major concern for the reactor operation.

2.4.1 Fixed-bed Reactors

Most of the literature studies considered fixed-bed type reactors for ODH reactions, mainly due to their simplicity^{8,40,73,108–110}. For instance, temperature gradients can hardly be eliminated in a traditional fixed-bed reactor unless the catalyst bed is diluted with inert particles using a large inert particles/catalyst particle ratio. This would greatly increase the fixed cost and would be a significant challenge for the economic industrial scale production of propylene based on the PODH process.

To overcome the exothermicity of ODH fixed-bed reactors, researchers analyzed multi-tubular reactors with periodic air injection¹¹¹, membrane reactors¹¹² and wall-cooled catalytic reactors¹¹³. The aim is to efficiently remove the generated heat from the catalyst bed. To reduce the fixed-bed reactor cost, a micro-channel reactor was utilized²¹. It is reported that the micro-channel reactor can achieve the same reactor productivity as a traditional fixed-bed reactor with less than 20% of fixed bed reactor volume. This is the case given the inherently suitable of micro-channel reactors to be used for highly exothermic reactions due to its excellent heat transfer and removal capabilities.

Recently, the catalytic performance of phase-pure M1 MoVNbTeO_x catalysts for the ODHE reaction in both a micro-channel reactor and small-sized fixed-bed reactor under same conditions

was investigated²¹. This comparison was carried out to demonstrate the advantages of the micro-channel reactors for improved heat management. XRD, SEM and ICP characterization indicated that the M1-PVA catalyst plate has a high stability in the micro-channel system.

2.4.2 Twin Circulating Fluidized-bed Reactors for PODH

Due to the several shortcomings of the fixed-bed reactors, the use of circulating fluidized bed reactors and more specifically downer reactors for ODH have received much attention recently^{3,60,114}. Downer reactors if operated with fine particles in the 60-100 micron range, provide controlled thermal change and narrow particle and residence times, allowing ODH with high olefin selectivity⁶⁷.

In ODH, under oxygen-free atmospheres and once the surface lattice oxygen has been exhausted, the rate of water formation decreases. This occurs with a gradual increase in the formation of molecular H₂, which in turn slows down the ODH reaction. Therefore, catalyst re-oxidation (regeneration) is necessary^{45,61,93,108,115,116}. In ODH, periodic catalyst re-oxidations are required and as a result the ODH process can be viewed as a system of twin fluidized reactors: an oxidative dehydrogenation reactor and a re-oxidation reactor^{12,59,61}. In these ODH systems, the gas phase oxygen is never allowed to reach the oxidative dehydrogenation unit, thus limiting the possibility of complete combustion of the propane feed and propylene product.

Thus, a remaining outstanding challenge for ODH is to have available fluidizable catalysts with high selective towards propylene formation and catalyst able to supply oxygen for dehydrogenation. Therefore, the most important characteristics of a successful ODH catalyst is their activity in the ODH reactor and their reactivity in the re-oxidation cycle. In addition the fluidizable ODH catalysts should be stable under repeated reduction/oxidation cycles, be resistant to agglomeration, be able to withstand the friction stress associated with high circulation of particles and be environmentally benign and affordable.

2.4.3 Circulating Fluidized-bed Reactors Models for PODH

The technical literature reports a mathematical model for PODH. The model was based on a two-phase fluidized bed reactor representation⁶⁸. The model used kinetics for a V-Mg oxide catalyst. Simulations showed that temperature, pressure, feed composition, particle size and gas velocity

were all factors affecting propane conversion and selectivity. The model was validated using previously published experimental data of circulating fluidized bed reactor unit.

Recently, Rostom et al. as described in Chapter 7: CPFD Simulation, reported a downer fluidized bed reactor simulation using a hybrid CPFD Barracuda which represents the catalyst particles as particle clusters. A kinetic model established using experimental data, was incorporated in the simulation. Data showed the good propane conversion and propylene selectivity prospects in an industrial scale unit.

2.4.4 Experimental Laboratory Reactor for PODH

The CREC Riser Simulator ¹¹⁷, is a bench-scale mini-fluidized bed reactor (50 cm³). It provides conditions equivalent to those of a twin circulating fluidized reactor process (reactor–regenerator). Promising paraffin conversions and olefin selectivities have already been demonstrated by CREC researchers by using this reactor. In the CREC Riser Simulator, VO_x/c-Al₂O₃ ⁷⁸, VO_x-MoO_x/γ-Al₂O₃ ³, VO_x-Nb/La-γ-Al₂O₃ ⁹, VO_x/ γ-Al₂O₃-ZrO₂ ^{54,56,118} catalysts were used for ethane ODH. VO_x/ γ-Al₂O₃ ¹² and VO_x/CaO- γ-Al₂O₃ ^{10,61} catalysts were used in propane ODH in the same reactor in the absence of gas phase oxygen. This reactor operates under batch conditions and is designed for catalyst evaluation and kinetic studies under fluidized bed (riser/downer) reactor conditions. One of the main advantages of this unit is its capability to simulate fluidized bed reactions conditions by using a very small amount of catalyst. Details of this reactor is discussed in Chapter 4: Experimental Methods and Apparatus.

Regarding the studies with the CREC Riser Simulator, two modes of operation can be considered: a) Single injections with catalyst regeneration in between cycles and b) Successive multiple injections without catalyst regeneration. These types of possible operation are discussed in the upcoming sections.

2.4.4.1 Single Propane Injection

A single propane injection in the CREC Riser Simulator allows one to understand the interaction between the alkane feed and a fully oxidized catalyst. Thus in these experiments, the catalyst is repeatedly reduced when reacting with the alkane and then re-oxidized by air at various reaction temperatures and contact times. Following every reaction injection, the catalyst is regenerated with

air. Therefore, every time the catalyst is regenerated, the PODH is mainly driven by non-selective oxygen species on the catalyst surface. This could involve loosely bound lattice oxygen from the catalyst surface or weakly adsorbed oxygen species^{59,61}. This loosely bound lattice oxygen is considered more reactive, and thus, likely to cause carbon-carbon bond breakage and promote total oxidation. As a result, both types of oxygen species may contribute to the total oxidation of propane and lead to the low propylene selectivity. Therefore, it can be concluded that fully oxidized (fresh) catalysts are active but not selective for propane ODH reactions¹². Thus, single injections followed by catalyst re-oxidation show the value of using an optimized catalyst, where the density of the oxygen species on the catalysts surface is controlled. This is significant to achieve higher propylene selective.

2.4.4.2 Successive Propane Injection

To overcome the problem of single injection experiments where propylene selectivity is an issue, successive propane injections can be implemented. Here, the PODH catalyst is progressively reduced via the consecutive alkane injections and propylene selectivity is gradually augmented. As mentioned, there is no catalyst regeneration between the injections.

With this data and for each of the injections, the instantaneous conversion and selectivities for the main products can be calculated. Furthermore, the degree of reduction of the catalyst can be defined as the ratio of the remaining oxygen in the catalyst after each injection to the original oxygen content of the catalyst. The former can be determined by analyzing the various oxygen-containing products resulting from each alkane injection. The latter can be calculated from the oxygen uptake of the O₂-chemisorption characterization technique.

In this respect, researchers reported high propylene selectivity and good propane conversion following the second and third successive injection^{12,59,61}. This is the result given that, due to successive injections, weakly adsorbed oxygen depletes quickly. Furthermore, only the catalyst lattice oxygen drives the PODH reaction.

2.5 PODH Industrial Prospects

As shown in below section, the PODH process shall involve a catalyst is circulated between a PODH reactor and a catalyst regenerator units. After leaving the PODH reactor, the catalyst is

divided into two parts using a splitter. Using this device, a major portion of the catalyst is recirculated back to the PODH reactor with a smaller fraction going to the regenerator (1/10 times) to be reactivated. In this way, a partially reduced catalyst is always maintained circulating in between the systems. This reactor configuration helps to overcome the influence of combustion reactions, which increases as a result of overall propylene selectivity. It is envisioned that this industrial scale downer reactor for PODH will involve a 20-m length with 2.8-3.5 m/s particle cluster velocities and contact times in the 5-7 s range.

2.6 Computational Particle Fluid Dynamic Study for Propane ODH Process

Circulating fluidized beds (CFB) have been used as an efficient gas-solid contact reactors in a broad range of applications, namely, coal combustion, biomass gasification, fluid catalytic cracking (FCC) and others^{119,120}. Regarding downer units, gas and particulates move concurrently downwards, in the same direction as gravity. As a result, a more uniform radial gas and a solid flow structure are expected¹²¹⁻¹²³. Downer reactors offer significant advantages over concurrent up-flow CFBs (risers). This is the case given that downer reactors overcome the severe solid back-mixing occurring in riser reactors¹²⁴ (back-mixing in riser due to non-uniform gas and solid flow).

The use of downer reactors in fluid catalytic cracking processes is reported in the literature^{121,125}, indicating flow field with limited phase segregation. In a downer, different phases (gas and solids) can aggregate to form transient structures. These structures designated as “particle clusters” can be affected by system boundaries and by particle interactions. Lanza et al. reported “individual clusters” in downer reactors¹²⁶, with radial and axial solid distributions. To clarify this issue, CREC-GS-Optiprobes¹²⁷⁻¹²⁹ were implemented to study the gas-solid concurrent downflow reactor hydrodynamics. In particular and with the help of CREC-GS-Optiprobes, particle/cluster velocities as well as cluster sizes were measured.

Computational Fluid Dynamic techniques are increasingly used in the oil and gas industry for the purpose of process optimization and scale-up¹²⁰. Computational Particle Fluid Dynamic (CPFD) is also used in fluidization research due to their capacity to provide far more detailed hydrodynamics and reaction information of fluidization systems than experimental approaches¹³⁰. Using the CPFD, however allows one to develop calculations using an Eulerian computational grid for the gas phase and a Lagrangian numerical particle grid for the particle phase. The particle

phase is accounted for by using a particle probability distribution function. The particle momentum equation is based on a multiphase particle-in-cell (MP-PIC) method¹³¹⁻¹³³. In this regard, the use of CPFDF, for downer simulations, has significant advantages as it describes the particle-fluid patterns and special flow features including inherent rotational flow properties¹³⁴.

To address the issue of the PODH process development in the context of downflow reactors, our research group at the CREC-University of Western Ontario, Canada has led to the implementation of a PODH circulating bed process involving a downer unit and a dense phase fluidizable regenerator⁵⁹. Figure 3 describes the proposed PODH process in a set of fluidized bed reactors. The PODH reaction is performed in a downer reactor unit while the catalyst oxidation occurs in a dense phase fluidized regenerator. Propane is fed via two levels of injectors at the downer entry section level where it meets the PODH catalyst. It is in the downer where the PODH reactions along with the propane combustion reaction take place. Then, the partially reduced catalyst particles and gases enter the “terminator” cyclone (Cyclone-2) where product gases and particles are separated. Following this, catalyst particles exit the “Terminator Cyclone” via a cyclone dipleg ending in a splitter unit, where solids are divided into two streams: a) a major stream which is recirculated back to the downer and b) a smaller stream which is directed to the regenerator for catalyst re-oxidation. Once catalyst particles are re-oxidized in the regenerator, they are returned to the “feeding cyclone” (Cyclone-1) via a transport line. Here, re-oxidized particles join the catalyst particle flow fraction which is recirculated directly from the “Terminator Cyclone”.

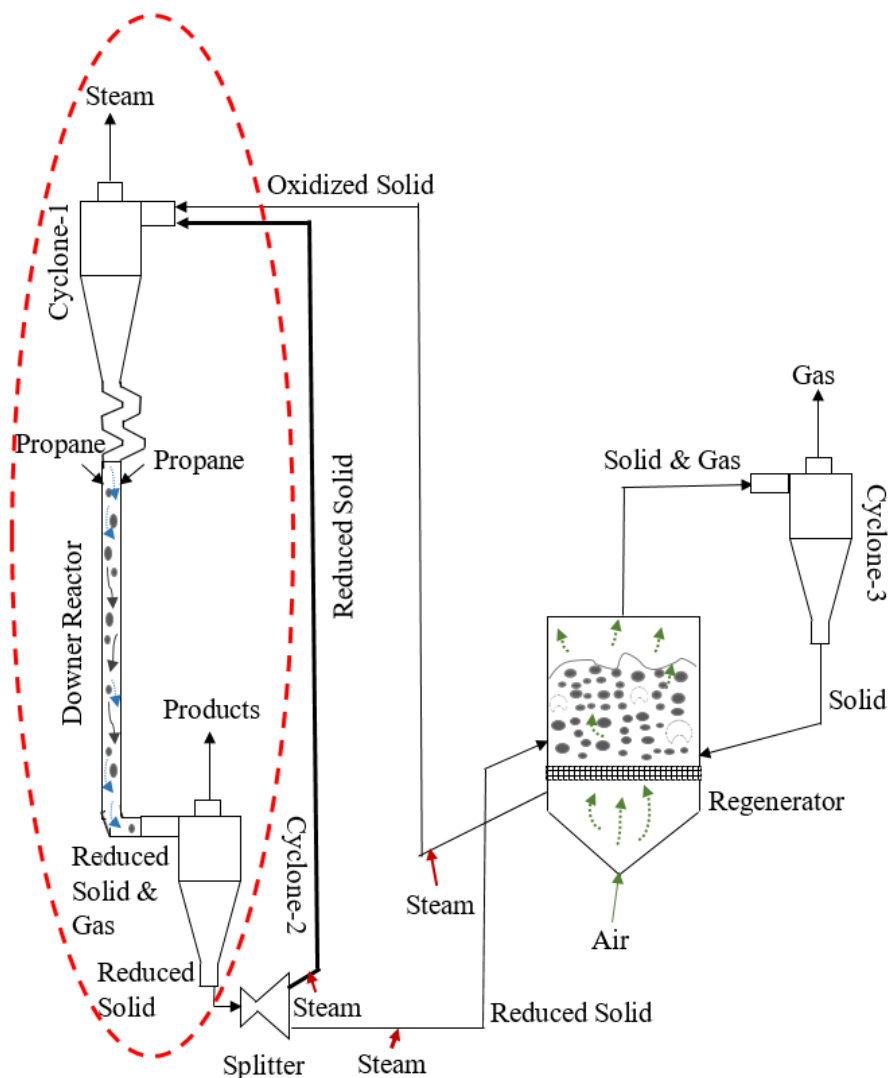


Figure 3: Schematic PODH Process Flow Sheet ⁵⁹. The process components inside the red marked section are considered in the simulation study (Details in Chapter 7).

2.7 Conclusions

Based on the information provided in this review chapter, it can be concluded that:

- a) Propane oxidative dehydrogenation reactions under gas phase oxygen-free atmosphere are thermodynamically favored;
- b) Vanadium-based catalysts supported on variety of fluidizable supports can be utilized to develop a suitable propane oxidative dehydrogenation process. This fluidizable catalysts can supply the lattice oxygen required for high olefins selectivity;

- c) A variety of reaction mechanisms and kinetic models can be considered for PODH. However, if one aims to develop a PODH leading to high propylene selectivity, special experimental devices such as the CREC Riser Simulator must be used.
- d) This approach provides kinetic models that will represent the PODH, under the conditions of successive propane injections, which are the most favorable ones for high propylene selectivity.
- e) An appropriate reactor selection for PODH is also an important aspect to establish PODH at the commercial scale. In this respect, special reactor configurations involving downer reactors with partial catalyst regeneration are favored to achieve high propylene selectivities in a continuous process.
- f) Industrial scale downer fluidized bed reactor simulation requires the use of hybrid CPFDD computational accounting for particle cluster flow.

Chapter 3: Scope of Research

3.1 Objectives

The goal of this study is to provide an in-depth study on a novel vanadium-based fluidizable catalyst for the propane oxidative dehydrogenation under the gas phase oxygen free atmosphere. This will include the reactivity of the ODH catalysts, its stability, its propane conversion kinetics and also the behavior in the large scale simulation.

As a result, the specific proposed objectives for this PhD research are set as follows:

- 1) The preparation of new fluidizable $\text{VO}_x/\text{ZrO}_2\text{-}\gamma\text{Al}_2\text{O}_3$ (1:1 wt. %) catalysts with varying vanadium content (2.5, 5 and 7.5 wt. % Vanadium) for propane ODH and compare those with the corresponding $\text{VO}_x/\gamma\text{Al}_2\text{O}_3$ catalysts. The catalysts will be prepared by wet-saturation impregnation technique with a close control of acidity and Brønsted sites.
- 2) The prepared catalysts will be characterized by various techniques to understand the surface properties. For that, most advanced surface characterization techniques such as BET, XRD, H_2 -TPR, NH_3 -TPD, Pyridine FTIR, LRS, and XPS will be used.
- 3) The development of reaction runs to establish various $\text{VO}_x/\text{ZrO}_2\text{-}\gamma\text{Al}_2\text{O}_3$ (1:1 wt. %) catalysts performances for propane ODH under fluidized bed reaction conditions in the CREC Riser Simulator reactor. The experimental runs will be developed to examine the effects of reaction temperature and contact times on the ODH reactions.
- 4) The effect of vanadium loading and their molecular structures on PODH reactions will be analyzed.
- 5) Mechanistic steps involved in the catalytic propane oxidative dehydrogenation with pure propane feed under molecular oxygen free conditions will be studied.
- 6) The development of heterogeneous kinetic model that describes the product gas compositions during catalytic PODH will be established.
- 7) Intrinsic kinetic parameters (i.e. activation energies and pre-exponential factors) for the proposed kinetic models will be estimated using non-linear regression analysis.
- 8) Developed kinetic model will be used in a twin circulating fluidized bed reactors for large scale simulation using CPFDF Barracuda. A BarracudaTM CPFDF code, which uses a commercial software for gas/particle flow simulations. The CPFDF code incorporates both

reaction and adsorption phenomena, and allows the rigorous coupling of gas and catalyst phases in the downer unit.

3.2 Accomplishments of Research Objectives

The accomplishments of the research objectives of the present PhD dissertation are reflected in two published manuscripts and one submitted manuscript in reputed chemical engineering journals as follows:

a) Manuscript 1: **Rostom, S.**; de Lasa, H. I. Propane Oxidative Dehydrogenation Using Consecutive Feed Injections and Fluidizable $\text{VO}_x/\gamma\text{Al}_2\text{O}_3$ and $\text{VO}_x/\text{ZrO}_2-\gamma\text{Al}_2\text{O}_3$ Catalysts. *Ind. Eng. Chem. Res.* **2017**, 56 (45), pp 13109–13124, **DOI:** 10.1021/acs.iecr.7b01369, Publication Date (Web): May 22, 2017

This manuscript considers, as reported in Chapter 4 and 5 of this thesis, catalysts preparation, characterizations and reactivity studies in the CREC Riser Simulator.

b) Manuscript 2: **Rostom, S.**; de Lasa, H. High Propylene Selectivity via Propane Oxidative Dehydrogenation Using a Novel Fluidizable Catalyst: Kinetic Modeling. *Ind. Eng. Chem. Res.* **2018**, 57 (31), pp 10251–10260, **DOI:** 10.1021/acs.iecr.8b01891, Publication Date (Web): July 12, 2018

This paper considers the development of a heterogeneous kinetic model based on Langmuir-Hinshelwood for catalytic propane ODH. Details of this model are reported in Chapter 6.

c) Manuscript 3, entitled “Downer Fluidized Bed Reactor Modeling for Catalytic Propane Oxidative Dehydrogenation with High Propylene Selectivity”. This article was recently submitted to *Chemical Engineering and Processing: Process Intensification Journal* and is now under review.

This manuscript considers, the large scale simulation of propane ODH process including a downer fluidized bed reactor using the CPFDD Barracuda software. Various findings of this manuscript are reported in Chapter 7.

Chapter 4: Experimental Methods and Apparatus

This chapter describes the experimental procedures of catalyst synthesis, characterizations and evaluation techniques for propane oxidative dehydrogenation (PODH).

4.1 Catalysts Preparation

Several PODH catalysts were prepared with different vanadium loadings (2.5, 5 and 7.5 wt. %). Vanadium was dispersed over $\gamma\text{Al}_2\text{O}_3$ and $\text{ZrO}_2\text{-}\gamma\text{Al}_2\text{O}_3$ by a wet saturation impregnation technique. This technique allows VO_x species to be highly dispersed on the catalyst surface. This method has been demonstrated as preferable for industrial catalyst applications¹³⁵.

In the case of the $\text{VO}_x/\text{ZrO}_2\text{-}\gamma\text{Al}_2\text{O}_3$ catalyst, before the vanadium loading, the $\gamma\text{Al}_2\text{O}_3$ (10 g) (SASOL, Catalox® SSCa 5/200) was wet impregnated with ZrO_2 ($\text{ZrO}_2:\gamma\text{Al}_2\text{O}_3=1:1$ wt. %). To accomplish this, the $\gamma\text{Al}_2\text{O}_3$ support was dried at 140°C to remove the moisture. Then, in a beaker, the desired amount of ZrCl_4 (20 g) (Sigma Aldrich, 99.5%) was dissolved with ethanol (33.0 ml) (Commercial Alcohols, Anhydrous). Following this, $\gamma\text{Al}_2\text{O}_3$ was contacted with this mixture, under continuous stirring. The solvent was then evaporated under a vacuum and the resulting cake was dried in a vacuum at 120°C for 8 h. Finally, the particles were calcined under an air stream at 650°C for 8 h.

Furthermore, and to achieve an optimal vanadium loading, oxalic acid (Sigma Aldrich, 99%) (2.0 g) was mixed with distilled water (13.0 ml). After continuous stirring, this gave a translucent solution. Ammonium metavanadate (NH_4VO_3) (Sigma Aldrich, 99%) (1.0 g) was then added to the clear solution keeping the pH ~ 2 ¹². The acidity of the solution was chosen to improve precursor solubility. This led to better vanadium oxide dispersion on the support¹³⁶. After the addition of NH_4VO_3 , the color of the solution changed progressively from white to orange-red, and finally to a gray-green. After stirring and heating, the solution color became brilliant blue¹³⁷. Then, the prepared solution was added to the previously prepared $\text{ZrO}_2\text{-}\gamma\text{Al}_2\text{O}_3$ support (in case of $\text{VO}_x/\gamma\text{Al}_2\text{O}_3$, the support is only $\gamma\text{Al}_2\text{O}_3$). This was done under continuous stirring. Following this step, the solvent was evaporated under vacuum pressure to minimize metal loading losses. Then, the resulting solids were dried and calcined by following the same procedure used for zirconia

loading. In this way, different percentages (2.5, 5.0 and 7.5 wt. %) of vanadium were loaded on the $\gamma\text{Al}_2\text{O}_3$ and $\text{ZrO}_2\text{-}\gamma\text{Al}_2\text{O}_3$ (1:1) supports.

4.2 Catalyst Characterizations

4.2.1 Brunauer–Emmett–Teller (BET) Surface Area

Specific surface areas and pore size distributions of the prepared catalysts were calculated using the Brunauer, Emmett and Teller method (BET). Nitrogen adsorption-desorption was developed at 77K in an ASAP 2010 Analyzer. Before each measurement, a 0.15-0.25 g catalyst sample was degassed at 250°C for 2 h. Adsorption isotherms were measured in the relative pressure range of 0.04-1 at 77 K.

4.2.2 X-ray Diffraction (XRD)

XRD patterns were obtained by using an Ultima IV instrument from Rigaku Instruments. This XRD diffractometer is equipped with a monochromatic $\text{Cu K}\alpha$ radiation source (wavelength=0.15406 nm, 40 kV, 40 mA). It provides a scan rate of 2° per minute, in the 10° to 80° 2 θ scale with a 0.02° resolution.

4.2.3 Temperature-Programmed Reduction (TPR)

Temperature programmed reduction (TPR) was performed by using a Micromeritics Autochem II 2920 Analyzer. During each experiment, 140-150 mg of catalyst sample was in contact with a 10% H_2/Ar gas mixture at a flow rate of 50 ml/min. The sample was heated at a 15°C/min rate until it reached 900°C. Hydrogen consumption was monitored using a thermal conductivity detector (TCD). The amount of hydrogen uptake by the sample can be calculated via numerical integration of the TPR area. TPR analysis allows establishing available lattice oxygen for PODH.

4.2.4 Temperature-Programmed Desorption of Ammonia (NH_3 -TPD)

NH_3 -TPD analysis is available in the Autochem II Analyzer from Micromeritics. For each experiment, an amount of 180-200 mg of catalyst sample was first pretreated for 1 h at 650°C with a helium flow at a flow rate of 50 ml/min. Then, the sample was cooled to 100°C and brought to saturation using a 5% NH_3/He gas mixture, at a 50 ml/min flow rate for 1 h. After that, ammonia

flow was switched off. Then, 50 ml/min of pure inert gas (He) at 100°C was contacted with the catalyst for 1h extra, to remove the physically adsorbed ammonia. The temperature was then raised up to 650°C at a rate of 15°C/min, with ammonia being desorbed progressively. Regarding NH₃ concentration in the effluent gas, it was monitored by using a thermal conductivity detector (TCD). On this basis the total acidity was established by accounting for the total amount of ammonia desorbed from the catalyst.

4.2.5 Pyridine Fourier Transform Infrared Spectroscopy (FTIR)

Catalyst surface acid site type can be determined using Fourier Transform Infrared Spectroscopy (FTIR) and by utilizing pyridine as probe molecule. Before the analysis, the catalyst sample was dried for 2 h under N₂ flow at 550°C and then cooled to 100°C. The samples was kept at 100°C and saturated with pyridine using a N₂ stream containing pyridine. The adsorption of pyridine was allowed for 1 h. Then, the samples were flushed with pure N₂ at 100°C for 90 min, in order to remove weakly adsorbed pyridine. The catalyst samples were dispersed on a sodium chloride window. Following this, samples were analyzed by Fourier Transform Infrared Spectroscopy (FTIR) using a Bruker Hyperion 2000 microscope attached to a Tensor II main box.

4.2.6 Laser Raman Spectroscopy (LRS)

Laser Raman Spectroscopy (LRS) was employed to establish vanadium oxide surface species (VO_x) state on γ -Al₂O₃ and ZrO₂- γ -Al₂O₃. Laser Raman spectra were obtained using a Renishaw InVia Reflex Raman spectrometer equipped with a 633 nm laser and an 1800 I/mm grating. The spectra were collected in the static mode with the spectra centre placed at 775 cm⁻¹ (~ 8mW at the sample). Spectra were recorded for 10 seconds or 30 seconds periods, with these periods being a function of the signal strength.

4.2.7 X-ray Photoelectron Spectroscopy (XPS)

XPS measurements were performed to quantify elements on the surface of the VO_x/ γ -Al₂O₃ and VO_x/ZrO₂- γ -Al₂O₃ catalysts. The XPS analyses were carried out with a Kratos Axis Ultra spectrometer using a monochromatic Al K (alpha) source (15mA, 14kV). Survey scan analyses were carried out with an analysis area of 300 x 700 microns and a pass energy of 160 eV. High resolution analyses were carried out with an analysis area of 300 x 700 microns and a pass energy

of 20 eV, with the main line of the carbon 1s spectrum (adventitious carbon) set to 284.8 eV. Spectra were analyzed using a CasaXPS software (version 2.3.14).

4.3 PODH Catalytic Test

The catalytic reaction runs of propane oxidative dehydrogenation over supported vanadium oxide catalyst samples were developed using the Chemical Reactor Engineering Center (CREC) Riser Simulator ¹¹⁷.

Thermal and catalytic runs of propane ODH were carried out at three different temperatures (500, 525 and 550°C), three contact times (10, 15 and 20 seconds) and a 44.0 catalyst/propane weight ratio (g/g). Catalytic propane ODH runs were studied under an O₂-free atmosphere where the only oxygen source was the catalyst lattice oxygen. To achieve this, successive injection experiments were considered. These experiments were used to change the catalyst state from completely oxidized to partially reduced.

All thermal and catalytic runs were repeated three times. This was done to ensure the reproducibility of results. The carbon mass balance closures, which considered all carbon containing products such as carbon monoxide, methane, carbon dioxide, ethylene, ethane, propylene, propane and carbon deposited over the catalyst, were found in all cases to be higher than 95%.

4.3.1 Experimental Apparatus

A schematic diagram of the CREC Riser Simulator Reactor System is provided in Figure 4. The main reactor consists of a lower shell and an upper shell. These two shells allow easy access to the reactor to load and unload catalyst samples. The lower shell houses a basket that contains the catalyst sample. This creates an annulus in between the catalyst basket and lower shell section. The catalyst basket is bound by two grids, trapping the catalyst and restraining its mobility within this chamber. There is as well also an impeller located in the upper reactor section. The impeller rotation provides both a suction effect as well as a compression, moving the gas in the upward direction through the inside of the basket and downward direction through the outer annulus. A metallic gasket is used to seal the upper and the lower shells of the reactor. A packing gland assembly with a cooling jacket supports and seals the impeller shaft. Upon the rotation of the impeller at high speed (up to 7500 rpm), gas is forced both outward in the impeller section and

downwards in the outer reactor annulus, causing the solids material (catalyst) to become fully fluidized. (Computational fluid dynamics mixing pattern study of the CREC Riser Simulator is reported in a recent literature ¹³⁸)

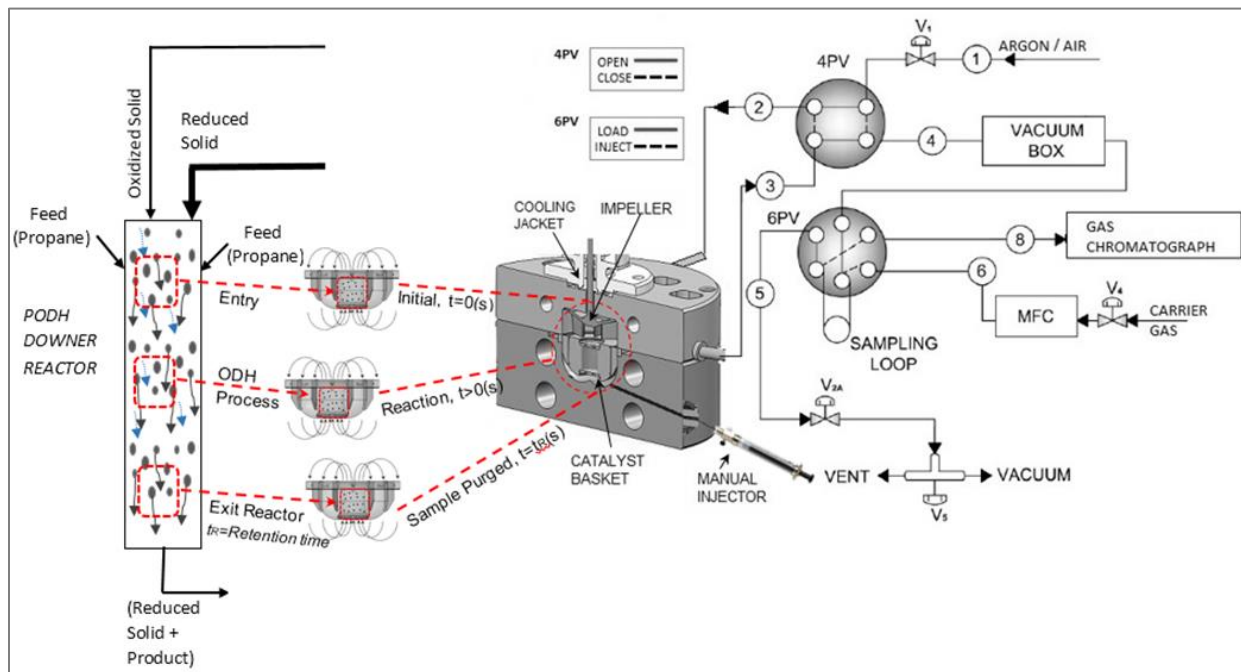


Figure 4: Schematic diagram of CREC Riser Simulator reactor system⁵⁹.

The CREC Riser Simulator connects with other accessories such as a vacuum box, a gas chromatograph (GC), a series of sampling valves, a timer, two pressure transducers and two temperature controllers. A timer is linked to an actuator, which operates the four-port valve. The timer is used to set the reaction time for an experimental run. It starts with the manual injection of the feed, and when the pre-set time expires, the reactor is evacuated to the vacuum box through the four-port valve. The evacuation process is almost instantaneous because of the significant pressure difference between the reactor and the vacuum box. Consequently, the reaction is terminated with the evacuation of the reactor. The vacuum box, a stainless-steel cylinder with a capacity of 1068 cm³, is connected with the reactor by the four-port valve that enables the connection-isolation of the reactor and the vacuum box. The vacuum box collects product and helps to transfer the product sample into a gas sampling loop while the six-port valve (6PV) is in the “load” mode. After loading the sample into the sample loop, the product gas is directed to the gas chromatograph (GC) for further analysis while having the 6PV in the “inject” mode.

Two pressure transducers (Omega PX303-050A5) rated at 50 psia maximum pressure are installed in both the reactor and vacuum box to allow the monitoring of the pressure during the experiment, as well as to make sure that complete and instantaneous evacuation occurs in the reactor. Both of the transducers are connected to analog/digital cards, supplied by Cole Parmer (A/D, model L-08109-27). For data collection, GWBASIC code is used.

Two Omega 400 KC temperature controllers are used in order to display and control various parts of the system which includes the reactor, vacuum box, cooling jacket, flow lines etc. The temperature controllers are calibrated to work with K type Omega thermocouples. In order to display the temperature of each of the parts specified above, the input selector knob is rotated to the desired position.

The CREC Riser Simulator and auxiliary components provides altogether: a) an almost instantaneous reactant injection, b) catalytic reaction under controlled conditions, c) quick product evacuation, and d) “on-line” product analysis via gas chromatography.

4.3.2 Experimental Procedures

For each catalytic experiment, the required amount of catalyst was first loaded to the reactor basket and then reactor was closed. A temperature program was run to heat the system to the desired reaction temperature. An argon flow was maintained during the heating period to ensure that the reactor system was free from oxygen (air). Once the reactor reached the desired temperature, the argon flow was arrested and the pressure in the vacuum box brought to 2 psia using a vacuum pump. At this point, the impeller was turned on and when it reached 5300 rpm, the feed (propane) was injected into the reactor using a preloaded syringe. During this period of ODH reaction, the pressure profile of the reactor was recorded using a pressure transducer. At the end of the pre-specified reaction time, a valve isolating the reactor and the vacuum bottle was opened and the contents of the reactor were transferred to the vacuum bottle. This introduced an abrupt decrease of the reactor pressure confirming that most of the reactant and product species were removed from the reactor almost instantaneously and that no further reaction took place. Finally, the product species were analyzed using a gas chromatograph. After the ten successive propane injections with the same procedure, the catalyst sample is regenerated (oxidized) by flowing air at a specified temperature and prepared for the next cycle.

4.3.3 Thermal Runs

Thermal cracking (without catalyst) runs were performed using the empty reactor to understand clearly the catalyst effect and thermal conversion effect on the oxidative dehydrogenation reactions. The thermal runs were tested at 550°C and 20 s reaction time using the same reactant (propane).

4.3.4 Analytical System

The effluent from the reactor was analyzed online using a gas chromatograph (Shimadzu GC-2010) with argon as a carrier gas and two detectors, FID and TCD. This unit was equipped with a HayeSepD 100/120 mesh packed column. The analytical set-up was completed with a methanizer unit, where CO and CO₂ were detected as methane. Thus, the FID was used to detect all hydrocarbons species including CO and CO₂. Furthermore, hydrogen was measured using the TCD. A schematic of GC columns connections is shown in Figure 5.

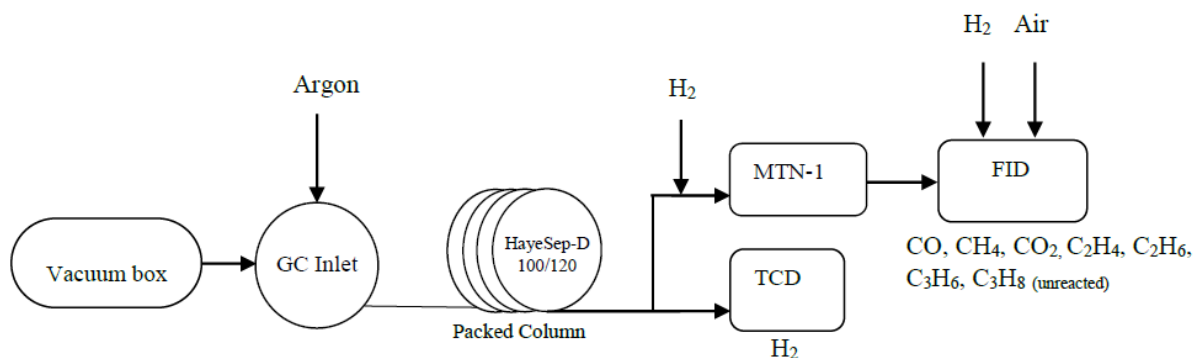


Figure 5: Schematic of GC column connections.

Argon was used as a carrier gas, whereas the FID is operated with hydrogen and synthetic air. The duration of one GC analysis is about 30 min and data acquisition was done using Shimadzu GC Solution software. Correlation between peak areas and gas correlations were established by using standard gas mixtures. The GC calibration procedures, detailed method parameters and analytical conditions used for each detector and also the temperature programming in the GC oven are given in Appendix A: GC Calibration Curves.

4.3.5 Conversion and Selectivity Calculations

The performance of the PODH catalysts was examined based on propane conversion and propylene selectivity. Although the literature reports other methods for calculating conversion and selectivity^{56,118}, a more rigorous approach based on carbon containing product species is considered in this research¹², as follows:

$$\text{Propane Conversion, } X_{\text{C}_3\text{H}_8}(\%) = \frac{\sum_i v_i n_i}{3n_{\text{propane}} + \sum_i v_i n_i} \times 100 \quad (31)$$

$$\text{Selectivity to a product, } S_i(\%) = \frac{v_i n_i}{\sum_i v_i n_i} \times 100 \quad (32)$$

$$\text{Propylene Yield (Y)} = \frac{X_{\text{C}_3\text{H}_8}(\%) \times S_{\text{C}_3\text{H}_6}(\%)}{100} \quad (33)$$

Where:

n_i = Moles of gaseous carbon containing product 'i';

v_i = Number of carbon atoms in gaseous carbon containing product 'i';

n_{propane} = Moles of unconverted propane in the product stream;

4.4 Conclusions

- a) Different PODH catalysts were prepared by wet saturation impregnation technique that allowed vanadium oxide species to be highly dispersed on the catalyst surface.
- b) Prepared PODH catalysts were characterized by several techniques to establish surface properties of these PODH catalysts.
- c) Catalysts performance runs were developed in a mini-fluidized CREC Riser Simulator reactor which is designed for catalyst evaluation and kinetic studies under fluidized bed (riser/downer) conditions.
- d) Reaction products were analyzed by a gas chromatograph using two detectors, FID and TCD with a methanizer unit. All the carbon-containing gaseous products were analysed using the FID detector while the TCD was used to establish hydrogen gas produced.

Chapter 5: Results and Discussion of the Experiments

This chapter reports the PODH catalysts characterization results along with experimental results in the CREC Riser Simulator.

5.1 Catalyst Characterizations

5.1.1 BET Surface Area

Figure 6 and Figure 7 describe the nitrogen adsorption/desorption isotherms for $\text{VO}_x/\gamma\text{Al}_2\text{O}_3$ and $\text{VO}_x/\text{ZrO}_2-\gamma\text{Al}_2\text{O}_3$ catalysts respectively. One can notice that the observed isotherms are Type IV with capillary condensation at relatively high pressures according to the IUPAC classification.

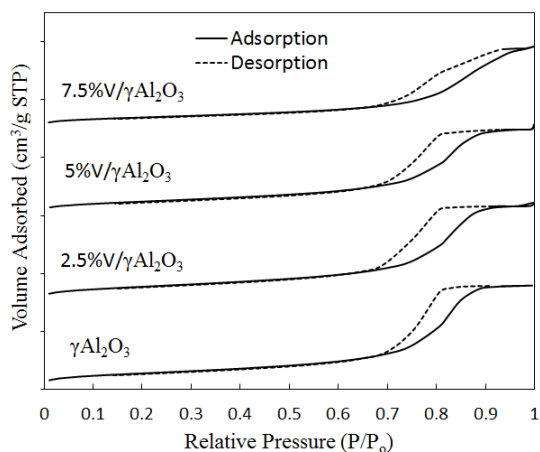


Figure 6: N_2 Adsorption-desorption isotherms for $\text{VO}_x/\gamma\text{Al}_2\text{O}_3$ catalysts.

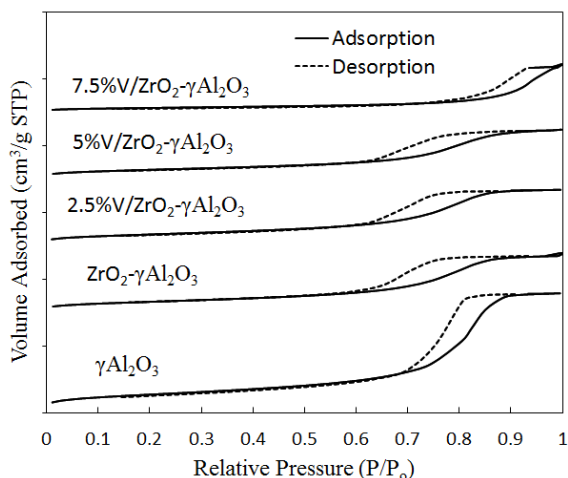


Figure 7: N_2 Adsorption-desorption isotherms for $\text{VO}_x/\text{ZrO}_2-\gamma\text{Al}_2\text{O}_3$ catalysts.

Note that, for Figure 6 and Figure 7, the unit scale used corresponds to 200 cm³/g STP of adsorbed volume. All data are in the same linear scale.

Table 4 shows the BET surface areas of the bare γ -Al₂O₃ support, of the VO_x/ γ -Al₂O₃ and of the VO_x/ZrO₂- γ -Al₂O₃ catalysts with different vanadium loadings. The specific surface area of the fresh γ -Al₂O₃ was found to be 203 m²/g. However, after successive impregnations with zirconia and vanadium, followed by calcination at 650°C for 8 h, the V and ZrO₂ loaded catalysts showed a gradual decrease of surface area. This reduction can be ascribed to the blocking of some of the smaller alumina pores with ZrO₂ and VO_x species. For the 7.5%V/ZrO₂- γ -Al₂O₃ catalyst, the specific surface area was reduced to 50 m²/g.

It is assumed that this decrease in specific surface area for 7.5%V/ZrO₂- γ -Al₂O₃ catalyst was the result of the phase transformation of zirconia from tetragonal to monoclinic or alternatively, the result of the formation of ZrV₂O₇ crystals on the catalysts' surface¹³⁹. This crystal phase may also contribute to the increase of the catalyst average pore diameters.

Table 4: BET Specific surface area, pore volume and average pore diameter for the bare γ -Al₂O₃ and the various prepared catalysts.

Sample	S _{BET} (m ² /g)	V _{pore} (cc/g)	Avg. Pore Dia. (Å)
γ -Al ₂ O ₃	203	0.56	109
2.5%V/ γ -Al ₂ O ₃	200	0.52	103
5%V/ γ -Al ₂ O ₃	177	0.46	105
7.5%V/ γ -Al ₂ O ₃	141	0.43	121
ZrO ₂ : γ -Al ₂ O ₃ (1:1)	133	0.28	85
2.5%V/ZrO ₂ - γ -Al ₂ O ₃	128	0.26	82
5%V/ZrO ₂ - γ -Al ₂ O ₃	105	0.23	86
7.5%V/ZrO ₂ - γ -Al ₂ O ₃	50	0.20	164

Figure 8 and Figure 9 report the pore size distribution (PSD) of the VO_x/ γ -Al₂O₃ and VO_x/ZrO₂- γ -Al₂O₃ catalysts respectively. One can observe both in Table 4 and Figure 8, that the γ -Al₂O₃ displayed an average pore diameter of 109 Å. As well, one can notice that, after loading 2.5 and 5

wt. % V on $\gamma\text{Al}_2\text{O}_3$, the average pore diameter remained essentially unchanged. It was only once the vanadium loading reached 7.5 wt. % V on the $\gamma\text{Al}_2\text{O}_3$ that the average pore diameter varied slightly to 121 Å. This pore diameter change took place with a modest reduction of pore volume.

However and, for the $\text{VO}_x/\text{ZrO}_2-\gamma\text{Al}_2\text{O}_3$, the average pore diameter was reduced from 109 Å to 82-86 Å (Table 4 and Figure 9). This was the case for both the 2.5 and 5 wt. % V/ $\text{ZrO}_2-\gamma\text{Al}_2\text{O}_3$ catalysts. Furthermore, for the 7.5 wt. % V/ $\text{ZrO}_2-\gamma\text{Al}_2\text{O}_3$, the average pore size diameter augmented to 164 Å with a corresponding loss of the smaller pores and pore volume reduction.

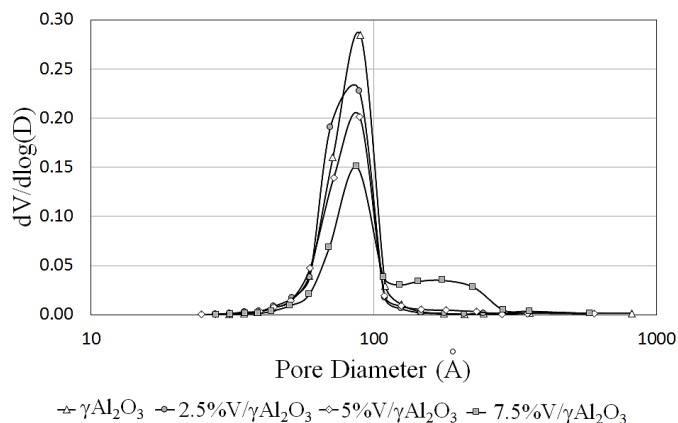


Figure 8: Pore Size Distribution of the $\gamma\text{Al}_2\text{O}_3$ Support and the $\text{VO}_x/\gamma\text{Al}_2\text{O}_3$ Catalyst Samples as determined from Nitrogen Desorption Isotherms.

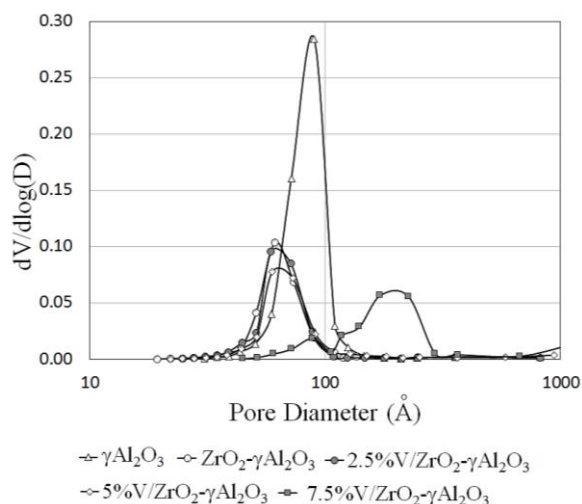


Figure 9: Pore Size Distribution of the $\gamma\text{Al}_2\text{O}_3$ and $\text{ZrO}_2-\gamma\text{Al}_2\text{O}_3$ Supports and the $\text{VO}_x/\text{ZrO}_2-\gamma\text{Al}_2\text{O}_3$ Catalyst Samples as Determined from Nitrogen Desorption Isotherms.

5.1.2 XRD

Al-Ghamdi et al.¹² reports XRD patterns for the $\gamma\text{Al}_2\text{O}_3$ support and for $\text{VO}_x/\gamma\text{Al}_2\text{O}_3$ catalysts with different vanadium loadings. Consistent with previous technical literature, no diffraction lines were observed for the vanadium oxide species in the $\text{VO}_x/\gamma\text{Al}_2\text{O}_3$ samples. This provides support to the view that VO_x species consists of a dispersed amorphous phase on the γ -alumina or V_2O_5 may present as small crystalline nanoparticles (<4 nm) which is undetectable by XRD¹². Only $\gamma\text{Al}_2\text{O}_3$ peaks were observed at positions of 46° and 67° of the 2θ scales for these catalysts.

Figure 10 shows the diffraction peaks of the $\gamma\text{Al}_2\text{O}_3$ and zirconia modified alumina support for various $\text{VO}_x/\text{ZrO}_2\text{-}\gamma\text{Al}_2\text{O}_3$ catalysts.

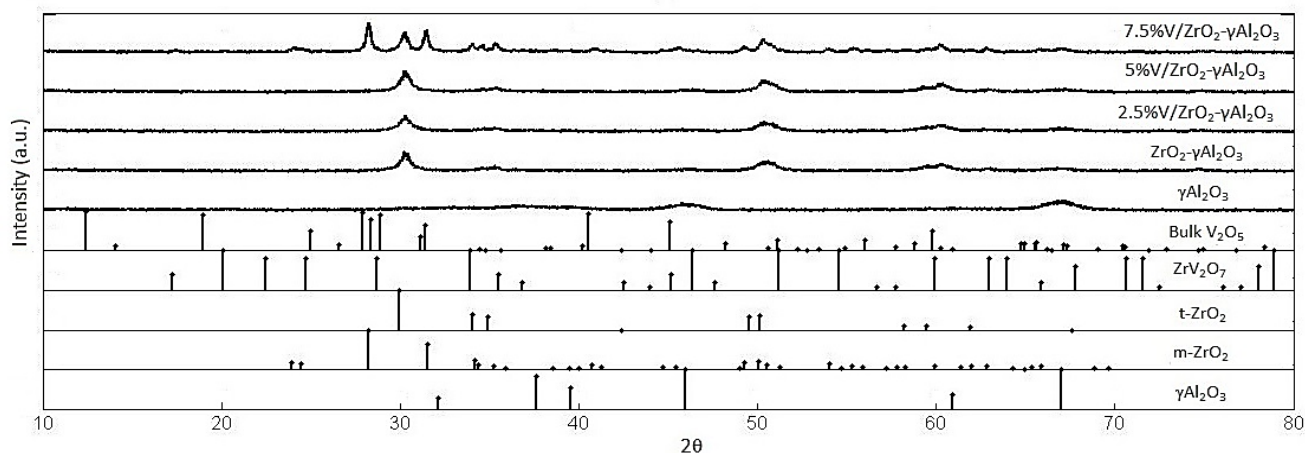


Figure 10: XRD patterns for the $\gamma\text{Al}_2\text{O}_3$ and the $\text{ZrO}_2\text{-}\gamma\text{Al}_2\text{O}_3$ supports as well as those for the $\text{VO}_x/\text{ZrO}_2\text{-}\gamma\text{Al}_2\text{O}_3$ catalysts with different vanadium loadings.

In Figure 10, the XRD diffractograms for bulk V_2O_5 , ZrV_2O_7 complex, $t\text{-ZrO}_2$, $m\text{-ZrO}_2$ and $\gamma\text{Al}_2\text{O}_3$ JCPDS data are also shown as a reference. Note that, all reported intensity data are in the same linear scale.

It can be observed from Figure 10 that for $\text{ZrO}_2\text{-}\gamma\text{Al}_2\text{O}_3$, 2.5%V/ $\text{ZrO}_2\text{-}\gamma\text{Al}_2\text{O}_3$ and 5%V/ $\text{ZrO}_2\text{-}\gamma\text{Al}_2\text{O}_3$, there were four observable peaks at 30° , 36° , 51° and 61° of the 2θ scale. These peaks can be assigned to the tetragonal zirconia phase¹⁴⁰. However, when vanadium loading reached 7.5% V on the $\text{ZrO}_2\text{-}\gamma\text{Al}_2\text{O}_3$ support, monoclinic zirconia peaks were observed at 28.5° , 31° , 35° and 41° in the 2θ scale¹⁴⁰. Thus, at 2.5 and 5% vanadium, surface-dispersed vanadium oxide species were

formed, leading to the transformation of the zirconia from an amorphous to a tetragonal phase. At higher vanadium loadings, though, the tetragonal zirconia phase changed to monoclinic. Furthermore, in this case, one can notice that there were no detectable diffraction lines corresponding to the vanadium oxide.

Moreover, and in order to establish the structural stability of the two sets of catalysts prepared, XRD was performed using spent catalysts, after 10 successive propane injections performed at 550°C and 20 seconds reaction time. Figure 11 and Figure 12 report the XRD patterns of the spent $\text{VO}_x/\gamma\text{Al}_2\text{O}_3$ and $\text{VO}_x/\text{ZrO}_2-\gamma\text{Al}_2\text{O}_3$ catalysts.

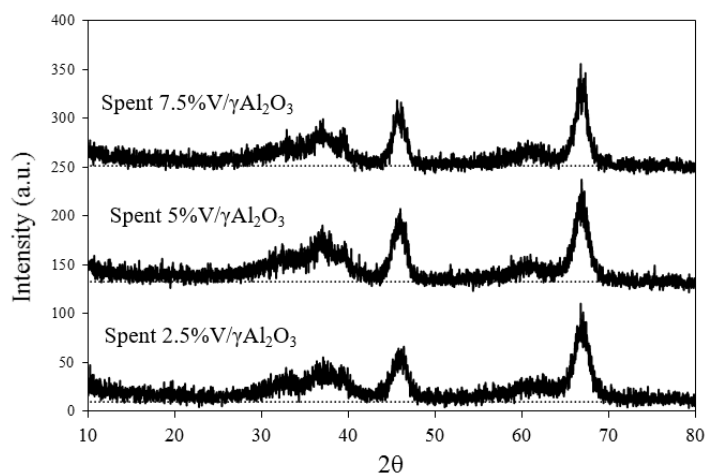


Figure 11: XRD patterns for the spent $\text{VO}_x/\gamma\text{Al}_2\text{O}_3$ catalysts with different vanadium loadings after 10 consecutive propane injections.

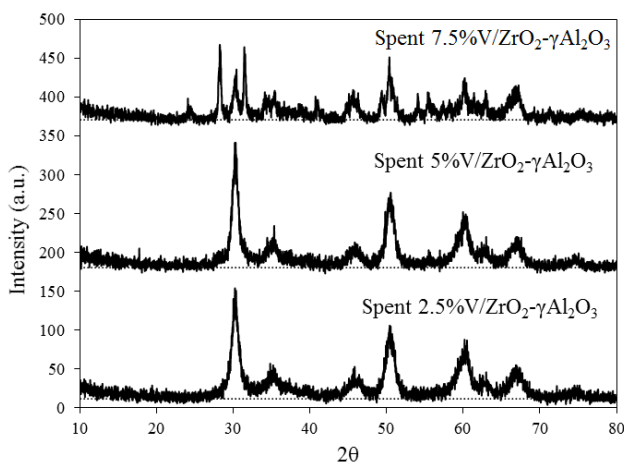


Figure 12: XRD patterns for the spent $\text{VO}_x/\text{ZrO}_2-\gamma\text{Al}_2\text{O}_3$ catalysts with different vanadium loadings after 10 consecutive propane injections.

For Figure 11 and Figure 12, the selected operation conditions were: a) $T=550^{\circ}\text{C}$; b) reaction time= 20s; c) propane injected= 10 ml and d) catalyst loaded= 0.76 g. Note that, reported signals represent deviations from baseline (dotted line).

One can notice, in the XRD diffraction of Figure 11 that for the spent $\text{VO}_x/\gamma\text{Al}_2\text{O}_3$ catalysts, peaks at 46° and 67° of the 2θ scale were only observable for the bare $\gamma\text{Al}_2\text{O}_3$. For the $\text{VO}_x/\text{ZrO}_2\text{-}\gamma\text{Al}_2\text{O}_3$ spent catalysts (Figure 12) however, the XRD observable peaks were assigned to m- ZrO_2 , t- ZrO_2 and $\gamma\text{Al}_2\text{O}_3$. These XRD peaks were the same as the ones recorded for the fresh catalysts. Thus, this indicates that there was no structural change after the catalyst was used under reaction conditions, proving the PODH catalyst stability.

5.1.3 H_2 -TPR and Degree of Reduction

TPR experiments were used to investigate the reducibility of vanadium oxide surface species deposited on the $\gamma\text{Al}_2\text{O}_3$ and $\text{ZrO}_2\text{-}\gamma\text{Al}_2\text{O}_3$. Figure 13 and Figure 14 describe the H_2 -TPR profiles during the first catalyst reduction cycle.

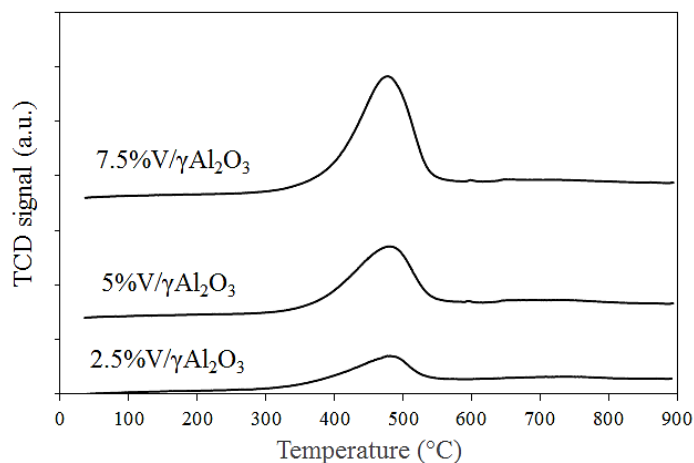


Figure 13: H_2 -TPR profile of calcined $\text{VO}_x/\gamma\text{Al}_2\text{O}_3$ catalyst samples for the first reduction cycle.

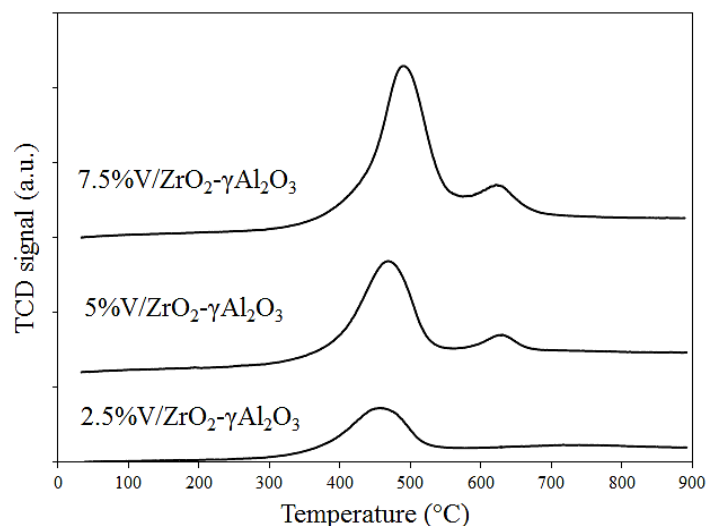


Figure 14: H₂-TPR profile of the calcined VO_x/ZrO₂- γ Al₂O₃ catalyst samples for the first reduction cycle.

Regarding Figure 13 and Figure 14, the following operating conditions were chosen: a) Temperature increasing up to 900°C with a 15°C/min heating rate; b) Reducing Agent: 10 mole% H₂/Ar at 50 cm³/min; c) Oxidizing Agent: 5 mole% O₂/He at 50 cm³/min. Note that, all reported TCD signal data are in the same linear scale.

Regarding the reducibility of vanadium-based catalysts, it was observed that, for VO_x/ γ Al₂O₃ catalysts (Figure 13), there is only one symmetric reduction peak extending from 300°C to 600°C with a T_{max} between 475 and 485°C. The presence of a single reduction peak in these catalysts was attributed to the reduction of V⁺⁵ to V⁺⁴ species¹⁴¹.

On the other hand, zirconia over γ Al₂O₃ shows no TPR peak. This result is consistent with the technical literature¹⁴⁰. Furthermore, the 2.5%V/ZrO₂- γ Al₂O₃ displayed a single peak at 453°C, while the 5 and 7.5V%/ZrO₂- γ Al₂O₃ catalysts showed two TPR peaks with the second peak located between 625-630°C (Figure 14).

Table 5: TPR data comparing hydrogen consumption in the first reduction cycle using catalysts with varying amounts of vanadium (wt. %). All TPR analyses were repeated at least 3 times.

Catalysts	T _{max} (°C)		H ₂ Uptake (cm ³ STP/g)
	T ₁	T ₂	
2.5% V/ γ -Al ₂ O ₃	481	-	6.07
5.0 % V/ γ -Al ₂ O ₃	479	-	13.67
7.5% V/ γ -Al ₂ O ₃	477	-	22.62
2.5% V/ZrO ₂ - γ -Al ₂ O ₃	453	-	6.96
5.0 % V/ZrO ₂ - γ -Al ₂ O ₃	468	628	16.15
7.5% V/ZrO ₂ - γ -Al ₂ O ₃	490	625	25.90

Table 5 shows the hydrogen consumption and the reduction temperatures at the TPR maximum of the prepared catalysts. One can observe that, for vanadium loadings of 5 and 7.5 wt. %, the VO_x/ZrO₂- γ -Al₂O₃ catalysts showed higher hydrogen consumption than the catalyst without zirconia. As well, one can observe that the VO_x/ZrO₂- γ -Al₂O₃ catalysts displayed a higher T_{max} with an increased V content. This means that by increasing vanadium loading, and given the enhanced metal-support interaction, oxygen is released in a more controlled manner in the case of the 7.5% V/ZrO₂- γ -Al₂O₃. This is required for highly selective propylene production.

Furthermore, one can also notice in Figure 14, a second TPR peak for both 5% V/ZrO₂- γ -Al₂O₃ and 7.5% V/ZrO₂- γ -Al₂O₃ catalysts. This points towards a two stage reduction with extra hydrogen consumption.

Regarding PODH catalyst stability, the best 7.5% V/ZrO₂- γ -Al₂O₃ performing catalyst was checked via consecutive TPR-TPO cycles. Figure 15 reports TPR for five consecutive cycles.

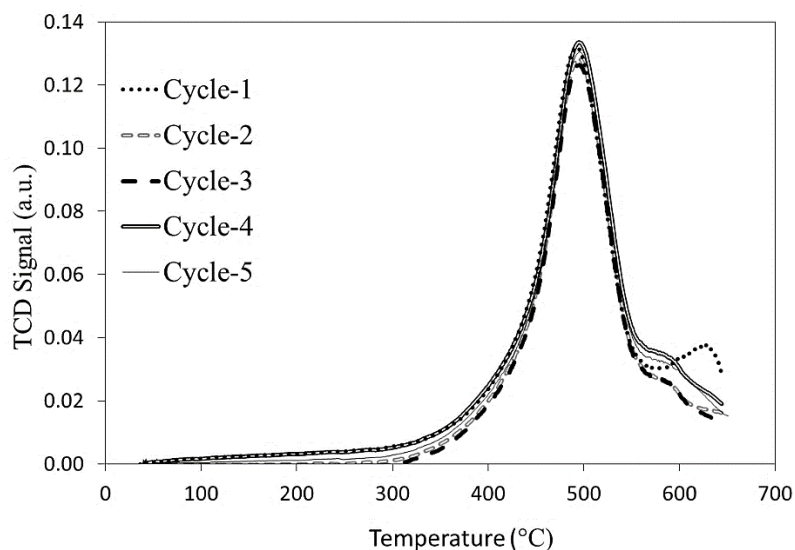


Figure 15: Consecutive TPR/TPO for the 7.5% V/ZrO₂- γ Al₂O₃ Catalyst.

Concerning for Figure 15, the following operating conditions were selected: a) Temperature increases up to 650°C with a 15°C/min heating rate; b) Reducing Agent: 10 mole% H₂/Ar at 50 cm³/min; c) Oxidizing Agent: 5 mole% O₂/He at 50 cm³/min.

It is proven with the TPR data of Figure 15 that, with the only exception of the double peak for the 1st cycle, all other consecutive cycles displayed single and unchanged TPR peaks. Consistent with this, the double TPR peaks for the first TPR were attributed to ZrV₂O₇ crystals, observed using Raman Spectroscopy as will be described later in this article.

Furthermore, once this first cycle was completed, the vanadium species gave a stable single H₂ consumption peak. This single peak remained unchanged for the various TPR's in the sequence. Every sequence was repeated at least 3 times, giving a hydrogen consumption very close to 22.0±5% cm³/g STP.

5.1.4 NH₃-TPD

Surface acidity is a very important property of supported vanadia catalysts of the present study. Surface acidity is governed by the nature of the support used and the structure of surface vanadia species (VO_x). Thus, a correlation of surface acidity with the structure of the supported vanadia is important to understand the PODH catalytic activity.

NH₃-TPD was used in this study, to assess total acidity and acid strength of the bare γ -Al₂O₃ and compare to that of the VO_x/ γ Al₂O₃ and VO_x/ZrO₂- γ Al₂O₃ catalyst samples with different vanadium loadings. Figure 16 and Figure 17 report the relationship between the thermal conductivity of the desorbed species (NH₃ pre-adsorbed at 100°C) with a linear increase in temperature (15°C/min) of the VO_x/ γ Al₂O₃ and VO_x/ZrO₂- γ Al₂O₃ catalyst samples, respectively.

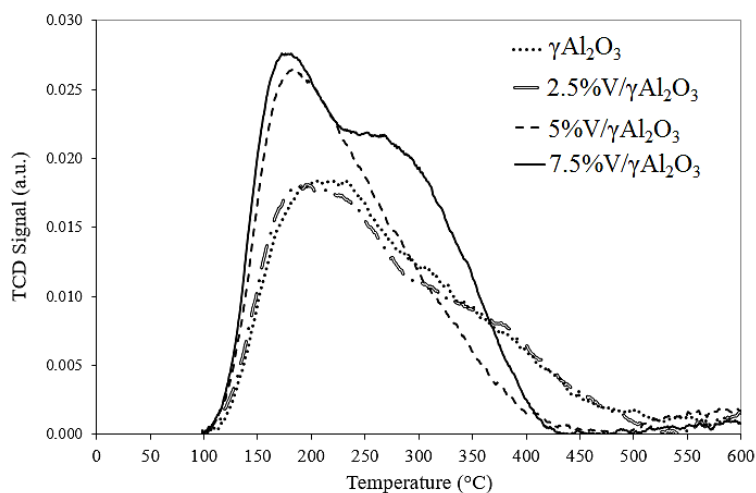


Figure 16: NH₃-Temperature Programmed Desorption profiles for γ Al₂O₃ and various VO_x/ γ Al₂O₃ Catalyst Samples (Heating rate: 15°C/min; NH₃ adsorbed at 100°C).

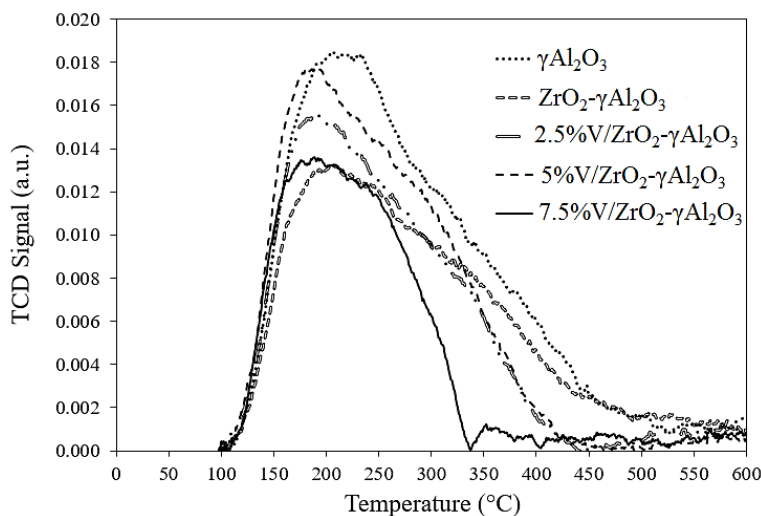


Figure 17: NH₃-Temperature Programmed Desorption profiles for γ Al₂O₃, ZrO₂- γ Al₂O₃ and various VO_x/ZrO₂- γ Al₂O₃ Catalyst Samples (Heating rate: 15°C/min; NH₃ adsorbed at 100°C).

It can be observed in Figure 16, that for the VO_x/ γ Al₂O₃ catalysts, increasing the vanadium loading augments the NH₃ uptake showing an increased acidity in the catalyst samples (e.g. 2.5%V/ γ Al₂O₃

acidity is close to that of $\gamma\text{Al}_2\text{O}_3$). However, and as shown in Figure 17, $\text{VO}_x/\text{ZrO}_2\text{-}\gamma\text{Al}_2\text{O}_3$ acidity remained low and almost constant, with this being true when increasing vanadium loadings. These effects can be explained considering that ZrO_2 , with a lower acidity than alumina can block acid sites of the $\gamma\text{-Al}_2\text{O}_3$ diminishing total acidity^{56,118}.

Table 6 shows ammonia uptake by various samples and their desorption temperatures (T_{des}). The total acidity of each catalyst sample was established on the basis of the integration of desorbed NH_3 as given by the TCD (temperature conductivity detector) profiles.

Table 6: Temperature Programmed Desorption of NH_3 for $\text{VO}_x/\gamma\text{Al}_2\text{O}_3$ and $\text{VO}_x/\text{ZrO}_2\text{-}\gamma\text{Al}_2\text{O}_3$ catalyst samples. The $\gamma\text{-Al}_2\text{O}_3$ and $\text{ZrO}_2\text{-}\gamma\text{Al}_2\text{O}_3$ Supports are provided as a reference.

Catalysts	T_{des} (°C)	NH_3 Uptake (cm^3 STP/g)
$\gamma\text{Al}_2\text{O}_3$	221	6.03
2.5%V/ $\gamma\text{Al}_2\text{O}_3$	185	5.87
5.0 %V/ $\gamma\text{Al}_2\text{O}_3$	182	6.62
7.5%V/ $\gamma\text{Al}_2\text{O}_3$	176, 271	8.35
$\text{ZrO}_2\text{-}\gamma\text{Al}_2\text{O}_3$	209	4.73
2.5% V/ $\text{ZrO}_2\text{-}\gamma\text{Al}_2\text{O}_3$	187	4.50
5.0 % V/ $\text{ZrO}_2\text{-}\gamma\text{Al}_2\text{O}_3$	185	5.04
7.5% V/ $\text{ZrO}_2\text{-}\gamma\text{Al}_2\text{O}_3$	179	3.56

Table 6 also reports that $\text{VO}_x/\text{ZrO}_2\text{-}\gamma\text{Al}_2\text{O}_3$ display a decreasing maximum desorption temperature with increasing vanadium loading. Thus, based on this, one can anticipate that enhanced desorption properties at higher vanadium loadings. This can indeed facilitate product species desorption, reducing the chances of further propylene oxidation. Thus, both lower desorption temperatures and lower acidity are favorable for PODH¹⁴². Furthermore, and given that the $\text{VO}_x/\gamma\text{Al}_2\text{O}_3$ catalyst displays higher acidity than $\text{VO}_x/\text{ZrO}_2\text{-}\gamma\text{Al}_2\text{O}_3$ catalyst, it is expected that the $\text{VO}_x/\gamma\text{Al}_2\text{O}_3$ catalyst will produce more cracking products and more carbon deposition on the catalyst surface which will lead to catalyst deactivation.

5.1.5 Pyridine FTIR

Given that the best propylene selectivities were found when using 7.5%V/ γ Al₂O₃ and 7.5%V/ZrO₂- γ Al₂O₃ catalysts, further pyridine FTIR characterizations of these two catalyst were performed. Figure 18 shows the FTIR spectra of the 7.5%V/ γ Al₂O₃ and 7.5%V/ZrO₂- γ Al₂O₃ catalysts.

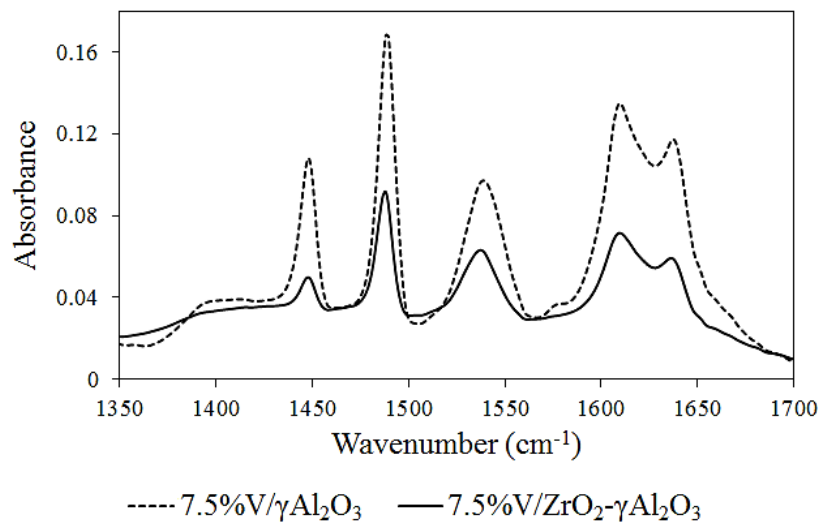


Figure 18: Pyridine FTIR Spectra of the 7.5%V/ γ Al₂O₃ and 7.5%V/ZrO₂- γ Al₂O₃ Catalysts.

One can observe in Figure 18 that both 7.5%V/ γ Al₂O₃ and 7.5%V/ZrO₂- γ Al₂O₃ catalysts exhibit FTIR bands at 1448 and 1540 cm⁻¹. Regarding the 1448 cm⁻¹ band, it can be assigned to surface Lewis acid sites while the 1540 cm⁻¹ can be assigned to Brønsted acid sites. Furthermore, the several bands observed in the spectral region between 1580 and 1660 cm⁻¹ can be allocated to hydrogen-bonded pyridine while the bands at 1490 cm⁻¹ attributed to both Lewis and Brønsted acid species^{143,144}.

By reviewing Figure 18, one can establish the total number of Brønsted sites and Lewis sites in the two catalysts. On this basis, one can establish that the 7.5%V/ γ Al₂O₃ contains a higher combined density of Lewis and Brønsted acid sites than the 7.5%V/ZrO₂- γ Al₂O₃ catalyst. This means that the 7.5%V/ γ Al₂O₃ catalyst is more acidic than the 7.5%V/ZrO₂- γ Al₂O₃ catalyst, with these results agreeing with NH₃-TPD.

Furthermore, the pyridine FTIR peaks at 1448 and 1540 cm^{-1} were used to quantify the Brønsted sites over the Lewis sites ratio. Table 7 reports Brønsted/Lewis ratios for the 7.5%V/ $\gamma\text{Al}_2\text{O}_3$ and the 7.5%V/ $\text{ZrO}_2\text{-}\gamma\text{Al}_2\text{O}_3$ catalysts. These ratios are 0.94 and 2.21 respectively, indicating an increased abundance of Brønsted over Lewis acid sites in the 7.5%V/ $\text{ZrO}_2\text{-}\gamma\text{Al}_2\text{O}_3$ catalyst.

As for PODH, a low acidity with dominant Brønsted acid sites is a desirable condition. This can contribute in facilitating rapid propylene desorption, avoiding as a result, further propylene oxidation to CO_x . In conclusion, pyridine FTIR also points towards the 7.5%V/ $\text{ZrO}_2\text{-}\gamma\text{Al}_2\text{O}_3$ as being a very suitable catalyst for PODH.

Table 7: Acid Properties of 7.5%V/ $\gamma\text{Al}_2\text{O}_3$ and 7.5%V/ $\text{ZrO}_2\text{-}\gamma\text{Al}_2\text{O}_3$ Catalyst Samples Using Pyridine FTIR.

Catalyst	Bronsted/Lewis sites
7.5%V/ $\gamma\text{Al}_2\text{O}_3$	0.94
7.5%V/ $\text{ZrO}_2\text{-}\gamma\text{Al}_2\text{O}_3$	2.21

5.1.6 Laser Raman Spectroscopy

Raman Spectroscopy is a powerful and versatile technique for characterizing vanadium oxide¹³⁶. Figure 19 reports the Raman spectra for different samples. One can notice that the $\gamma\text{Al}_2\text{O}_3$ support does not exhibit any Raman bands in the 100-1100 cm^{-1} region due to the ionic character of the Al-O bonds¹⁴⁵. Furthermore, the 7.5%V/ $\gamma\text{Al}_2\text{O}_3$ shows a narrow peaks at 1010-1030 cm^{-1} which is assigned to the stretching mode of the V=O bond in the isolated monovanadate surface species¹⁴⁶. It also shows a broad band from 750-1000 cm^{-1} which can be attributed to polyvanadate species. This indicates the coexistence of both mono and polyvanadate species on the $\gamma\text{Al}_2\text{O}_3$ support.

For the $\text{ZrO}_2\text{-}\gamma\text{Al}_2\text{O}_3$ samples, Raman peaks were observed at 149, 274, 322, 464, 606 and 652 cm^{-1} . These peaks were be assigned to a tetragonal zirconia phase^{140,147}. Furthermore, when 7.5% V is loaded on the $\text{ZrO}_2\text{-}\text{Al}_2\text{O}_3$ support, peaks for tetragonal zirconia, V=O bond and monoclinic zirconia species were observed at 178, 190, 225, 339, 382 and 639 cm^{-1} . As well, ZrV_2O_7 peaks were also recorded at 780 and 991 cm^{-1} ^{100,146}. Except for ZrV_2O_7 , all the mentioned species were detected with XRD. Therefore, it can be concluded that the ZrV_2O_7 observed belongs to a class of

small crystals undetectable by XRD. One can also notice that none of the catalysts studied showed 180, 235, 325, 345, 448, 520, 567 and 993 cm^{-1} Raman peaks, which can be assigned to bulk V_2O_5 crystals. These findings point towards the absence of a V_2O_5 crystalline phase.

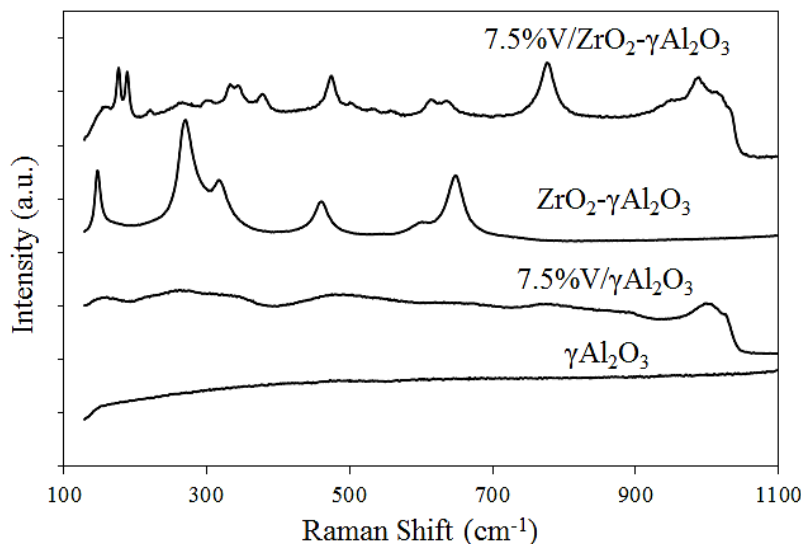


Figure 19: Dehydrated Raman Spectra for $\gamma\text{Al}_2\text{O}_3$, 7.5%V/ $\gamma\text{Al}_2\text{O}_3$, ZrO_2 - $\gamma\text{Al}_2\text{O}_3$ and 7.5%V/ ZrO_2 - $\gamma\text{Al}_2\text{O}_3$. Note: All reported intensity data are in the same linear scale.

5.1.7 X-Ray Photoelectron Spectroscopy (XPS)

X-ray Photoelectron Spectroscopy (XPS) is a highly surface sensitive technique. It is considered as one of the best techniques for studying the dispersion of V_2O_5 on various supports. The nature of the surface species of the 7.5%V/ $\gamma\text{Al}_2\text{O}_3$ and 7.5%V/ ZrO_2 - $\gamma\text{Al}_2\text{O}_3$ catalysts were investigated by the XPS technique.

Figure 20 and Figure 21 report the XPS for 7.5%V/ $\gamma\text{Al}_2\text{O}_3$ and 7.5%V/ ZrO_2 - $\gamma\text{Al}_2\text{O}_3$ catalysts respectively. The V 2p 3/2 photoelectron peaks of vanadia were consistently observed at 517 and 518 eV, and assigned to the V 2p 3/2 V (IV) and V 2p 3/2 V (V) states⁸⁸. Thus, for both of the fresh catalysts, V^{+4} and V^{+5} oxidation states can be assumed to be present.

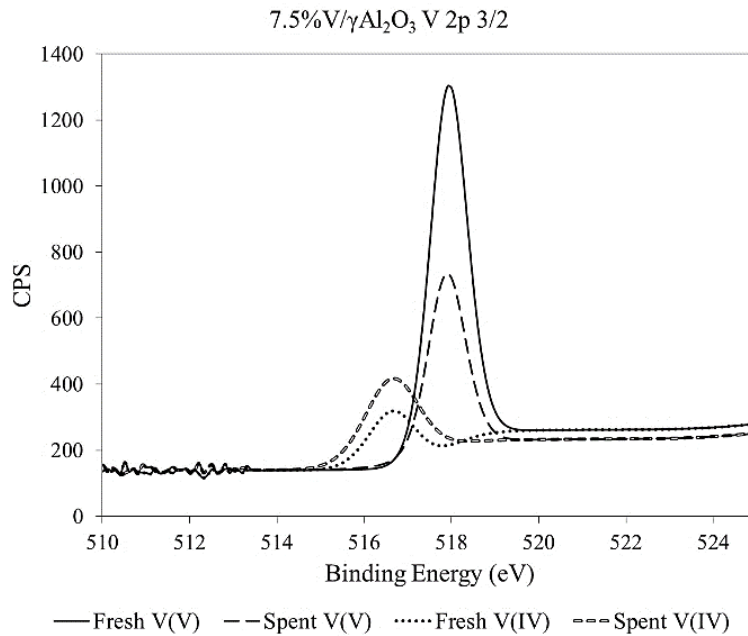


Figure 20: XPS Analysis of the 7.5%V/ γ Al₂O₃ Catalyst (fresh and spent catalysts).

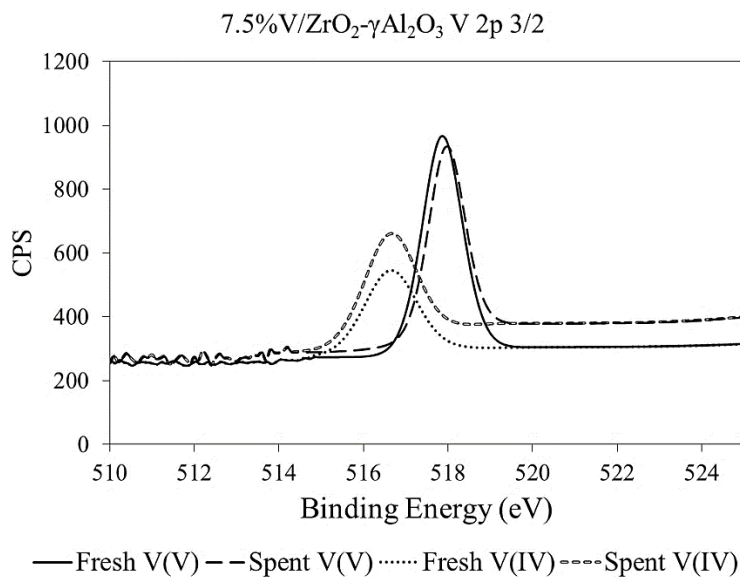


Figure 21: XPS Analysis of the 7.5%V/ZrO₂- γ Al₂O₃ Catalyst (fresh and spent catalysts).

For Figure 20 and Figure 21, operating conditions for the spent catalyst were: a) T=550°C; b) reaction time=20 s; c) C₃H₈ injected= 10 ml; d) catalyst loaded=0.76 g.

Given that the two catalysts were prepared with the same vanadium loadings of 7.5 wt. % V, V⁺⁵/V⁺⁴ can be compared using XPS areas ratios. In this respect, one can notice that the fresh

7.5%V/ γ Al₂O₃ catalyst, displays a V⁺⁵/V⁺⁴ ratio of 4.88 which points towards a larger abundance of V₂O₅ versus V₂O₄ species. However, one can also see that the fresh 7.5%V/ZrO₂- γ Al₂O₃ catalyst shows a V⁺⁵/V⁺⁴ ratio of 1.86 only (Table 8). This means that in the fresh 7.5%V/ZrO₂- γ Al₂O₃, V⁺⁵ is a dominant species, with this standing being reduced when compared to the fresh 7.5%V/ γ Al₂O₃ catalyst.

Furthermore and as shown in Table 8, the spent 7.5%V/ γ Al₂O₃ and 7.5%V/ZrO₂- γ Al₂O₃ catalysts, show reduced V⁺⁵/V⁺⁴ ratios at 1.38 and 1.13 levels, respectively.

Table 8: XPS Data of the 7.5%V/ γ Al₂O₃ and 7.5%V/ZrO₂- γ Al₂O₃ Catalysts (fresh and spent)

Catalysts	V 2p 3/2 (area%)
	V(V)/V(IV)
7.5%V/ γ Al ₂ O ₃ (Fresh)	4.88
7.5%V/ γ Al ₂ O ₃ (spent)	1.38
7.5%V/ZrO ₂ - γ Al ₂ O ₃ (Fresh)	1.86
7.5%V/ZrO ₂ - γ Al ₂ O ₃ (spent)	1.13

Regarding V⁵⁺, it has been reported as essential for the initial activation of alkanes, as for example, in the oxidative dehydrogenation of propane to propylene¹⁴⁶. However, excessive V⁵⁺ can also be responsible for the over oxidation of alkanes reducing propylene selectivity. Thus, this explains the importance of a good V⁺⁵ and V⁺⁴ balance as that found in the 7.5%V/ZrO₂- γ Al₂O₃ catalysts.

Furthermore, the formation of partially reduced vanadium species (V⁺⁴) in the VO_x/ZrO₂- γ Al₂O₃ catalysts, could also be correlated to the formation of isolated VO_x species with strong vanadium-support interactions⁸⁸. These VO_x species may have limited side interactions, which are known to favor the formation of polyvanadates or V₂O₅ crystallites.

5.2 TPD Kinetics and Heat of Desorption

The NH₃-TPD data was used in the present study to establish desorption kinetic parameters such as desorption energy E_{des} and the frequency factor k_{des0}. The calculation of desorption kinetic parameters is important to assess the metal-support interactions. The NH₃-TPD data can be modeled as described in the literature⁷⁸ and used to estimate these parameters under the following assumptions:

- I. Homogeneous catalyst surface, with $k_d = k_{des0} \exp\left(\frac{-E_{des}}{RT}\right)$, being independent of the surface coverage (θ_{ads});
- II. Ammonia does not re-adsorb during TPD experiment;
- III. Adsorbate concentration is constant in the carrier gas flow;
- IV. Adsorption rate is first order with respect to surface coverage;
- V. Temperature increases linearly with time.

In order to comply with these assumptions, a high gas flow rate was maintained during the experiments. Thus, the rate of NH₃ desorption can be expressed as¹⁴⁸:

$$r_{des} = -V_m \left(\frac{d\theta_{ads}}{dt} \right) = k_{des0} \theta_{ads} \exp \left[\frac{-E_{des}}{R} \left(\frac{1}{T} - \frac{1}{T_m} \right) \right] \quad (34)$$

Where,

θ_{ads} = fraction of surface covered by adsorbed species;

k_d = the desorption constant, $\left(\frac{\text{cm}^3}{\text{g}_{cat} \times \text{min}} \right)$;

k_{des0} = the pre-exponential factor, $\left(\frac{\text{cm}^3}{\text{g}_{cat} \times \text{min}} \right)$;

T_m = the centering temperature which minimizes the cross-correlation between parameters (k);

E_{des} = the activation energy of desorption (KJ/mol);

By raising the temperature gradually at a constant value of β' ($^{\circ}\text{C}/\text{min}$), the following equation can be used:

$$T = T_o + \beta' t \quad (35)$$

$$\frac{dT}{dt} = \beta' \quad (36)$$

$$\left(\frac{d\theta_{ads}}{dt} \right) = \left(\frac{d\theta_{ads}}{dT} \right) \left(\frac{dT}{dt} \right) = \beta' \left(\frac{d\theta_{ads}}{dT} \right) \quad (37)$$

$$\left(\frac{d\theta_{ads}}{dT} \right) = - \frac{k_{des0}}{V_m \beta'} \theta_{ads} \exp \left[\frac{-E_{des}}{R} \left(\frac{1}{T} - \frac{1}{T_m} \right) \right] \quad (38)$$

where, $\theta_{\text{ads}} = 1 - \frac{V_{\text{des}}}{V_{\text{m}}}$; V_{des} = volume of ammonia desorbed ($\text{cm}^3/\text{g}_{\text{cat}}$); V_{m} = volume of ammonia adsorbed at saturation conditions ($\text{cm}^3/\text{g}_{\text{cat}}$)

And finally,

$$\left(\frac{dV_{\text{des}}}{dT}\right) = \frac{k_{\text{des}0}}{\beta'} \left(1 - \frac{V_{\text{des}}}{V_{\text{m}}}\right) \exp\left[\frac{-E_{\text{des}}}{R} \left(\frac{1}{T} - \frac{1}{T_{\text{m}}}\right)\right] \quad (39)$$

The above equation was fitted to the experimental data using the Mathematica Nonlinear Model Fit built-in function at a heating rate of $15^\circ\text{C}/\text{min}$ for all samples. In addition, the above differential equation was solved using the ODE45 (in MATLAB, 4th order Runge-Kutta) least square method.

Table 9 reports activation energies for the various fresh catalysts of the present study and their spans for the 95% confidence intervals which never exceeds the $\pm 2.60\%$. One should also note that cross-correlation coefficients (γ) in the cross-correlation matrix never surpassed the value of ± 0.50 . Furthermore, the R^2 regression coefficients, as reported in Table 9, remained very close to one. Thus, various statistical parameters as required for desorption model applicability are in the adequate range in all cases.

One can observe in Table 9 that the vanadium supported on $\text{ZrO}_2\text{-}\gamma\text{Al}_2\text{O}_3$ catalysts displays a 22-29 KJ/mole activation energy and a 0.43-0.49 $\text{cm}^3/\text{g}_{\text{cat}}\cdot\text{min}$ frequency factor. These parameters are higher and lower than the 17-22 KJ/mole and 0.45-0.70 $\text{cm}^3/\text{g}_{\text{cat}}\cdot\text{min}$, observed for vanadium supported on bare alumina. This consistently suggests a strong interaction between the vanadium species and the $\text{ZrO}_2\text{-}\gamma\text{Al}_2\text{O}_3$ support. These results are also consistent with the relatively low observed acidity of the $\text{VO}_x/\text{ZrO}_2\text{-}\gamma\text{Al}_2\text{O}_3$ catalyst samples.

Table 9: Estimated Desorption Kinetic Parameters for NH₃-TPD Kinetics (NH₃ adsorption at 100°C). Activation energies and k_{des0} are reported with the spans for the 95% confidence intervals.

Catalysts	k_{des0} (cm ³ /g _{cat} ·min)	E_{des} (KJ/mol)	R^2	γ
γ Al ₂ O ₃	0.586 ± (0.94%)	16.72 ± (2.54%)	0.996	0.13
2.5%V/ γ Al ₂ O ₃	0.452 ± (1.06%)	17.03 ± (2.47%)	0.996	-0.49
5.0 %V/ γ Al ₂ O ₃	0.698 ± (1.09%)	22.00 ± (2.55%)	0.997	-0.24
7.5%V/ γ Al ₂ O ₃	0.673 ± (0.97%)	20.96 ± (2.03%)	0.998	-0.48
ZrO ₂ - γ Al ₂ O ₃	0.386 ± (0.88%)	14.30 ± (2.59%)	0.996	-0.23
2.5% V/ZrO ₂ - γ Al ₂ O ₃	0.432 ± (0.95%)	22.08 ± (2.14%)	0.997	-0.31
5.0 % V/ZrO ₂ - γ Al ₂ O ₃	0.492 ± (0.92%)	24.00 ± (1.85%)	0.998	0.06
7.5% V/ZrO ₂ - γ Al ₂ O ₃	0.479 ± (0.96%)	29.75 ± (2.02%)	0.998	0.08

5.3 PODH in the CREC Riser Simulator

Propane ODH experiments were developed in a CREC Riser Simulator operated under a batch reactor mode and fluidized bed conditions. The fluidizability of the various VO_x/ γ Al₂O₃ and VO_x/ZrO₂- γ Al₂O₃ catalyst samples used in this study, was ensured in the riser basket by conducting the experiments at a high impeller speed of 5300 rpm.

Catalytic propane ODH runs were studied under an oxygen-free atmosphere using the lattice oxygen of the vanadium oxide in the VO_x/ γ Al₂O₃ and VO_x/ZrO₂- γ Al₂O₃ catalysts. To achieve this, multi-injection experiments were considered. Multi-injection experiments were used to change the catalyst state from completely oxidized to partially reduced. In each set of experiments, the identifiable carbon-containing products other than propylene were, CO, CH₄, CO₂, C₂H₄ and C₂H₆.

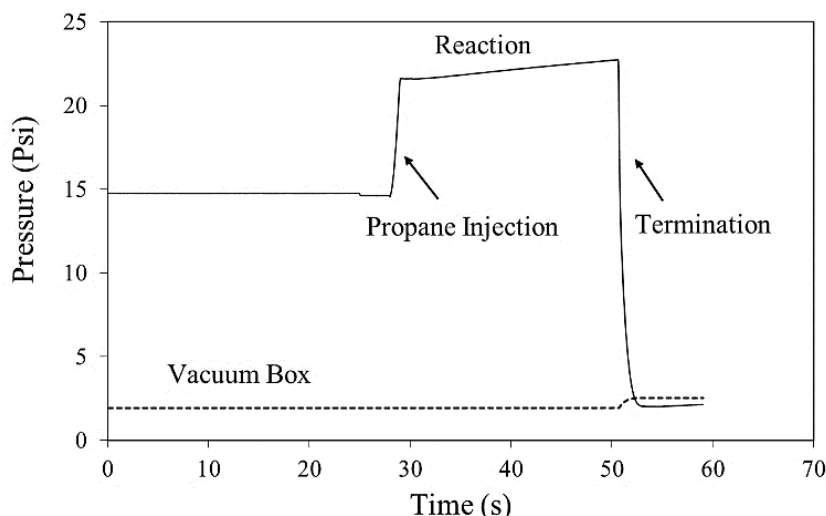


Figure 22: Pressure Profile in the CREC Riser Simulator for a Propane ODH Reaction.

Typical pressure profiles during propane ODH reactions in the CREC Riser Simulator are reported in Figure 22. The upper curve displays an increase in total pressure from injection (pulse) time to the termination time. This pressure rise is assigned to the increase in the total number of moles during the PODH reaction, involving propane and the lattice oxygen. Furthermore, the lower curve reports the pressure profile in the vacuum box, which remained constant during the reaction period. At the end of the experiment, and due to the gaseous products being transferred from the reactor to the vacuum box, the reactor pressure abruptly decreased while the pressure slightly augments in the vacuum box. As a result, reaction products were transferred almost instantaneously from the reactor to the vacuum box at 150°C preventing any further reaction. Once the product evacuation was completed, a sample of the gases contained in the vacuum box was transferred to a GC unit for analysis.

5.3.1 Thermal Runs

Blank runs or thermal runs (without catalyst) were performed to determine the contribution of homogeneous dehydrogenation gas-phase reactions. This allowed one to understand the difference between catalytic oxidative dehydrogenation effects and the thermal conversion effects. These runs were performed at the same reaction conditions (at 550°C and 20 s) as in a typical run. It can be seen in Table 10 that propane conversion remained at low levels ($\approx 4.0\%$). Based on these results, and under the conditions studied, thermal cracking was considered negligible.

Table 10: Propane Conversions and Product Selectivities during Thermal Runs.

Selectivity (%)				C ₃ H ₈ Conv. (%)	C ₃ H ₆ Yield (%)
CH ₄	C ₂ H ₄	C ₂ H ₆	C ₃ H ₆		
7.49	13.28	0.40	78.00	4.00	3.12

(Operating conditions for thermal runs: T=550°C, reaction time=20 s, C₃H₈ injected= 10 ml). Reported data correspond to at least 3 repeats. Standard deviations for repeats: 2%

5.3.2 Consecutive Propane Injections in PODH Experiments

In these PODH experiments, the VO_x/γAl₂O₃ and VO_x/ZrO₂-γAl₂O₃ catalysts were progressively reduced via 10 consecutive propane injections. The PODH catalyst was regenerated after the 10-consecutive injection. Both propane conversion, as well various product were calculated for each individual injection run.

Operating conditions selected were consistent with a proposed industrial process as described in Figure 3: a) reaction time: 20 s; b) Temperature: 550°C; c) Amount of Catalyst: 0.76 g and d) Propane Injected: 10 ml. Furthermore, the degree of reduction of the catalysts and their selectivities for PODH were determined by analyzing various product chemical species. Each experiment was repeated three times to ensure reproducibility. Carbon balances included unconverted propane and carbon-containing product species. It was found to be in all cases higher than 95%.

Regarding, the first series of runs, 2.5, 5 and 7.5 wt. %V/γAl₂O₃ catalysts were prepared and tested in the CREC Riser Simulator for propane ODH.

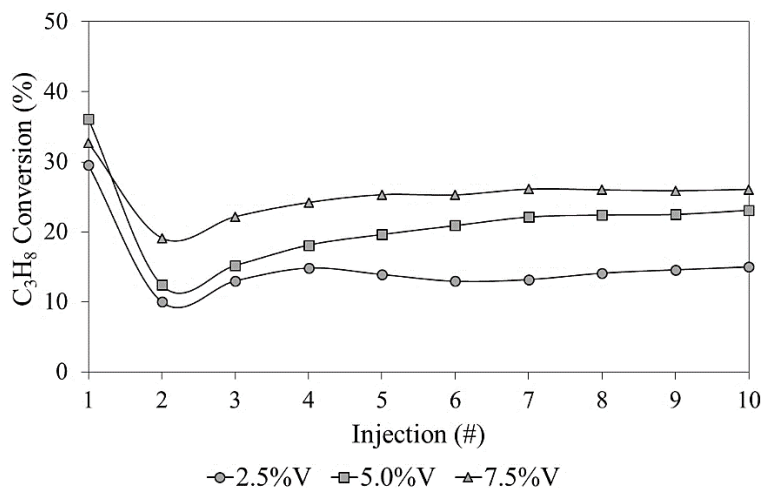


Figure 23: Propane Conversions during consecutive ODH Cycles over Various $\text{VO}_x/\gamma\text{Al}_2\text{O}_3$ Catalysts.

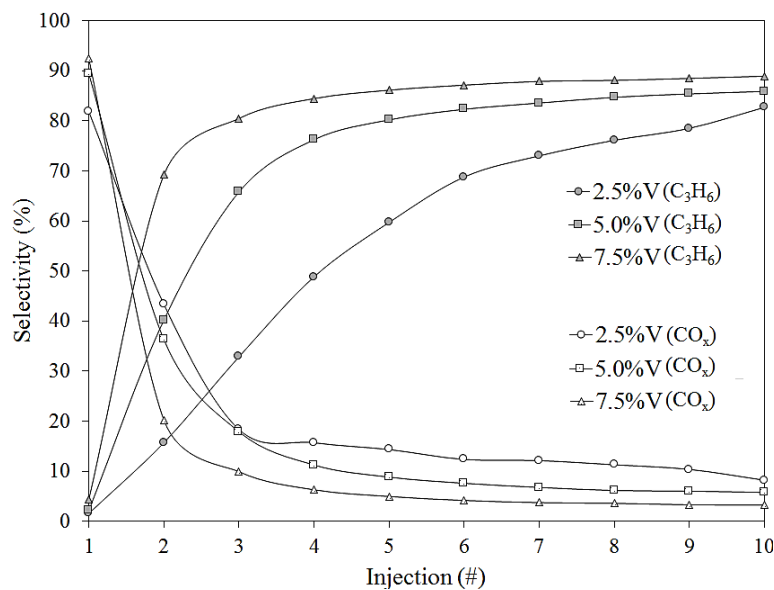


Figure 24: Propylene and CO_x Selectivities during consecutive ODH injections using various $\text{VO}_x/\gamma\text{Al}_2\text{O}_3$ Catalysts.

For Figure 23 and Figure 24, the operating conditions chosen were: a) $T=550^\circ\text{C}$; b) reaction time=20 s; c) C_3H_8 injected= 10 ml and d) catalyst loaded=0.76 g. Reported data correspond to at least 3 repeats. Standard deviations for repeats: 2%. Note that reported values are based on propane conversion into carbon containing gas phase products.

Figure 23 and Figure 24 report propane conversions as well as propylene and CO_x selectivities for the three prepared vanadium over γ -Al₂O₃ catalysts. Regarding the role of oxygen in PODH, experimental runs were planned using consecutive propane injections in oxygen free atmosphere. This allowed showing that under free oxygen atmospheres, there is variable oxygen reactivity using the PODH catalyst. For instance, during the 1st injection, PODH is strongly influenced by labile oxygen. Essentially all propane during the first injection is converted to carbon oxides, yielding the lowest propylene selectivity. Furthermore, during the 2nd injection, the remaining labile oxygen still plays a role. This is the case given that, a good fraction of propane is combusted to CO_x, with this CO_x inhibiting the PODH reaction and limiting the overall propane conversion to propylene¹¹⁴. Furthermore, once the labile oxygen consumed, the PODH reaction can proceed in earnest, as observed during the 3rd and subsequent injections, with both propane conversion and propylene selectivity increasing progressively. In summary, this significant change in selectivity shows that a certain degree of catalyst reduction is needed in order to obtain the best propylene selectivity.

Table 11 compares propylene and various product selectivities for the 10th consecutive injection for the three PODH catalyst studied (2.5, 5 and 7.5 wt. %V/ γ -Al₂O₃). Operating conditions: T=550°C, reaction time=20 s, C₃H₈ injected= 10 ml, catalyst loaded=0.76 g. Catalyst is not re-oxidized in between propane injections. Reported data correspond to at least 3 repeats. Standard deviations for repeats: 2%. Note that, reported values are based on propane conversion into gas phase carbon containing products.

Table 11: Performance of the VO_x/ γ -Al₂O₃ catalysts after 10 consecutive cycles.

Catalysts	Selectivity (%)						C ₃ H ₈ Conv.	C ₃ H ₆ Yield
	CO	CH ₄	CO ₂	C ₂ H ₄	C ₂ H ₆	C ₃ H ₆	(%)	(%)
2.5%V/ γ -Al ₂ O ₃	6.7	5.0	1.6	2.0	2.1	82.7	17.3	14.3
5%V/ γ -Al ₂ O ₃	3.6	4.0	0.9	1.7	1.4	88.5	25.6	22.6
7.5%V/ γ -Al ₂ O ₃	3.0	3.6	0.7	1.7	1.7	89.3	25.7	22.9

One can observe from Table 11, that through the 10 consecutive cycles, propylene selectivities increased progressively with the 7.5%V/ γ -Al₂O₃ catalyst reaching a 25.7% best propane conversion

and a 89.3% selectivity. This showed that high propylene selectivity can be achieved with minimum CO_x and cracking product selectivities.

However, and to further increase the propylene selectivity, three more catalysts were prepared with a modified $\gamma\text{Al}_2\text{O}_3$ support using ZrO_2 . Once again, vanadium loadings were 2.5%, 5% and 7.5%. Figure 25 and Figure 26 report both propane conversion and propylene and CO_x selectivities for the $\text{VO}_x/\text{ZrO}_2-\gamma\text{Al}_2\text{O}_3$ catalysts using 10 consecutive propane injections without oxygen addition in-between injections.

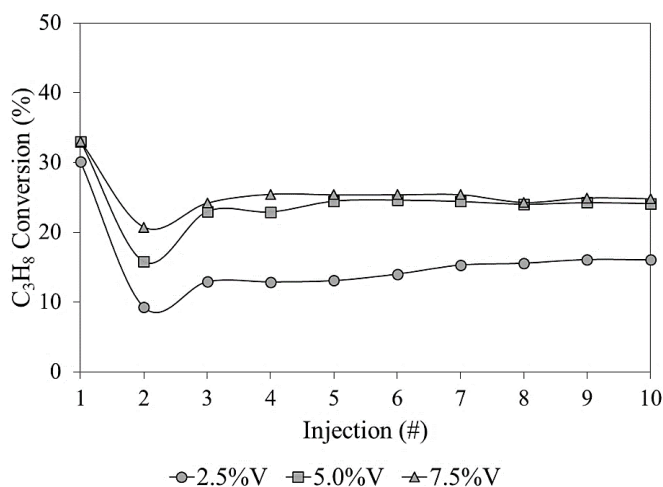


Figure 25: Propane Conversion during Consecutive ODH Cycles over $\text{VO}_x/\text{ZrO}_2-\gamma\text{Al}_2\text{O}_3$ Catalysts.

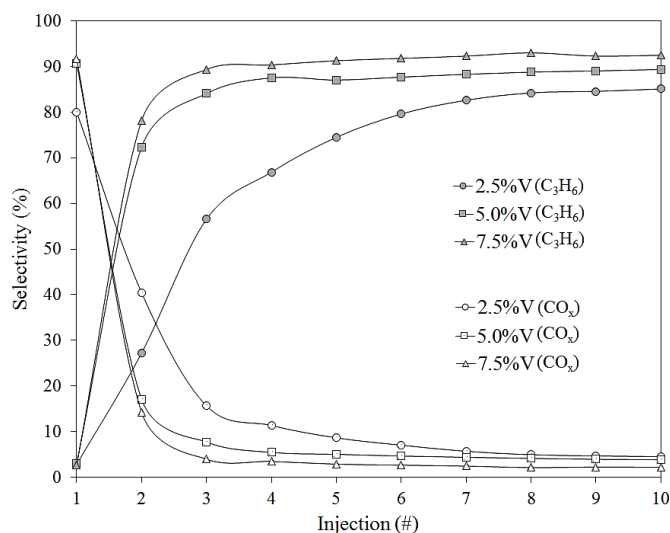


Figure 26: Propylene and CO_x Selectivities during Consecutive ODH Cycles using $\text{VO}_x/\text{ZrO}_2-\gamma\text{Al}_2\text{O}_3$ Catalysts.

Regarding Figure 25 and Figure 26, the following operating conditions were selected: a) $T=550^{\circ}\text{C}$; b) reaction time=20 s; c) C_3H_8 injected= 10 ml and d) catalyst loaded=0.76 g. Reported data correspond to at least 3 repeats. Standard deviations for repeats: 1.5%. Note that, reported values are based on propane conversion into carbon containing gas phase products.

As can be observed in Figure 25 and Figure 26, the $\text{VO}_x/\text{ZrO}_2-\gamma\text{Al}_2\text{O}_3$ catalysts provide a similar trend in terms of propane conversion and propylene and CO_x selectivities as the $\text{VO}_x/\gamma\text{Al}_2\text{O}_3$ catalysts. Propane conversion decreased with the number of injections as the propylene selectivity augmented steadily. For instance, for the 7.5% V loaded $\text{ZrO}_2-\gamma\text{Al}_2\text{O}_3$ supported catalyst, the propylene selectivity augmented steadily up to 92.5% (10th consecutive injection) while for the 2.5 and 5% V loaded $\text{ZrO}_2-\gamma\text{Al}_2\text{O}_3$ supported catalysts, it increased up to 85.1% and 89.7% respectively. These propylene selectivity values superseded the ones for $\text{VO}_x/\gamma\text{Al}_2\text{O}_3$ catalysts, with propane conversion being, however, very close.

Table 12 reports propane conversion and product selectivities for the 10th consecutive injection for various $\text{VO}_x/\text{ZrO}_2-\gamma\text{Al}_2\text{O}_3$ catalysts. Here, one can notice a progressive increase of both propane conversion and propylene selectivity with vanadium loading, with a very favorable propylene selectivity of 93% achieved for the 7.5% V/ $\text{ZrO}_2-\gamma\text{Al}_2\text{O}_3$ catalyst. One should also notice that this was accomplished with a significant reduction of the CO_x species. For example, in the case of 7.5% V/ $\text{ZrO}_2-\gamma\text{Al}_2\text{O}_3$, this remained below 2.1%. This was in clear contrast with the 3.7% CO_x selectivity obtained for the 7.5% V/ $\gamma\text{Al}_2\text{O}_3$ catalyst.

Table 12: Performance of Various $\text{VO}_x/\text{ZrO}_2-\gamma\text{Al}_2\text{O}_3$ Catalysts after the 10th Consecutive Cycle.

Catalysts	Selectivity (%)						C_3H_8 Conv. (%)	C_3H_6 Yield (%)
	CO	CH_4	CO_2	C_2H_4	C_2H_6	C_3H_6		
2.5% V/ $\text{ZrO}_2-\gamma\text{Al}_2\text{O}_3$	3.8	5.5	0.7	2.1	2.8	85.1	16.0	13.7
5% V/ $\text{ZrO}_2-\gamma\text{Al}_2\text{O}_3$	3.0	3.1	1.1	1.8	1.2	89.7	25.1	22.5
7.5% V/ $\text{ZrO}_2-\gamma\text{Al}_2\text{O}_3$	1.6	2.5	0.4	1.7	1.1	92.5	24.8	22.9

For Table 12, the operating conditions were: a) $T=550^{\circ}\text{C}$; b) reaction time=20 s; c) C_3H_8 injected= 10 ml and d) catalyst loaded=0.76 g. One should notice that in this case, catalyst is not re-oxidized

in between propane injections. Reported data correspond to at least 3 repeats. Standard deviations for repeats: 1.5%. Note that, reported values are based on propane conversion into gas phase carbon containing products.

The $\gamma\text{Al}_2\text{O}_3$ is an acidic support. Vanadia dispersed on $\gamma\text{Al}_2\text{O}_3$ yield polyvanadates which promote complete propane oxidation. Thus, 7.5%V/ $\gamma\text{Al}_2\text{O}_3$ has an intrinsically limited propylene selective. On the other hand, $\text{ZrO}_2\text{-}\gamma\text{Al}_2\text{O}_3$ provides a less acidic-support. Vanadia on $\text{ZrO}_2\text{-}\gamma\text{Al}_2\text{O}_3$ promote, isolated tetrahedral VO_x species which are more prone to enhance propylene selectivity.

Table 13 reports an average coke-on-catalyst on a per injection basis for the 7.5%V/ $\gamma\text{Al}_2\text{O}_3$ and 7.5%V/ $\text{ZrO}_2\text{-}\gamma\text{Al}_2\text{O}_3$ catalysts. Carbon contents were calculated using Total Organic Carbon Analyzer.

Table 13: Carbon Content Analysis on a per Injection Basis for the 7.5% V/ $\gamma\text{Al}_2\text{O}_3$ and 7.5% V/ $\text{ZrO}_2\text{-}\gamma\text{Al}_2\text{O}_3$ Catalysts. Reported coke values represent average values.

Catalysts	$g_{\text{coke}}/g_{\text{catalyst}}$	$g_{\text{coke}}/g_{\text{propane}}$
7.5%V/ $\gamma\text{Al}_2\text{O}_3$	0.0010	0.04
7.5%V/ $\text{ZrO}_2\text{-}\gamma\text{Al}_2\text{O}_3$	0.0006	0.02

One can observe from Table 13 that, the 7.5%V/ $\text{ZrO}_2\text{-}\gamma\text{Al}_2\text{O}_3$ produces almost half the coke than the 7.5 %V/ $\gamma\text{Al}_2\text{O}_3$. These lower coke yields in the 7.5%V/ $\text{ZrO}_2\text{-}\gamma\text{Al}_2\text{O}_3$ can also be linked to the lower acidity of the 7.5%V/ $\text{ZrO}_2\text{-}\gamma\text{Al}_2\text{O}_3$ catalyst limiting propane cracking. Taking 0.76g of catalyst and 10 ml propane injection, this yields a 0.04 g of coke/g of propane and 0.02 g of coke/g of propane for the 7.5 %V/ $\gamma\text{Al}_2\text{O}_3$ and 7.5%V/ $\text{ZrO}_2\text{-}\gamma\text{Al}_2\text{O}_3$ catalyst respectively.

As a result, both propylene selectivity and propane conversion are revised accounting for coke as follows:

$$\text{Propane Conversion, } X_{\text{C}_3\text{H}_8}(\%) = \frac{\sum_i v_i n_i}{3n_{\text{propane}} + \sum_i v_i n_i + n_{\text{coke}}} \times 100 \quad (40)$$

$$\text{Selectivity to Propylene, } S_{\text{C}_3\text{H}_6}(\%) = \frac{v_i n_i}{\sum_i v_i n_i + n_{\text{coke}}} \times 100 \quad (41)$$

This yields 85% propylene selectivity and 28% propane conversion for the 7.5% V/ZrO₂-γAl₂O₃ catalyst.

Thus, the 7.5 wt.% vanadium loading on a ZrO₂ modified γAl₂O₃ support, yields a PODH catalyst with high propylene selectivity. This is accomplished using a catalyst not requiring re-oxidation during 10 consecutive PODH cycles. This makes of the 7.5% V/ZrO₂-γAl₂O₃, a suitable catalyst for a continuous PODH process which uses a manageable catalyst inventory.

Given the above described findings, the 7.5% V/ZrO₂-γAl₂O₃ catalyst was further analyzed at different temperatures and contact times. One should note that in this case, catalyst/propane weight ratio was kept as before (44 g/g) having a 0.40 g of catalyst loaded and using 5 ml of propane for every ODH cycle.

Figure 27 and Figure 28 report propane conversions as well as propylene and CO_x selectivities for 10 successive propane injections. There was no catalyst regeneration between the 10 consecutive propane injections. The described runs were developed using the 7.5V/ZrO₂-γAl₂O₃ catalyst, 20 s reaction time and 500°C, 525° C and 550°C reaction temperatures. Catalyst loaded= 0.40 g and propane injected= 5 ml. Reported data correspond to at least three repeats. Standard deviations for repeats: 1.2%. Note that the reported values are based on propane conversion to gas phase carbon-containing product species.

It can be observed that during the first propane injection, while propane conversion is significant, CO_x selectivity and propylene selectivity remain high and low, respectively¹⁰. This is assigned to the fact that the first of the 10 consecutive PODH injections is strongly influenced by very reactive and weakly adsorbed oxygen, favoring complete propane combustion to CO_x. However, when this weakly bounded oxygen is depleted, CO_x selectivities start decreasing and propylene selectivities start increasing¹⁰.

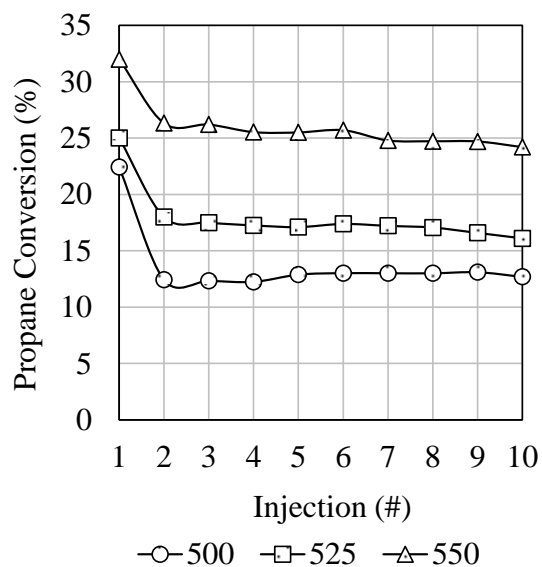


Figure 27: Propane Conversion during 10 Consecutive PODH Cycles using a 7.5V/ZrO₂-γAl₂O₃ Catalyst at T=500, 525 and 550°C and Reaction Time= 20 sec.

Thus, it is under the 4th to the 10th PODH consecutive propane injections, that the highest propylene selectivities for PODH are obtained, as reported in Figure 28. Thus, injections 1-3 were not considered in this kinetic analysis given these injections led to products somewhat more affected by the PODH catalyst labile oxygen. One can notice as well, that during these 4th to the 10th PODH consecutive propane injections, both propane conversion as well as CO_x selectivities remain almost constant. Thus, the 7.5V/ZrO₂-γAl₂O₃ catalyst can deliver dosed lattice oxygen up to 10 cycles, with this leading to an almost constant high selectivity. One shall note however that, after these 10 consecutive cycles, the catalyst must be regenerated to resupply it with oxygen.

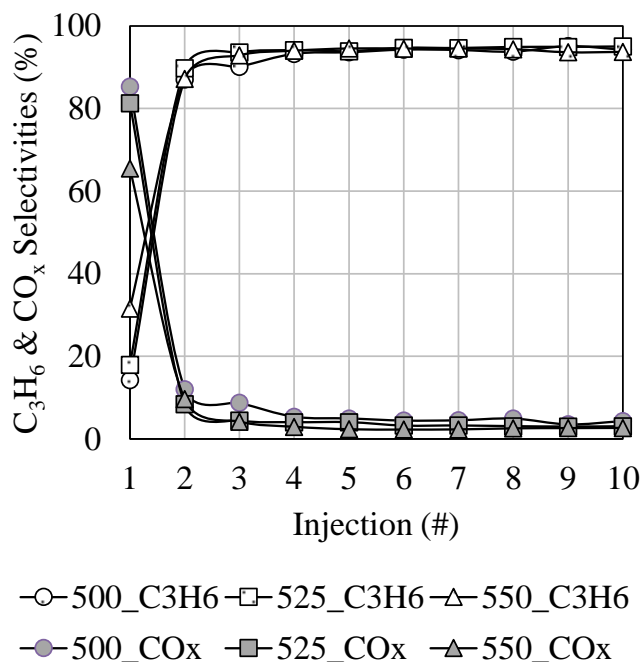


Figure 28: Propylene and CO_x Selectivities during 10 Consecutive PODH Cycles using a 7.5V/ZrO₂-γAl₂O₃ Catalyst at T=500, 525 and 550°C and Reaction Time= 20 sec.

Figure 29, Figure 30 and Figure 31 report the average propane conversion, propylene selectivity and CO_x selectivity from the 4th-10th consecutive propane injections using the 7.5V/ZrO₂-γAl₂O₃ catalyst at 10, 15 and 20s and 500°C, 525°C and 550°C.

These data show that, increasing temperature and reaction time, augment propane conversion from 8% to 25%, enhancing propylene selectivity from 91 to 94% and decreasing CO_x selectivity from 6.7 to 2.5% (Appendix B: Conversion and Products Distribution Results). Thus, propylene selectivity increases at higher temperatures in the 500°C-550°C range, with this being attributed to the higher lattice oxygen mobility¹⁴⁹. As well, longer contact times yield higher catalyst lattice oxygen utilization, favoring propylene formation and decreasing CO_x.

One should also notice, that the only identifiable carbon-containing products other than propylene were CO, CO₂, CH₄, C₂H₄ and C₂H₆. However, CH₄, C₂H₄ and C₂H₆ percentages yields were below 2% (Appendix B: Conversion and Products Distribution Results). Therefore, these chemical species can be neglected in the kinetics analysis. Besides, thermal cracking in the worst-case scenario in terms of thermal cracking contribution (highest temperature: 550°C and longest

reaction time: 20 s), it was found to contribute up to 2% propane conversion only. Thus, thermal cracking was considered negligible in the kinetic modelling development.

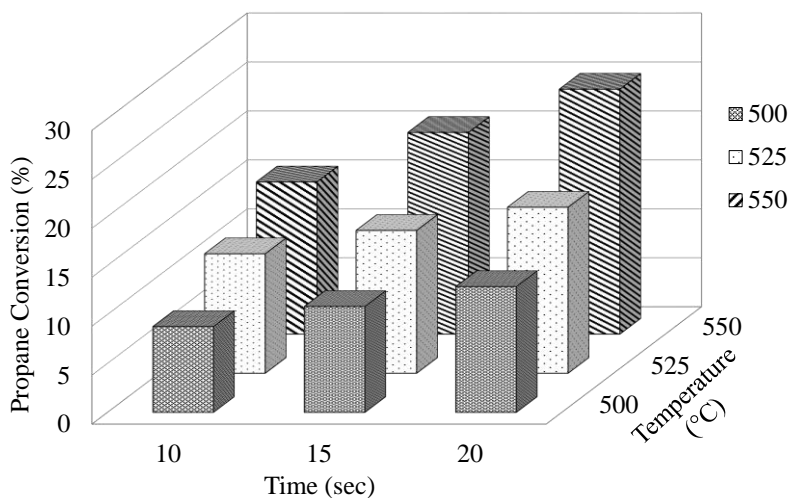


Figure 29: Propane Conversions Obtained with Different Reaction Times and Temperatures.

Reported data are the average of 4-10 injections.

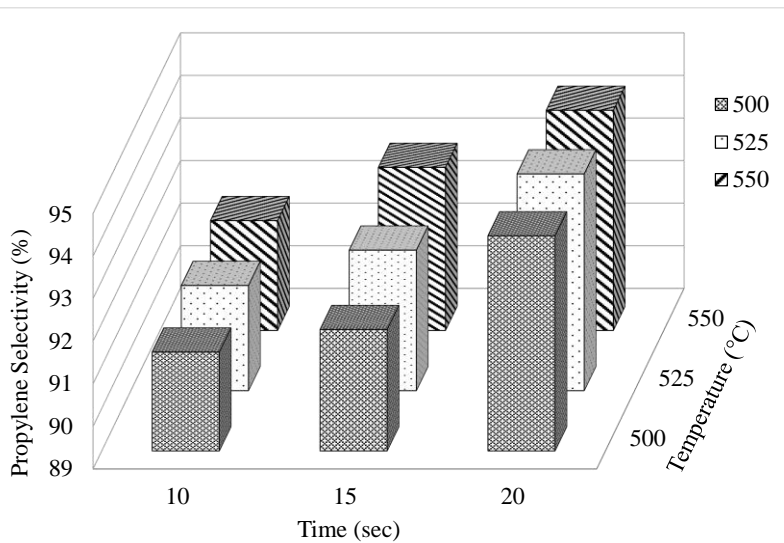


Figure 30: Propylene Selectivities Obtained with Different Reaction Times and

Temperatures. Reported data are the average of 4-10 injections.

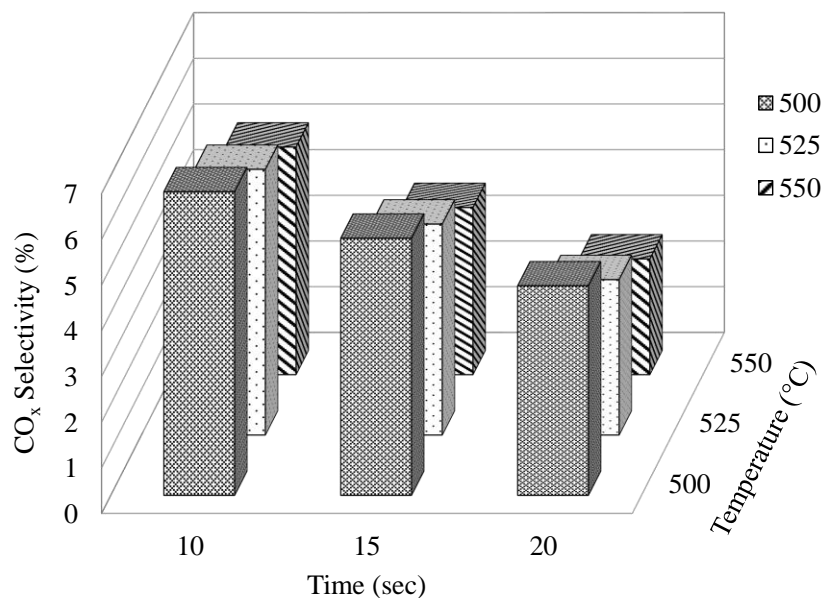


Figure 31: CO_x Selectivities Obtained with Different Reaction Times and Temperatures.

Reported data are the average of 4-10 injections.

In summary, PODH catalyst reduction with limited lattice oxygen availability, provides a favorable reaction pathway for propane combustion with CO_x formation. In this respect, added zirconia has a critical effect as well, reducing catalyst support acidity. This facilitates propylene desorption, minimizing the influence of the consecutive propylene oxidation reactions.

One should note however, that temperature increases are limited in practice. Temperature increases beyond 650°C are not recommended, as this would result in a significant decrease in propylene yield¹⁵⁰ due to the more significant influence of unselective thermal reactions.

5.4 Conclusions

- a) The ability of a VO_x loaded ZrO₂-γAl₂O₃ catalyst to perform in oxidative dehydrogenation of propane under oxygen-free atmospheres was demonstrated. Reported results favor the use of a twin fluidized continuous process, which complies with the desirable condition of limited catalyst inventory.
- b) XRD and Raman analyses were helpful to show that VO_x/ZrO₂-γAl₂O₃ catalysts did not show V₂O₅ crystals. On the other hand, XRD and Raman analyses of the 2.5% and 5%V/ZrO₂-

$\gamma\text{Al}_2\text{O}_3$ exhibited tetragonal zirconia peaks, while the 7.5% V on $\text{ZrO}_2\text{-}\gamma\text{Al}_2\text{O}_3$ showed a monoclinic zirconia phase.

- c) TPR and XPS were valuable to confirm that, there are two of vanadium achievable oxidation states on the catalyst surface: V^{+4} and V^{+5} . In the presence of hydrogen, V^{+5} is reduced to V^{+4} .
- d) $\text{NH}_3\text{-TPD}$ and pyridine-FTIR showed that the $\text{VO}_x/\gamma\text{Al}_2\text{O}_3$ (considered as a reference) was more acidic than $\text{VO}_x/\text{ZrO}_2\text{-}\gamma\text{Al}_2\text{O}_3$. In the $\text{VO}_x/\gamma\text{Al}_2\text{O}_3$ catalysts, Lewis acid sites are dominant, while in the $\text{VO}_x/\text{ZrO}_2\text{-}\gamma\text{Al}_2\text{O}_3$ catalysts, Brønsted acid sites become more abundant.
- e) TPD kinetics was important to show that the highest desorption energy was observed when using the 7.5% V/ $\text{ZrO}_2\text{-}\gamma\text{Al}_2\text{O}_3$ catalyst. This can be assigned to an increased vanadium-support interaction, which is predicted to favor a controlled PODH reaction.
- f) PODH runs showed that, propane can be selectively converted to propylene using a 7.5V/ $\text{ZrO}_2\text{-}\gamma\text{Al}_2\text{O}_3$ (1:1) catalyst in the absence of gas-phase oxygen. Good propane conversion levels (8-25%) and high propylene selectivity (91-94%) were achieved using 10 successive injections of propane in a CREC Riser Simulator in the 500-550°C range.
- g) Consecutive propane injection, with up to 10 propane injections allowed controlled catalyst reduction, achieving high propylene selectivity. Injections 4 to 10 were the ones with the highest and steadiest propylene selectivity, with coke amounts being negligible.
- h) Regarding the 7.5V/ $\text{ZrO}_2\text{-}\gamma\text{Al}_2\text{O}_3$ (1:1) catalyst lattice, it was replenished with oxygen following the 10th injection.

Chapter 6: Kinetic Modeling

Propane oxidative dehydrogenation involves a parallel-series reaction network^{100–105,151,152}. This reaction network can be considered to include: a) the PODH conversion to propylene, b) the undesired formation of CO_x from propane and c) the secondary combustion of propylene to CO_x. In these cases, the only source of oxygen is the catalyst lattice oxygen. These reactions can be described as follows:

Desired Reaction:



Undesired Reaction:



Equation (42) and (43) are “primary reactions”, while Equation (44) is a “secondary” reaction step. These three reactions steps are of critical importance for determining propylene selectivity. On this basis, a triangular parallel-series reaction network is proposed for the PODH (Figure 32).

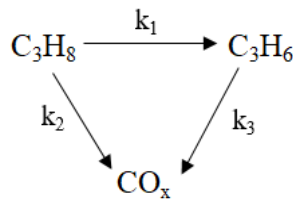


Figure 32: Proposed Reaction Network for Propane Oxidative Dehydrogenation using a VO_x/ZrO₂-γAl₂O₃ Catalyst in the CREC Riser Simulator.

The proposed reaction network assumes that propane reacts with the catalyst lattice oxygen producing both propylene and CO_x. The associated rate constants are k₁ with k₂, respectively. On the other hand, propylene can be further combusted to CO_x. The associated rate constant is k₃.

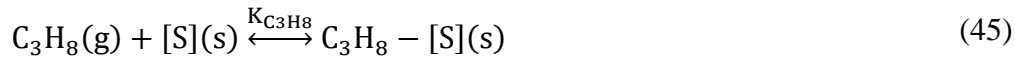
6.1 Kinetic Model Development

In absence of gas-phase oxygen propane ODH of the present study, it can be assumed that, there are two types of oxygen species available on the catalyst: (a) surface oxygen or weakly adsorbed oxygen and (b) lattice oxygen. Surface oxygen is responsible for the combustion of propane and propylene to produce CO_x whereas lattice oxygen provides a controlled release of oxygen which is necessary for high propylene formation. According to the Langmuir-Hinshelwood mechanism, propane, propylene and CO_x are adsorbed on the catalyst surface.

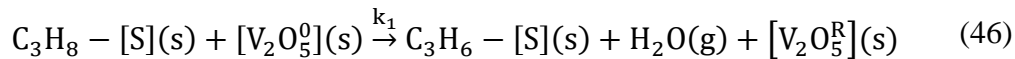
Thus, the surface reaction step is considered to be the rate controlling step and this while compared to the adsorption and the desorption steps. According to this mechanism, there are two types of catalyst sites: a) [V₂O₅⁰] representing the lattice oxygen in an oxidized site-1, b) [V₂O₅^R] denoting a surface oxygen vacancy in a reduced site-1 and c) [S] representing a support-based site-2.

Based on this, the following elementary steps can be considered:

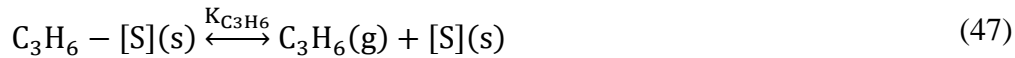
- i. Adsorption of propane on a support-based site-2 on the catalyst surface:



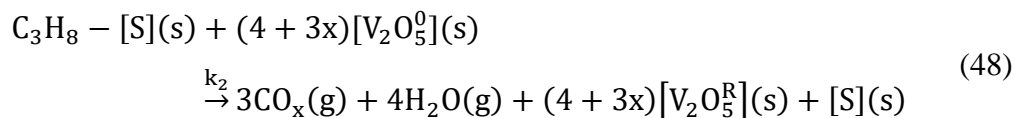
- ii. Formation of propylene (r₁) via the reaction between adsorbed propane and lattice oxygen of the [V₂O₅⁰] site:



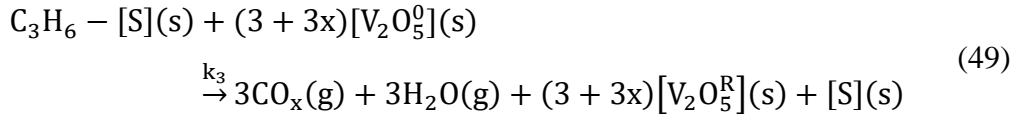
- iii. Propylene desorption from a reduced site :



- iv. CO_x formation from propane (r₂) via the reaction between adsorbed propane and lattice oxygen of the [V₂O₅⁰] site:



v. CO_x formation from propylene (r_3) via the reaction between adsorbed propylene and lattice oxygen of the $[\text{V}_2\text{O}_5^0]$ site:



vi. The re-oxidation of the reduced catalyst by molecular oxygen:



According to the above described reaction mechanism, rate equations for steps 1, 2 and 3 are:

$$r_1 = k_1\theta_{\text{C}_3\text{H}_8}(1 - \beta) \quad (51)$$

$$r_2 = k_2\theta_{\text{C}_3\text{H}_8}(1 - \beta) \quad (52)$$

$$r_3 = k_3\theta_{\text{C}_3\text{H}_6}(1 - \beta) \quad (53)$$

where, r_i is the reaction rate (mol/g_{cat}.sec), k_i is the reaction rate constant (mol/g_{cat}.sec), θ_i is the surface coverage of the adsorbed species “i”. In $\beta+\gamma=1$, β represents the reduced vanadium sites and $\gamma=1-\beta$ stands for the oxidized vanadium sites. $\theta_{\text{C}_3\text{H}_8} + \theta_{\text{C}_3\text{H}_6} + \theta_{\text{CO}_x} + \theta_v = 1$ describes the support-based sites.

Thus, the surface coverage θ_i is given by:

$$\theta_{\text{C}_3\text{H}_8} = \frac{K_{\text{C}_3\text{H}_8}C_{\text{C}_3\text{H}_8}}{1 + K_{\text{C}_3\text{H}_8}C_{\text{C}_3\text{H}_8} + K_{\text{C}_3\text{H}_6}C_{\text{C}_3\text{H}_6} + K_{\text{CO}_x}C_{\text{CO}_x}} \quad (54)$$

$$\theta_{\text{C}_3\text{H}_6} = \frac{K_{\text{C}_3\text{H}_6}C_{\text{C}_3\text{H}_6}}{1 + K_{\text{C}_3\text{H}_8}C_{\text{C}_3\text{H}_8} + K_{\text{C}_3\text{H}_6}C_{\text{C}_3\text{H}_6} + K_{\text{CO}_x}C_{\text{CO}_x}} \quad (55)$$

where, K_i is the adsorption constant (cm³/mol) of species “i” and C_i is the concentration (mol/cm³) of species “i”.

Given that the catalyst lattice oxygen is consumed by the PODH reactions, the available oxygen must be included in the kinetic model. This can be expressed using a time-dependent extent of

oxidation. This can be calculated using the ratio of oxygen content left over the original oxygen content of the catalyst before the PODH run. Therefore, the catalyst degree of oxidation is expected to decrease during the PODH reaction cycles.

Moreover, catalyst re-oxidation is a necessary process step after several reaction cycles (in this case after cycle 10) in order to the PODH catalyst recovers activity. Ten (10) consecutive injections were selected as the upper limit for the total number of injections in this study. After 10 injections, it was observed that propylene selectivity decreased with a higher abundance of cracking products. This can be justified given that under these conditions there is a lack of surface oxygen, with this negatively influencing product selectivity. As a result, catalyst regeneration was carried out in all cases after 10 cycles. This is a sound choice given in the continuous unit, this is equivalent to 1/10 of the total catalyst flow go to the regenerator as explained in a previous manuscript ⁵⁹.

Researchers reported that the use of an exponential decay function based on converted propane is suitable for the oxygen-free propane ODH ^{10,101,114}:

$$\varphi = \exp[-\lambda(X_{C_3H_8})] \quad (56)$$

where, φ is the catalyst's degree of oxidation, λ is a decay constant and X is the propane conversion. The advantage of this function is that it accounts for the effects of reaction conditions (temperature, concentration and contact time) on the catalyst extent of oxidation.

From Equations ((51)-(53)), β can be related to φ as:

$$(1 - \beta) = \varphi \quad (57)$$

Substitution of Equations ((54)-(57)) into ((51)-(53)) allows to describe reaction rates in terms of partial pressures of various species as follows:

$$r_1 = \frac{k_1 K_{C_3H_8} P_{C_3H_8}}{1 + K_{C_3H_8} P_{C_3H_8} + K_{C_3H_6} P_{C_3H_6} + K_{CO_x} P_{CO_x}} \exp[-\lambda(X_{C_3H_8})] \quad (58)$$

$$r_2 = \frac{k_2 K_{C_3H_8} P_{C_3H_8}}{1 + K_{C_3H_8} P_{C_3H_8} + K_{C_3H_6} P_{C_3H_6} + K_{CO_x} P_{CO_x}} \exp[-\lambda(X_{C_3H_8})] \quad (59)$$

$$r_3 = \frac{k_3 K_{C_3H_6} P_{C_3H_6}}{1 + K_{C_3H_8} P_{C_3H_8} + K_{C_3H_6} P_{C_3H_6} + K_{CO_x} P_{CO_x}} \exp[-\lambda(X_{C_3H_8})] \quad (60)$$

where, K_{CO_x} represents the lumped equilibrium adsorption constant for ($CO_x=CO+CO_2$) and k_2 and k_3 are the observed lumped reaction rate constants, which are defined as follows:

$$k_2 = k_2^{CO} + k_2^{CO_2} \quad (61)$$

$$k_3 = k_3^{CO} + k_3^{CO_2} \quad (62)$$

Furthermore, intraparticle diffusional resistances and external mass transfer resistances can be neglected for this study. Appendix C addresses and justify the negligible influence of internal and external catalyst particle mass transfer limitations. Hence, reaction rates can be described as direct functions of the gas-phase species concentrations or species partial pressures.

Concerning coke and its effects on PODH, it was found to be negligible (<0.01 wt. %). Thus, the potential effect of coke on catalyst deactivation was disregarded.

6.2 Kinetic Modeling in the CREC Riser Simulator

In this study, the PODH experimental runs are carried out in the CREC Riser Simulator. The CREC Riser Simulator is a well-mixed batch reactor. Thus, the reaction rate can be expressed as follows:

$$\eta \varphi r_i = \frac{V_R}{W_c} \frac{d\left(\frac{P_i}{RT}\right)}{dt} \quad (63)$$

where V_R is the reactor volume (cm^3), W_c is the catalyst weight (g), P_i is the partial pressure of species “i”, R is the universal gas constant ($cm^3 \text{ atm mol}^{-1} K^{-1}$), T is the reactor temperature (K) and t is the reaction time (sec). Assuming an effectiveness factor of $\eta=1$, the reaction rate equation is as follows:

$$\varphi r_i = \frac{V_R}{W_c} \frac{d\left(\frac{P_i}{RT}\right)}{dt} \quad (64)$$

So, the general rate of reaction for each chemical species is obtained as follows:

$$\frac{dP_i}{dt} = \frac{W_c RT}{V_R} r_i \phi \quad (65)$$

Therefore, by using Equations (58) to (60) and Equation (65), the following equations can be obtained for the rate of propane consumption:

$$\begin{aligned} \frac{dP_{C_3H_8}}{dt} &= -\frac{W_c RT}{V_R} (r_1 + r_2) \\ &= -\frac{W_c RT}{V_R} \frac{(k_1 + k_2) K_{C_3H_8} P_{C_3H_8}}{(1 + K_{C_3H_8} P_{C_3H_8} + K_{C_3H_6} P_{C_3H_6} + K_{CO_x} P_{CO_x})} \exp[-\lambda(X_{C_3H_8})] \end{aligned} \quad (66)$$

As well, the rate of propylene formation can be expressed as:

$$\begin{aligned} \frac{dP_{C_3H_6}}{dt} &= \frac{W_c RT}{V_R} (r_1 - r_3) \\ &= \frac{W_c RT}{V_R} \frac{(k_1 K_{C_3H_8} P_{C_3H_8} - k_3 K_{C_3H_6} P_{C_3H_6})}{(1 + K_{C_3H_8} P_{C_3H_8} + K_{C_3H_6} P_{C_3H_6} + K_{CO_x} P_{CO_x})} \exp[-\lambda(X_{C_3H_8})] \end{aligned} \quad (67)$$

Finally, the rate of CO_x formation can be considered as follows:

$$\begin{aligned} \frac{dP_{CO_x}}{dt} &= \frac{W_c RT}{V_R} (3r_2 + 3r_3) \\ &= \frac{3W_c RT}{V_R} \frac{(k_2 K_{C_3H_8} P_{C_3H_8} + k_3 K_{C_3H_6} P_{C_3H_6})}{(1 + K_{C_3H_8} P_{C_3H_8} + K_{C_3H_6} P_{C_3H_6} + K_{CO_x} P_{CO_x})} \exp[-\lambda(X_{C_3H_8})] \end{aligned} \quad (68)$$

Equations (66) to (68) can be solved simultaneously using a selected set of initial conditions as in the CREC Riser Simulator, which describe the various species (propane, propylene and carbon oxides) partial pressure changes with reaction time.

As well, and with the purpose of obtaining intrinsic kinetic parameters (activation energies and pre-exponential factors), the kinetic parameter k_i in Equations (66) to (68) vary with temperature, following an Arrhenius equation given by:

$$k_i = k_i^0 \exp \left[\frac{-E_i}{R} \left(\frac{1}{T} - \frac{1}{T_m} \right) \right] \quad (69)$$

where, k_i^0 is the intrinsic kinetic constant pre-exponential factor (mol/g_{cat}.sec), E_i is the activation energy (kJ/mol), R is the universal gas constant, T is the reaction temperature (K) and T_m is the median temperature (K).

The k_i constants were reparametrized to reduce the cross-correlation between the pre-exponential factors k_i^0 and the activation energies E_i ¹⁰⁶. This was done by centering the reaction temperature at a median value of $T_m=525^\circ\text{C}$. Substituting Equation (69) into Equations (66) to (68), gives a new set of ODEs with the k_i^0 , E_i and λ , being the intrinsic kinetic parameters to be estimated.

6.3 Estimation of Kinetic Parameters

The proposed rate expressions in Equations (66) to (68) are nonlinear with respect to their kinetic parameters. This is the result of Equations (66) to (68) having parameters that must be calculated both in the numerator and in the denominator. This is the case for the various species adsorption constants (K_i). One should note in this respect, that nonlinearity leads to over-parameterized models, with high parameter cross-correlations.

This issue is successfully addressed in the present study, by independently finding adsorption constants of various chemical species by using the CREC Riser Simulator ¹¹⁴. To accomplish this, independent adsorption experiments were evaluated in this reactor at different temperatures. Propane, propylene and carbon oxides adsorption isotherms were determined at 500, 525 and 550°C. Adsorption constants were determined by fitting the experimental data using a Langmuir adsorption isotherm (Equation (70)). An Arrhenius equation (Equation (71)) centered on the 525°C median temperature was employed to establish the effects of temperature. The adsorption constants and heat of adsorption for the various species are reported in Table 14 (details in Appendix D: Adsorption Constant Calculation).

$$\frac{V_i^A}{V_m} = \frac{K_i P_i}{1 + K_i P_i} \quad (70)$$

$$K_i = K_i^0 \exp \left[\frac{-\Delta H_i}{R} \left(\frac{1}{T} - \frac{1}{T_m} \right) \right] \quad (71)$$

where, V_i^A is the species volume adsorbed on the catalyst, V_m is the volume of monolayer coverage, K_i is the species adsorption constant (atm^{-1}), P_i is the species partial pressure (atm), K_i^0 is the adsorption constant pre-exponential factor (atm^{-1}) and $-\Delta H_i$ is the heat of adsorption (kJ/mol).

Table 14: Adsorption Parameters for Various Species.

Parameter	Estimated Value with 95% Confidence Spans	Parameter	Estimated Value with 95% Confidence Spans
$K_{\text{C}_3\text{H}_8}^0$ ^a	0.85 ± 0.02	$-\Delta H_{\text{C}_3\text{H}_8}$ ^b	32.2 ± 0.72
$K_{\text{C}_3\text{H}_6}^0$	0.43 ± 0.014	$-\Delta H_{\text{C}_3\text{H}_6}$	62.8 ± 1.20
$K_{\text{CO}_x}^0$	0.50 ± 0.018	$-\Delta H_{\text{CO}_x}$	54.0 ± 1.05

^a atm^{-1} ; ^b kJmol^{-1}

Furthermore, given the lack of kinetic parameter decay after injection 3, the λ decay parameter was set to zero. Therefore, the estimation of the 6 parameters (k_1^0 , k_2^0 , k_3^0 , E_1 , E_2 and E_3) was developed using non-linear least squares regression. The MATLAB routine “lsqnonlin” was used for the regression analysis. The numerical integration of the differential system (Equations (66) to (68)) and the determination of the 95% confidence intervals for each estimated parameter were performed using the MATLAB functions “ode45” and “nlparci”, respectively.

The optimization criteria was based on the fact that all the rate constants and all the activation energies for each reaction must be positive. Parameter estimates were obtained using a Trust Region Reflective Method for the minimization of the objective function:

$$SSQ = \sqrt{\sum_{i=1}^N (P_{i,\text{experimental}} - P_{i,\text{theoretical}})^2} \quad (72)$$

where, $P_{i,\text{experimental}}$ and $P_{i,\text{theoretical}}$ are the partial pressures of component “i” (propane, propylene and CO_x species) obtained experimentally and predicted by the kinetic model, respectively.

Model discrimination was based on the correlation coefficients (R^2) and the lowest sum of square (SSQ) criteria. The values of the 6 estimated parameters along with their corresponding 95% confidence intervals (CI) are reported in Table 15 for a 7.5V/ZrO₂- γ Al₂O₃ catalyst.

It can be noticed in Table 15, that all the estimated parameters display reduced and acceptable 95% confidence spans. Moreover, the ability to calculate the 6 model parameters is consistent with the high DOF (degrees of freedom) in this analysis. The DOF is 183 considering the 189 experimental data points including the 3 repeats per experimental condition.

Table 15: Intrinsic Kinetic Parameter Summary for the Proposed Kinetic Model with 95% Confidence Intervals (CIs).

Parameters	Value	95% CI	Correlation Matrix					
			k_1^0	k_2^0	k_3^0	E ₁	E ₂	E ₃
k_1^{0a}	2.82×10^{-5}	$\pm 1.15 \times 10^{-6}$	1					
k_2^0	1.65×10^{-6}	$\pm 1.02 \times 10^{-7}$	-0.84	1				
k_3^0	4.80×10^{-6}	$\pm 2.29 \times 10^{-6}$	0.83	-0.94	1			
E ₁ ^b	55.7	± 7.58	-0.21	0.04	-0.20	1		
E ₂	33.3	± 3.16	-0.03	0.07	0.13	-0.68	1	
E ₃	98.5	± 15.56	0.52	-0.55	0.75	-0.59	0.70	1
m	189							
DOF	183							

^a mol.gcat⁻¹s⁻¹; ^b kJmol⁻¹; Degree of freedom, DOF= Data points (m)- Parameters (p)=189-6=183.

Regarding the relative magnitudes of the activation energies as reported in Table 15, it can be noticed the following: a) PODH (Step1) is favored given the 2.82×10^{-5} mol.gcat⁻¹s⁻¹ frequency factor observed, a) CO_x from propane (Step 2) is limited, in spite of the 33.3 kJmol⁻¹ activation energy, as a result of the very low frequency factor, c) CO_x from propylene (Step 3) is very restricted given the 98.5 kJmol⁻¹ activation energy and 4.8×10^{-6} mol.gcat⁻¹s⁻¹ frequency factor.

These findings also support the data reported in Figure 29, Figure 30 and Figure 31. Zirconia modifies catalyst acidity, and as a result it can be hypothesized that propylene is not re-adsorbed significantly. This keeps the propylene selectivity high. Furthermore, the high value of the reaction

rate constant for propylene formation via propane oxidative dehydrogenation confirms that propylene formation dominates the reaction network.

Further insights into the validity of the proposed kinetic model and the estimated kinetic parameters could be obtained by comparing the product and reactant partial pressure model predictions with the experimental data. This comparison is reported in Figure 33. It can be noted that, within the limits of experimental error, the model predictions compare very well with the experimental data, validating the proposed PODH reaction model.

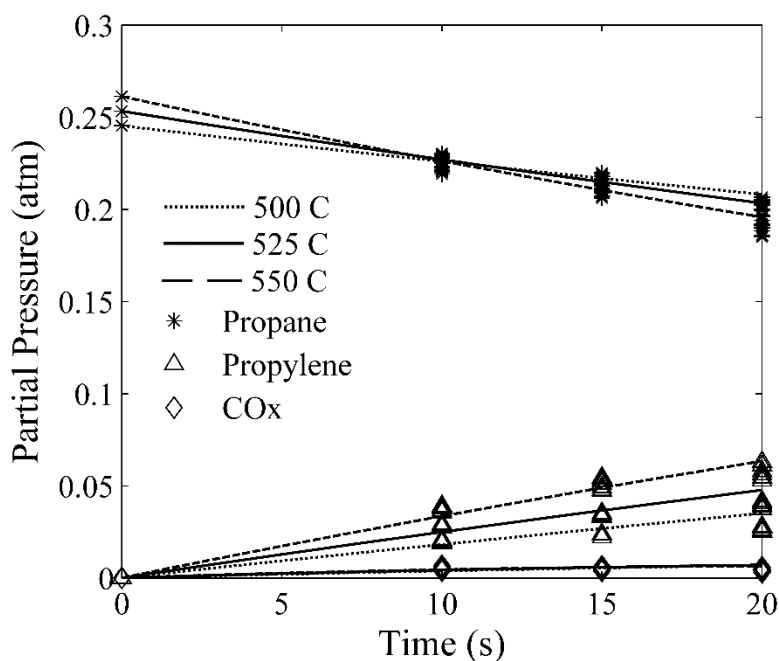


Figure 33: Comparison between Experimental Data and Model Predictions over a 7.5V/ZrO₂- γ Al₂O₃ Catalyst at T=500, 525 and 550°C.

Moreover, one can see in Figure 34 that, data is neither clustered in horizontal lines nor vertical lines. Horizontal lines may suggest observed conversion changes caused by an independent variable that is not included in the kinetic model. On the other hand, vertical lines may be an indication of the kinetic model over-parameterization.

Furthermore, the adequacy of the estimated parameters was confirmed by analyzing their interdependence through the cross-correlation matrix as shown in Table 15. It can be noticed that in most cases, cross-correlation coefficients are all below 0.90 with only one surpassing the 0.90

value. Therefore, it can be concluded that the proposed kinetic model is not over-parameterized and the defined parameters can be related to catalyst's physicochemical properties under this study.

Based on that which is discussed above, it can be determined that the established adsorption and kinetic parameters set in addition to the developed kinetic model are satisfactory to predict PODH reaction rates in the CREC Riser Simulator under the studied operating conditions range.

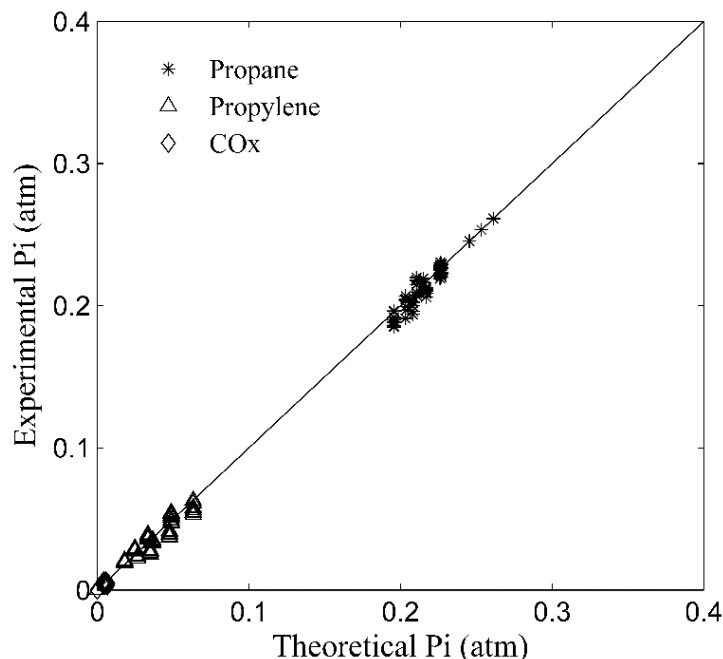


Figure 34: Overall Comparison between the Experimental Results and Model Predictions. Data points for three repeats are reported. Standard deviation on repeats is 1.5%.

As well, another important feature of the developed $7.5V/ZrO_2-\gamma Al_2O_3$ catalyst is limited coke formation (<0.01 wt. %). This justifies the observed λ decay parameter set as zero as reported here. This favorable property of the $7.5V/ZrO_2-\gamma Al_2O_3$ catalyst presents a significant advantage over other vanadium supported catalysts for PODH, referenced in the technical literature^{61,101}.

In brief, the catalytic experiments of the current study support a phenomenologically based kinetic model. This kinetic model can be of special value to support a PODH process using a twin circulating fluidized bed configuration (Figure 3). It is anticipated that, in this type of PODH process, with the selected operating conditions, after every 10 cycles, a small amount of catalyst will go back to regenerator and most of the catalyst will be recycled back directly to the PODH

reactor. It is expected that such an integrated PODH fluidized bed process will yield 25% propane conversion with 94% propylene selectivity.

6.4 Conclusions

- a) A parallel-series reaction network was proposed for the very stable PODH using a 7.5V/ZrO₂- γ Al₂O₃ (1:1) catalyst. This heterogeneous kinetic model was based on a Langmuir-Hinshelwood model. The rate equations were established by considering both reactant and product adsorption constants as well as catalytic reaction steps on the catalyst surface.
- b) The proposed kinetic model involved 6 independent kinetic parameters (k_1^0 , k_2^0 , k_3^0 , E_1 , E_2 and E_3). These 6 parameters were determined accurately using non-linear least squares regression and a large DOF. To accomplish this, the dominant propane, propylene and carbon oxides adsorption constants were determined independently in the CREC Riser Simulator and the λ activity decay parameter was set equal to zero. This led to parameters being calculated with reduced spans for the 95% confidence intervals and low parameter cross-correlation.
- c) The calculated energy of activation for propylene combustion were higher than that the ones for propane ODH and propane combustion. The frequency factors were as well much higher for PODH. This shows the intrinsic ability of a 7.5V/ZrO₂- γ Al₂O₃ (1:1) catalyst to promote high propylene selectivities (94%) at significant propane conversions (25%).

Chapter 7: CFPD Simulation of the PODH Process

7.1 Catalysts Used

The particle size distribution (PSD) of the 7.5 wt. % V/ZrO₂- γ Al₂O₃ catalyst considered in the present study, is reported in Figure 35. These spherical alumina particles show a mean particle diameter of 87.13 μ m with a standard deviation of 31.2 μ m, and an apparent particle density of 1730 kg/m³. Thus, the physical properties of this catalyst (apparent density, particle size) are very close to the ones used in previous studies by our research team^{153,154}.

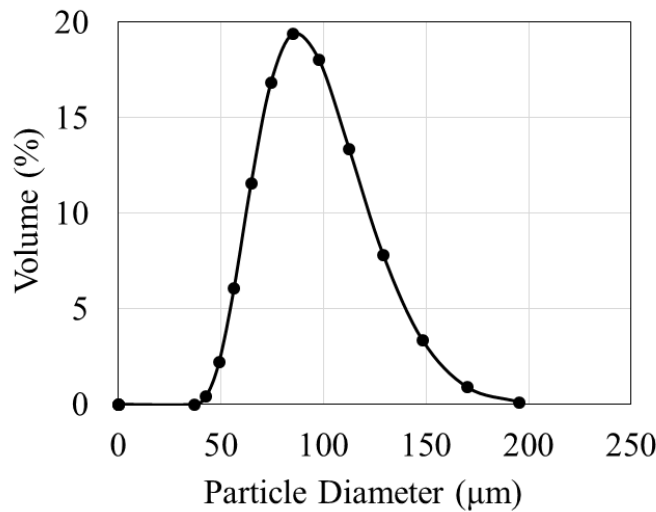


Figure 35: Volume Weighted Particle Size Distribution of PODH Catalyst Particles.

In downflow reactors particles flow as particle clusters. These particle clusters display a configuration of a train of particles, which is being a requirement for hydrodynamic stability¹²⁹. Furthermore, a PODH downer reactor model for adequate simulation requires a cluster particle size distribution. To provide this information, particle cluster data collected by our research team was adopted¹⁵⁴. These data allowed one to assume that particle clusters should involve an “asymmetric” particle cluster distribution as reported in Figure 36.

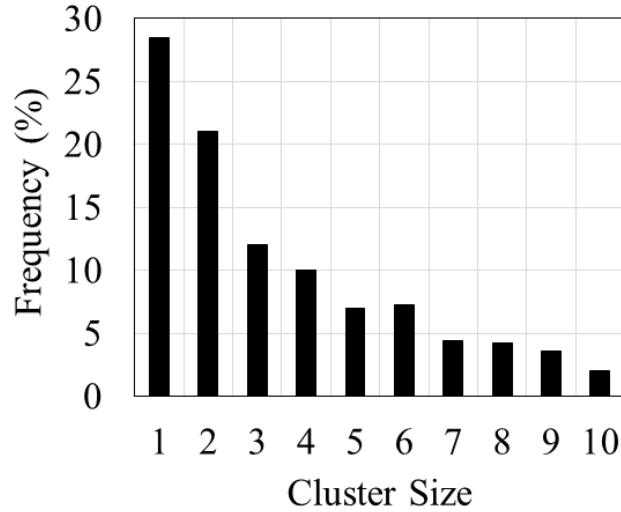


Figure 36: Distribution of the Number of Particles in Clusters for $U_g=1.5$ m/s, $G_s=34$ kg/m² s¹⁵⁴

7.2 Computational Particle Fluid Dynamic (CPFD) Modeling

7.2.1 CPFD Model Description

Gas-solid flows in CFB downers can be developed using a CPFD numerical scheme. To accomplish this, an accurate particle size distribution is needed. In this manuscript, both particle clusters and single particle size distributions are considered in the computations. Simulation conditions are selected so that calculated results show the value of accounting for particle clustering flow in PODH downer units.

In the present study, a Computational Particle Fluid Dynamic (CPFD) model is used to simulate the gas-solid flow with heat transfer and chemical reactions. Using the CPFD methodology, the gas and particle equations are solved in three dimensions. The gas phase dynamic is described by using the averaged Navier-Stokes equations (mass and momentum) with a strong coupling to the particle phase. Regarding the momentum equation, it is described by the Multi-phase Particle-in-Cell (MP-PIC) formulation^{155–158}. In the MP-PIC approach, not every particle and its interactions are calculated. This significantly reduces the computational cost. Therefore, the particles are grouped into computational particles with the same velocities and properties. This allows a reduction of the particle number from a magnitude of 10^{10} down to 10^5 - 10^6 .

Governing equations considered in the downer simulation are listed in Table 16. Using the MP-PIC method, temperatures within the particles and in the fluid surrounding the particles are assumed to be equal. This pseudo-homogenous model with negligible thermal gradients between particles and surrounding fluid, can be supported given the 53-120 micron particle size.

Table 16: Governing Equations for an Adapted CPFD Model Including the PODH Reaction.

Volume Averaged Gas Phase Model ^{159,160}

$$\text{Continuity equation: } \frac{\partial(\varepsilon_g \rho_g)}{\partial t} + \nabla \cdot (\varepsilon_g \rho_g \mathbf{u}_g) = \delta \dot{m}_p$$

$$\text{Momentum equation: } \frac{\partial(\varepsilon_g \rho_g \mathbf{u}_g)}{\partial t} + \nabla \cdot (\varepsilon_g \rho_g \mathbf{u}_g \mathbf{u}_g) = -\nabla p - \mathbf{F} + \varepsilon_g \rho_g \mathbf{g} + \nabla \cdot (\varepsilon_g \boldsymbol{\tau}_g)$$

$$\text{Energy equation }^{161}: \frac{\partial(\varepsilon_g \rho_g h_g)}{\partial t} + \nabla \cdot (\varepsilon_g \rho_g h_g \mathbf{u}_g) = \varepsilon_g \left(\frac{\partial p}{\partial t} + \mathbf{u}_g \cdot \nabla p \right) + \varphi - \nabla \cdot (\varepsilon_g \mathbf{q}) + \dot{Q} + S_h + \dot{q}_D$$

$$\text{Transport equation for the individual species: } \frac{\partial(\varepsilon_g \rho_g Y_{g,i})}{\partial t} + \nabla \cdot (\varepsilon_g \rho_g Y_{g,i} \mathbf{u}_g) = \nabla \cdot (\rho_g D \varepsilon_g \nabla Y_{g,i}) + \delta \dot{m}_{i,\text{chem}}$$

Particle Phase Model ¹⁵⁷

Transport conservation equation including a particle collision damping term:

$$\frac{df_p}{dt} + \frac{\partial(f_p \mathbf{u}_p)}{\partial x} + \frac{\partial(f_p A_p)}{\partial u_p} = \frac{f_D - f_p}{\tau_D},$$

Particle acceleration equation:

$$\mathbf{A}_p = \frac{d\mathbf{u}_p}{dt} = D_p(\mathbf{u}_g - \mathbf{u}_p) - \frac{1}{\rho_p} \nabla p_g - \frac{1}{\varepsilon_p \rho_p} \nabla \tau_p + \mathbf{g} + \frac{\overline{\mathbf{u}_p} - \mathbf{u}_p}{\tau_D}$$

Coupling Gas and Particle Phases

$$\text{Particle volume fraction in each cell: } \varepsilon_p = \iiint f_p \frac{m_p}{\rho_p} d\mathbf{u}_p dT_p$$

Rate of momentum transfer between fluid and solid phases:

$$\mathbf{F} = -\iiint f_p \left\{ m_p \left[D_p(\mathbf{u}_g - \mathbf{u}_p) - \frac{\nabla p}{\rho_p} \right] + \mathbf{u}_p \frac{dm_p}{dt} \right\} d\mathbf{u}_p dT_p$$

$$\text{Lumped Heat Equation for the Particle Phase }^{155}: C_V \frac{dT_p}{dt} = \frac{1}{m_p} \frac{\lambda_g N u_{g,p}}{2r_p} A_p (T_g - T_p)$$

Conservative Energy Exchange:

$$S_h = \iiint f_D \left\{ m_p \left[D_p (\mathbf{u}_p - \mathbf{u}_g)^2 - C_v \frac{dT_p}{dt} \right] - \frac{dm_p}{dt} \left[h_p + \frac{1}{2} (\mathbf{u}_p - \mathbf{u}_g)^2 \right] \right\} dm_p d\mathbf{u}_p dT_p$$

Reaction Kinetics: $k = A_0 m_p^{c_1} T^{c_2} \exp\left(\frac{-E}{RT} + E_0\right)$

Additional details of the basic governing equations for the gas and catalyst particles, their parameters and numerical procedures for solving the equations can be found in literature ^{155,156}.

7.2.2 Numerical Set-up and Simulation Conditions

For the CFPD simulations, an 8 cm diameter and 20 m height downer reactor, with two cyclones, one at the top and the other at the bottom of the downer were considered. Dimensions of the entry cyclone (feeding cyclone) ending in a venturi section, as shown in Figure 37 were selected to facilitate both gas and particle separation. This cyclone was designed following Stairmand's guidelines ¹⁶².

Furthermore, a cyclone dipleg ending in a spiral shaped section was selected to reduce particle velocity before particles enter into the downer. Dimensions of the exit cyclone as reported in Figure 38 (terminator cyclone) are identical to the ones of the entry cyclone.

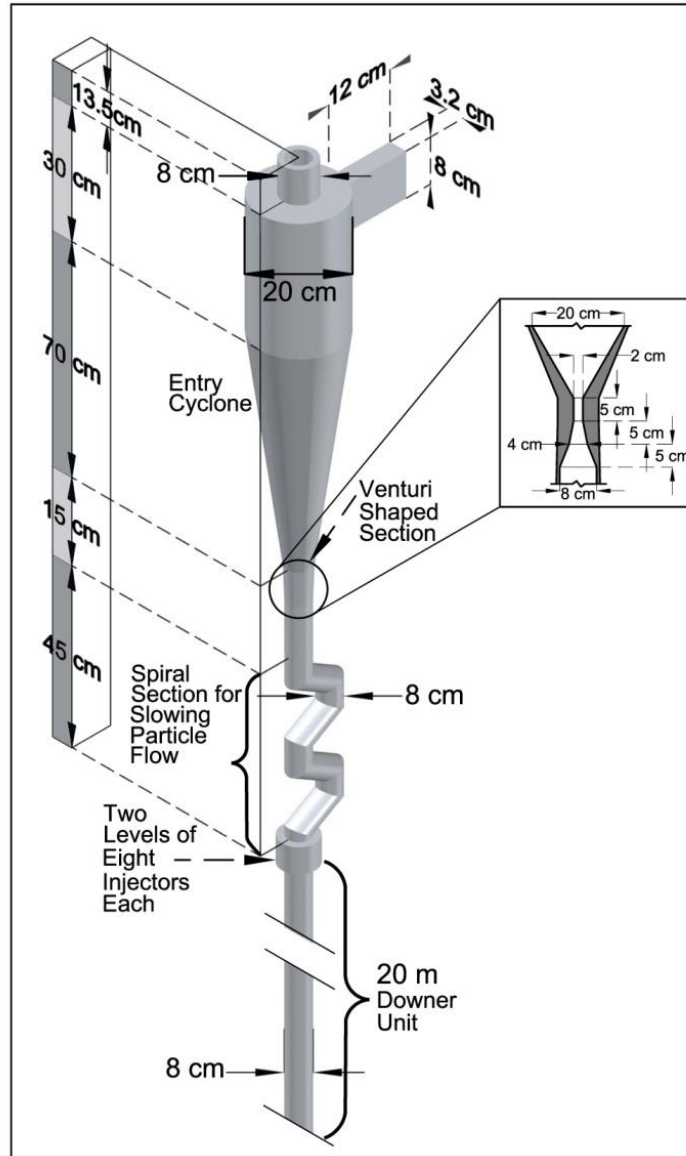


Figure 37: Schematic Dimensions of the Entry Cyclone (Feeding Cyclone) of the Downer Unit.

To initiate CPFDF computations, an empty particle free downer with two cyclones was filled with nitrogen at 1 atmosphere at a temperature of 550°C. Then, steam and catalyst particles were fed at the top entry cyclone continuously at a 3 m/s velocity. Catalyst particles were separated from steam in the entry cyclone, being fed to the downer. At the downer top section (solid flux in downer=28 kg/m².s), the flowing catalyst met with propane jets at two consecutive stages of propane injection as shown in Figure 38. At every injector stage, 8 propane jets emerged from 3.0 mm injector holes, angled downwards at 45 degrees. It was at this section, where catalyst and fluid mixed thoroughly.

Furthermore, the catalyst particles and the fluid emerging from the two stages of propane injection continued interacting with each other via drag forces. In this location, the propane and catalyst reacted as anticipated by the PODH kinetics⁶⁰. As well, at the downer outlet and after 20 s reaction time, solids, product gases and unconverted propane were fed to an exit cyclone (Terminator cyclone) where product gases and particles were separated and the PODH reaction was essentially arrested. Utilizing this downer, propylene can be produced 25 ton yearly.

The CPFDD Barracuda model was run using a personal computer comprising Intel® Core™ i7-3930K CPU @ 3.20 GHz processor, and RAM 16.0 GB. Windows 7, 64 bit operating system was employed to get an enhanced performance of simulation software. To reach a steady state, time computations had to be sufficiently long. For example, 30s or more of CPFDD Barracuda simulation time was considered adequate. Results obtained provided cluster particle velocity, solid concentration and slip velocity between the particle cluster and the superficial gas velocity. As well, computations allowed one to calculate local temperatures and product gases composition.

Regarding pressure boundary conditions, three pressure conditions as identified in Figure 38, were defined for the simulation at: 1) The top of the entry cyclone (Boundary Condition 1); 2) The top of the Terminator Cyclone (Boundary Condition 2) and 3) The bottom of the terminator cyclone dipleg (Boundary Condition 3).

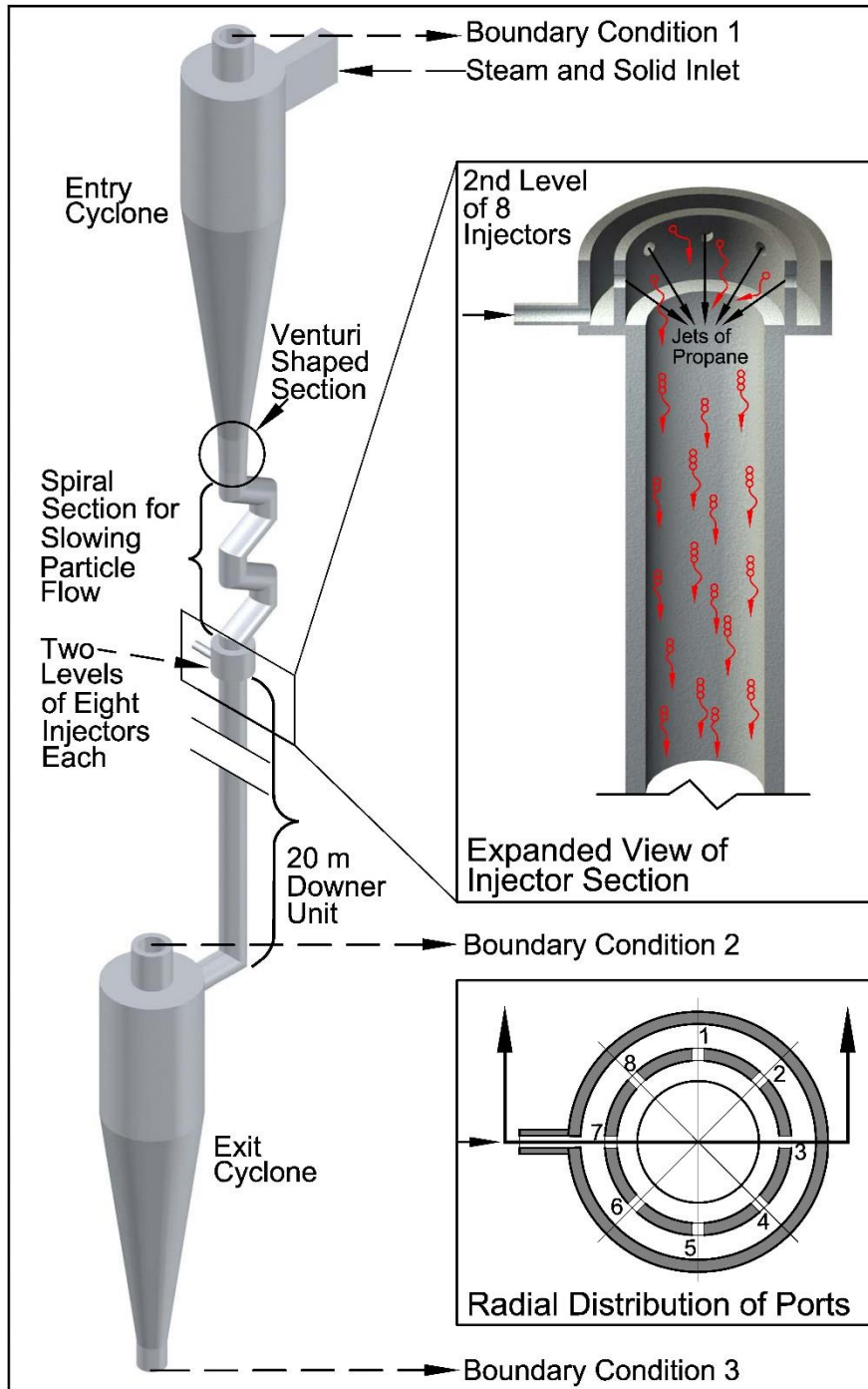


Figure 38: Schematic Diagram of Downer Unit Showing the Boundary Conditions for CPFD Calculations and the Propane Injector.

Furthermore, Table 17 reports additional details concerning various input parameters required for the CPFD simulations.

Table 17: Input Parameters in the CPFDF Simulation.

	Geometry	Simulation
CPFDF Model	Mesh	13×13×3250 for the downer
Heat transfer	Thermal flow	823 (K) (Starting temp.)
Gravity	z gravity	-9.8 (m/s ²)
Gases properties	Steam density	0.267 (kg/m ³)
	Steam molecular weight	18.02 (g/mol)
	Propane density	0.653 (kg/m ³)
	Propane molecular weight	44.1 (g/mol)
Particle properties	Density	1722 (kg/m ³)
	Sphericity	0.7 ¹⁵⁴
	Emissivity	1
Particle-to-particle interaction ¹⁶³	Close pack volume fraction	0.6
	Maximum momentum redirection from collision	40%
Particle-to-wall interaction	Normal-to-wall momentum retention	0.9
	Tangent-to-wall momentum retention	0.99 ¹⁶³
	Diffuse bounce	0
Initial conditions	Gas velocity	0
	Gas pressure	101325 (Pa)
	Solids	0
Pressure boundary conditions	Outlet pressure (1st cyclone top)	101325 (Pa)
	Outlet pressure (2nd cyclone top)	101325 (Pa)
	Outlet pressure (2nd cyclone bottom)	101325 (Pa)
Flow boundary conditions	Particle and steam velocity	3 (m/s)
	Particle/fluid slip ratio	1 ¹⁶⁴
	Particle feed per average volume	1500
	Particle feed mass flow rate	0.145 (kg/s)
Chemistry	Rate coefficient manager:	
	Reaction type	Volume-average

	Coefficient type Reactions manager: Reaction type	Arrhenius chemistry rate Stoichiometric
Time controls	Time step End time	0.01 (s) 40 (s)

7.2.3 Drag Model Used

Interactions between the gas and solid particles can be described using drag models. In CFPD, the modeling of gas-solid flows involves the selection of an adequate drag model. Drag models selected depend on particle sphericity. Thus, the Wen-Yu (for dilute flow, $\epsilon_g > 0.8$) model was used for single particle flows and the Ganser model was used for non-spherical clusters formed by trains of particles. Table 18 summarizes these recommended models.

Table 18: Drag Models Used in the CFPD Simulation.

Drag Model	where,
Force acting on a particle, $\mathbf{F}_p = m_p D(\mathbf{u}_g - \mathbf{u}_p)$	m_p =mass of the particle \mathbf{u}_g =fluid velocity \mathbf{u}_p =particle velocity D=drag function
Reynolds number, $Re = \frac{2\rho_g r_p \mathbf{u}_g - \mathbf{u}_p }{\mu_g}$	C_d =drag coefficient ρ_g =fluid density r_p =particle radius μ_g =fluid viscosity
Drag function, $D = \frac{3}{8} C_d \frac{\rho_g \mathbf{u}_g - \mathbf{u}_p }{\rho_p r_p}$	ϵ_g =fluid volume fraction
Wen-Yu's Model for Single Spherical Particles 165,166 $C_d = \frac{24}{Re} \epsilon_g^{n_0} (c_0 + c_1 Re^{n_1}); 0.5 \leq Re \leq 1000$	Wen-Yu's Model parameters: $c_0=1.0$; $c_1=0.15$; $c_2=0.44$; $n_0=-2.65$; $n_1=0.687$

<p>Ganser's Model for Non-Spherical Particle Clusters¹⁶⁷</p> $C_d = \varepsilon_g^{n_0} K_2 \left[\frac{24}{\text{Re} K_1 K_2} (1 + c_0 (\text{Re} K_1 K_2)^{n_1}) + \frac{24 c_1}{1 + \frac{c_2}{\text{Re} K_1 K_2}} \right]$ $K_1 = \frac{3}{1 + 2\psi^{-0.5}}; K_2 = 10^{n_2(-\log\psi)^{n_3}}$	<p>Non-Spherical Ganser's Model parameters: $c_0=0.1118$; $c_1=0.01794$; $c_2=3305$; $n_0=-2.65$; $n_1=0.6567$; $n_2=1.8148$; $n_3=0.5743$; ψ=particle sphericity</p>
--	---

7.2.4 Chemical Reactions

Table 19 reports the triangular PODH network implemented in the CFPD Barracuda code for the PODH downer reactor.

Table 19: Reactions, Kinetic Parameters and Thermodynamics Properties for the PODH Considered in the Present Calculations.

Propane ODH Reaction	$C_3H_8 + V_2O_5 \xrightarrow{k_1} C_3H_6 + V_2O_4 + H_2O$; $\Delta H_{800K} = 13.52 \text{ KJ/mol}$ (73)
Propane Combustion Reaction	$C_3H_8 + 8.5V_2O_5 \xrightarrow{k_2} 1.5CO + 1.5CO_2 + 8.5V_2O_4 + 4H_2O$; $\Delta H_{800K} = -505.14 \text{ KJ/mol}$ (74)
Propylene Combustion Reaction	$C_3H_6 + 7.5V_2O_5 \xrightarrow{k_3} 1.5CO + 1.5CO_2 + 7.5V_2O_4 + 3H_2O$; $\Delta H_{800K} = -518.66 \text{ KJ/mol}$ (75)

Where, $k_i = k_i^0 \exp\left[-\frac{E_i}{R} \left(\frac{1}{T} - \frac{1}{T_m}\right)\right]$ and k_i^0 represent the intrinsic pre-exponential factor (mol/gcat.sec); E_i stands for the activation energy (kJ/mol), R denotes the universal gas constant, T is the reaction temperature (K) and T_m represents the median temperature (K).

7.3 Results and Discussion

7.3.1 Mesh and Discrete Time Selection and Model Validation

The first step in the CFPD computations was to establish the influence of the selected mesh as well as that of the chosen incremental simulation time on the results obtained. It was observed that a downer grid mesh with 0.615 cm axial and radial increments was adequate. This led to: 13×13 steps in the cross-section plane $\times 3250$ axial steps or 549,250 cells in total. The incremental time

chosen was 0.01s. This matter is addressed in Appendix E: Grid Discretization Analysis, where it is shown that 1.5 times more cells and half of the incremental time (0.005 s) gave essentially the same simulation results with deviations less than 0.1%.

7.3.2 Entry and Exit Cyclones in the Downer Model

The proposed Hybrid CPFD model for PODH allows one to describe the changes of particle cluster velocity and gas velocity as well as the particle cluster volume fraction along the downer unit. Figure 39 (A) and Figure 39 (B) report these changes for both a downer simulation without cyclones, as well as for a downer equipped with both entry and exit cyclones.

Figure 39 (A) shows both axial gas velocity and axial particle cluster velocity for a downer without cyclones. One can observe that at the top of the downer unit, velocities are essentially zero. However, and due to particle cluster acceleration and propane injection, particle cluster and fluid velocity significantly increase in the top downer section (first 2 meters), reaching a fully developed flow pattern with particle cluster velocities remaining at 2.8-3.5 m/s and fluid velocity at 1.3-1.7 m/s ranges.

Figure 39 (B) reports axial gas and particle cluster velocity for a downer with entry and exit cyclones. One can then notice that particle clusters and gases emerging from the entry cyclone dipleg display 1.5 m/s and 0.65 m/s velocities, respectively. Furthermore, and once propane is fed via the two level of injectors, the axial gas velocity and axial particle velocity increase suddenly, with this change also being promoted by gravity acceleration. However, and because of the exit cyclone upstream effect, particle cluster and gas velocities abruptly decrease at the downer bottom.

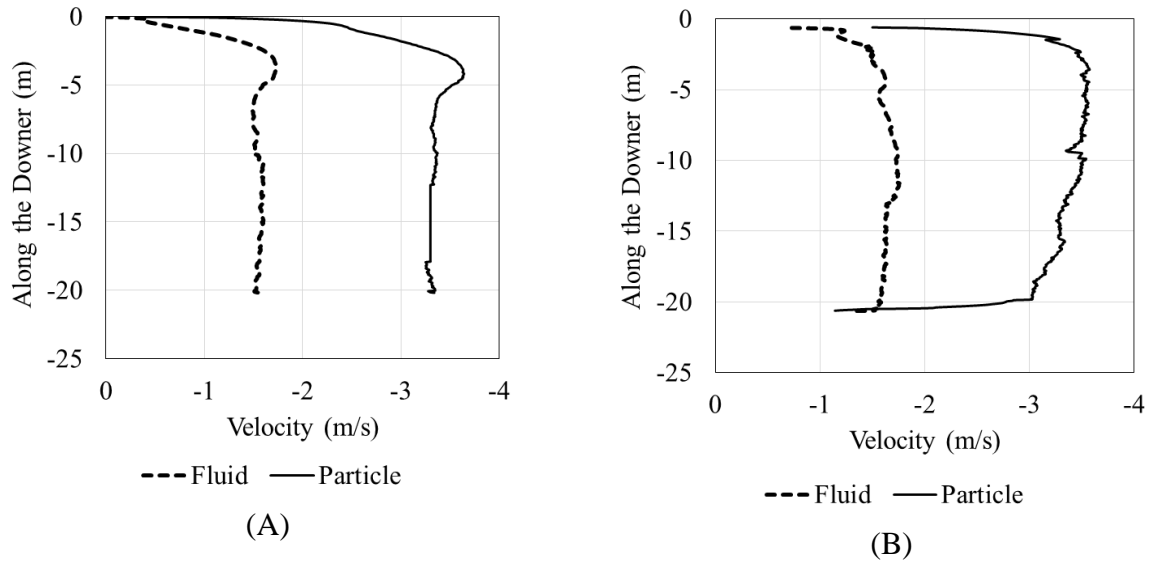


Figure 39: Axial Fluid and Particle Cluster Velocities along the Downer Length; (A) Downer unit only and (B) Downer unit Equipped with Feeding and Terminator cyclones.

Figure 40 shows the particle cluster volume fraction along the axial length of a downer unit with and without cyclones. In a downer without cyclones, one can notice a sudden reduction of the volume fraction in the entry downer region to a 0.006 volume fraction. This particle cluster volume fraction continues essentially unchanged, until it reaches the unit exit. However, for a downer with feeding and terminator cyclones, the particle cluster volume fraction decreases considerably in entry region, reaching 0.005, with a sudden increase in the near exit downer section of close to 0.01.

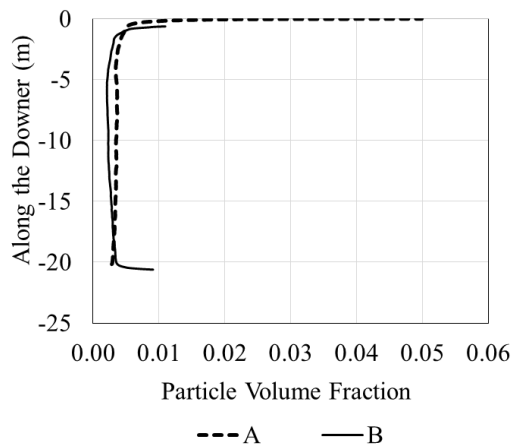


Figure 40: Average Axial Particle Cluster Volume Fraction along the Downer. (A) Downer unit only and (B) Downer equipped with entry and exit cyclones.

Figure 41 describes the axial pressure for both a downer unit only and a downer unit with entry and exit cyclones. As anticipated by ¹⁶⁸, the axial pressure profile displays an almost positive linear gradient in most of the downer, with the entry and the exit region being the exceptions.

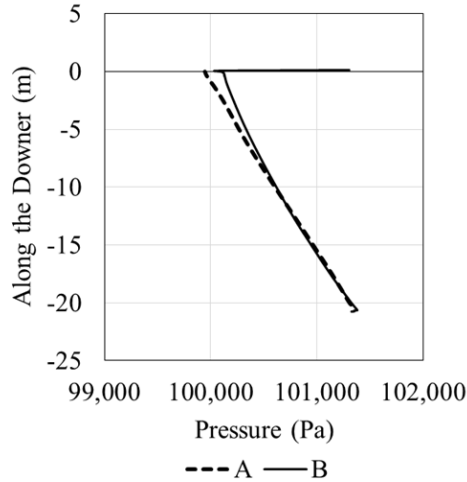


Figure 41: Simulated Average Pressure Profile along the Downer for a Particle Cluster Flow. (A) Downer unit only and (B) Downer equipped with entry and exit cyclones.

Furthermore, and consistent with this, Figure 42 shows a negative pressure gradient along the downer, with the entry and exit sections deviating from this trend.

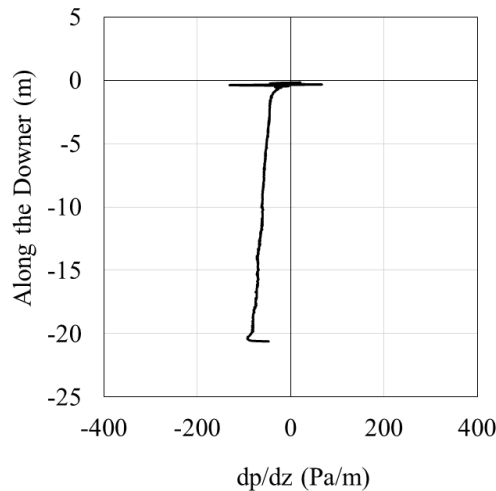


Figure 42: Average Pressure Gradient Profile along the Downer with Entry and Exit Cyclones.

As one can thus see, the inclusion of both the feeding cyclone and the terminator cyclone in the PODH downer simulation is important indeed. This is the case given that, it is in these sections

where the particle cluster volumetric concentration increases, and fluid velocity is significantly reduced. Given that both parameters have an impact on propane total conversion, it can be anticipated that the inclusion of the feeding and terminator cyclone regions in the CPFD simulations, contributes to enhancing propane total conversion by 2-3%.

Thus, and as a result, one can conclude that a rigorous downer model should incorporate the feeding and the terminator cyclones. This is significant to determining the true contribution of the entire downer system for propane conversion. The efficiency of the entry and exit cyclones based on gas and particle separation are reported in Appendix F: Gas and Particle Cluster Flow in Entry and Exit Cyclones.

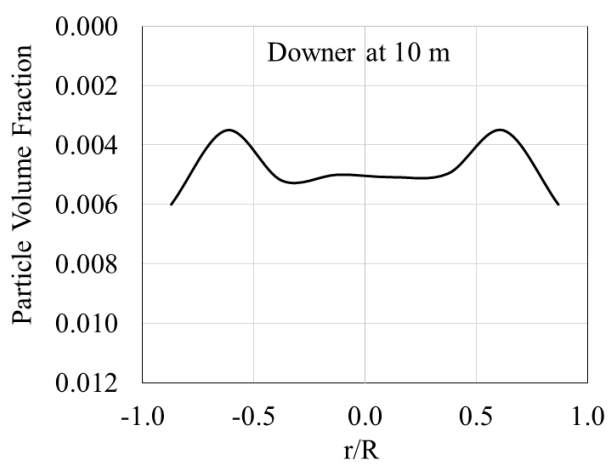
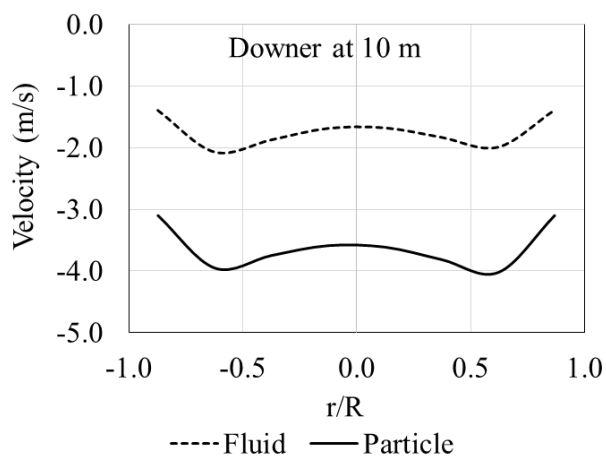
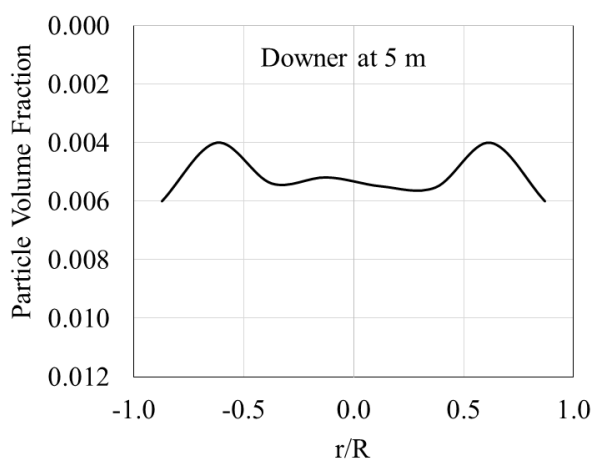
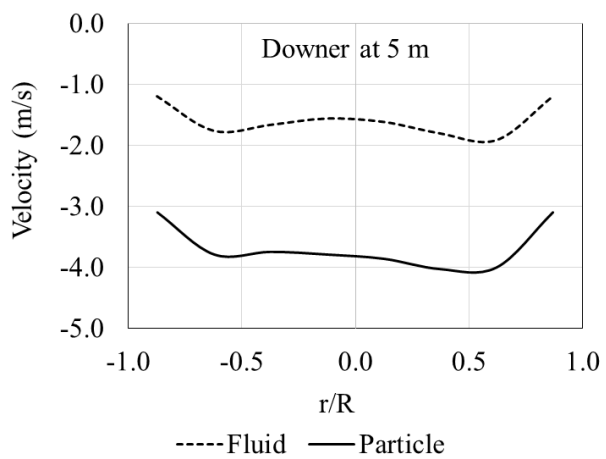
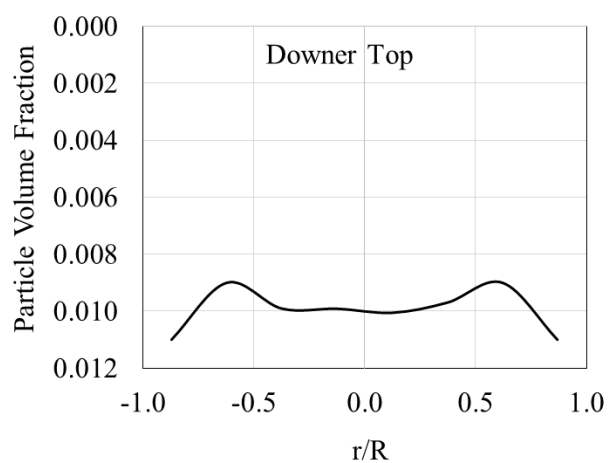
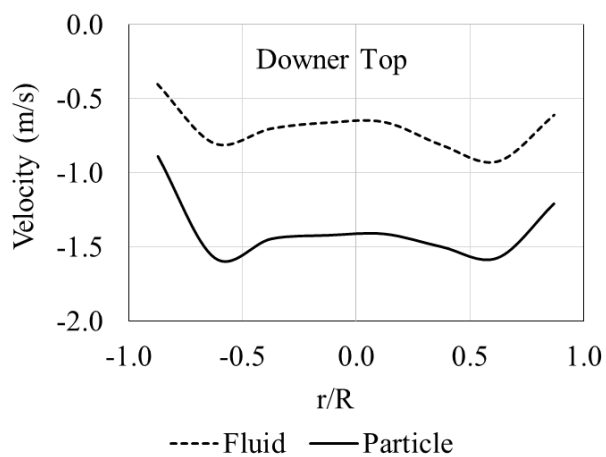
7.3.3 Radial Velocity and Solid Concentration Profiles in Downer with Entry and Exit Cyclones

7.3.3.1 Velocity Profiles

Figure 43 (a) reports the simulated radial gas and particle cluster velocities along the downer. One can observe at various z positions, consistently shaped gas and particle cluster radial velocity distributions with: a) stable velocities at the downer core, b) velocities changing in the near wall region. Additionally, one can also notice that, both gas and particle cluster velocities display consistency of the above described radial distribution at various axial positions, with cluster particle velocities in the core increasing from 1.4 m/s to 3.8 m/s. This axial velocity change is significantly moderated once the downer flow is fully established.

Regarding slip velocities between gas and particles, the calculated values are in the 2 m/s range. This is expected given the solid suspension model adopted, which includes a train of particles model for flowing clusters in the downer.

Finally, and at the downer near end section, it can be observed that both gas and particles at various radial positions, experience velocity reductions, with this being due to the exit cyclone influence on the two-phase flow.



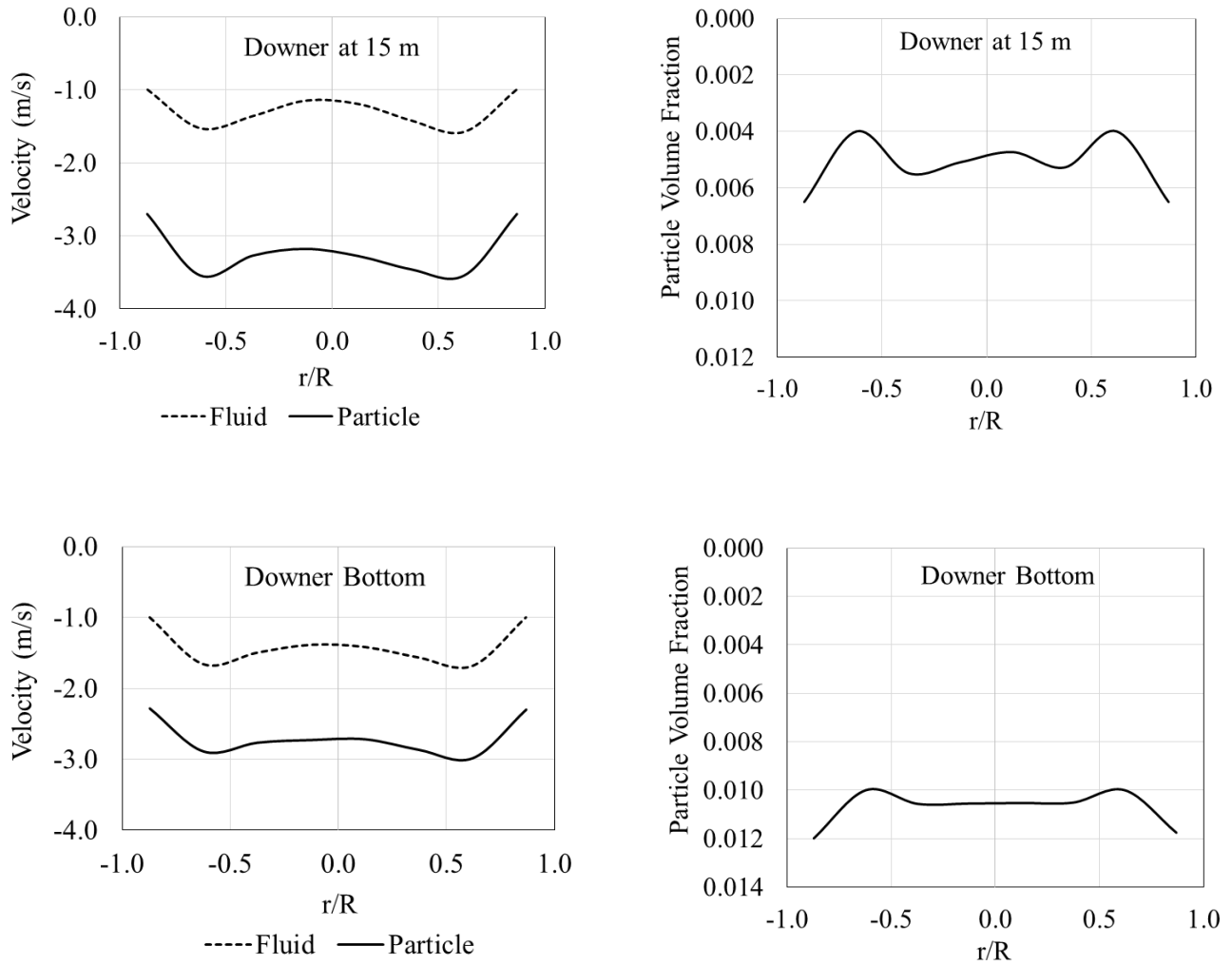


Figure 43: (a) Radial Velocity Profile for Both Gas and Particle Clusters and (b) Radial Particle Volume Fraction Profile for Particle Clusters.

7.3.3.2 Solid Concentration Profiles

Figure 43 (b) reports the radial solids distribution in the downer. One can notice a relatively constant solids holdup along the downer, with an annular region near the walls as well as in the downer core, with higher solid concentrations in the 0.005-0.006 range. These findings are consistent with higher solids concentrations in the wall region reported by ^{125,168}.

Particles in the downer tend to flow with a relatively constant solid flux. Thus, lower cluster particle velocities in the near-wall regions are combined with higher cluster particle hold ups. As

well, as one can anticipate, particle velocities decrease with increased particle cluster concentrations reaching 0.0010-0012 values, near the downer top section and near the bottom of the downer.

7.3.4 Particle Cluster and Gas Flows and PODH in a Downer Reactor

Figure 44 shows a propane mass flowrate along the downer top and bottom at various simulation times. Thus, one can see that at least 30s of simulation time are required for an accurate steady state propane conversion. Once this simulation time is reached, using Equation 76, a 20% propane conversion is observed.

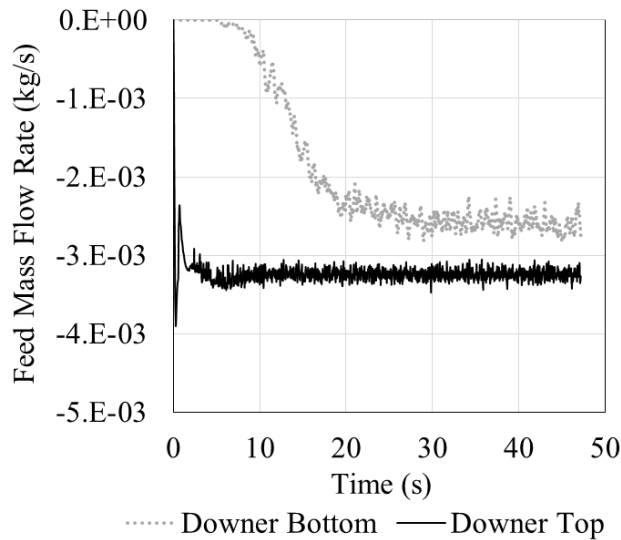


Figure 44: Propane Mass Flowrates through a Downer Bottom at Various Simulation Times.

Propane Conversion

$$\begin{aligned}
 &= \frac{\text{Mass Flowrate of Propane In} - \text{Mass Flowrate of Propane Out}}{\text{Mass Flowrate of Propane In}} \times 100 \quad (76) \\
 &= \frac{3.25 \times 10^{-3} - 2.60 \times 10^{-3}}{3.25 \times 10^{-3}} \times 100 = 20\%
 \end{aligned}$$

Figure 45 reports propylene and carbon oxide molar flowrates at the top and at the bottom of the downer reactor at various simulation times. Thus, one can also see that, for steady state propylene molar flowrates and steady state CO_x molar flowrates, simulation times larger than 30s are needed. This allows using the data in Figure 45 and Equation 77 to predict propylene selectivity in the 94% range.

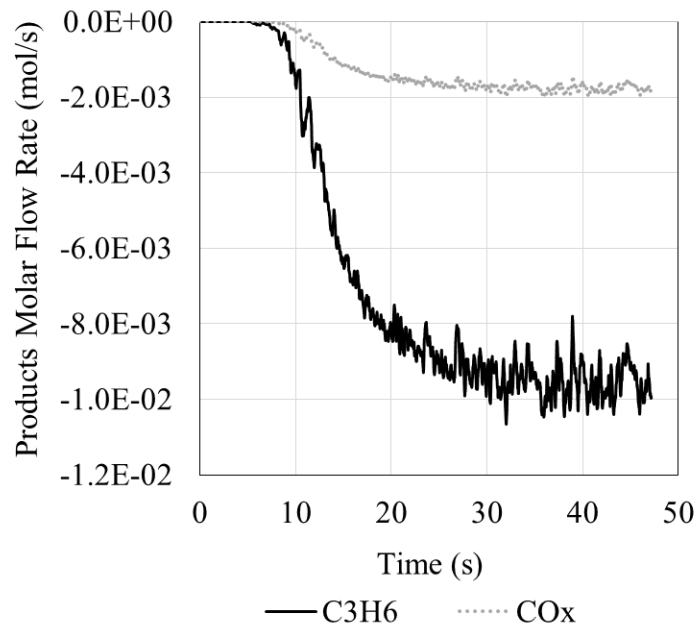


Figure 45: Products Molar Flowrates at the Downer Bottom at Various Simulation Times.

$$\text{Propylene Selectivity} = \frac{3 \times n_{\text{C}_3\text{H}_6}}{3 \times n_{\text{C}_3\text{H}_6} + n_{\text{CO}} + n_{\text{CO}_2}} \times 100 \dots (77)$$

$$= \frac{3 \times 9.56 \times 10^{-3}}{3 \times 9.56 \times 10^{-3} + 8.96 \times 10^{-4} + 8.82 \times 10^{-4}} \times 100 = 94.14\%$$

Figure 46 shows the molar fractions of various chemical species in the downer bottom along the downer length, and these molar fractions were calculated with simulation times in excess to 30s. This shows that, at the entry downer section, specifically at the injector section, steam (free of propane) meets propane. Following this, propane reacts with the catalyst particles with increasing reaction time. Because of this, propane molar fraction decreases from 0.8 to 0.58 and propylene increases progressively from 0 to 0.12 molar fractions.

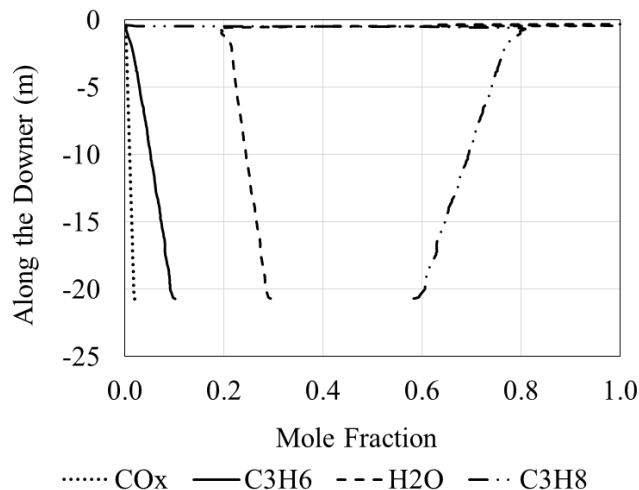


Figure 46: Chemical Special Molar Fractions along the Downer unit.

Figure 47 reports the total fluid molar flowrate through downer reactor from the reactor entry to reactor exit and its changes with simulation time. Again, here it is shown that a 30s simulation time is needed for accurate calculations. Thus, it is found that, along the downer length, the fluid molar flowrate increases moderately from 0.09 mol/s to 0.11mole/s with this being in agreement with the stoichiometric reactions postulated in the parallel-series reaction network.

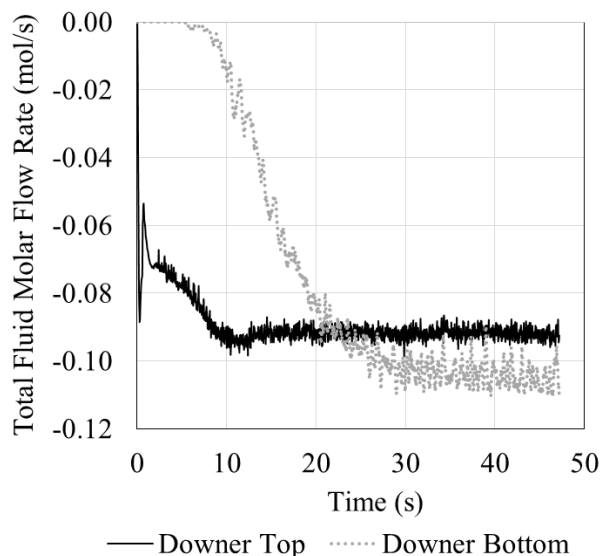


Figure 47: Total Fluid Mass Flowrates at the Downer Reactor Top and Bottom at Various Simulation times.

7.3.5 Temperature Changes due to Reactions

According to the postulated PODH reaction network, reactions (73), (74) and (75) are involved in PODH with catalyst lattice oxygen providing oxygen. This oxygen drives both the slightly endothermic propane oxi-dehydrogenation (reaction (73)) and the highly exothermic combustion of propane and propylene (reactions (74) and (75)). Table 20 reports the needed reaction enthalpies and chemical species and catalyst particles specific heats used in CFPD computations.

Table 20: Reaction Enthalpies and Chemical Species Specific Heats.

$C_3H_8 + V_2O_5 \xrightarrow{k_1} C_3H_6 + V_2O_4 + H_2O; \Delta H_{800K} = 13.52 \text{ KJ/mol}$
$C_3H_8 + 8.5V_2O_5 \xrightarrow{k_2} 1.5CO + 1.5CO_2 + 8.5V_2O_4 + 4H_2O; \Delta H_{800K} = -505.14 \text{ KJ/mol}$
Combining above two equations: $C_3H_8 + 4.75V_2O_5 \rightarrow 0.5C_3H_6 + 1.5CO_x + 4.75V_2O_4 + 2.5H_2O; \Delta H = -245.8 \text{ KJ/mol}$
$\Delta H = [(mC_p)_f + (mC_p)_p](T_2 - T_1)$ Where, $\Delta H = -245.8 \times 10^3 \times (1.8 - 2.2) = 98320 \text{ J}$ $(mC_p)_f = 348 \frac{\text{J}}{\text{K}}; (mC_p)_p = 5151 \frac{\text{J}}{\text{K}}; T_2 = \text{Final temp.}; T_1 = 823 \text{ K}$ So, $T_2 = 841 \text{ K}$

One can notice based on the CFPD calculations that along the downer length, temperature increases moderately both for particle and fluid, as shown in Figure 48. One can thus see that, the temperature increases as calculated by the CFPD model for both fluid and particle clusters is approximately 11-13°C.

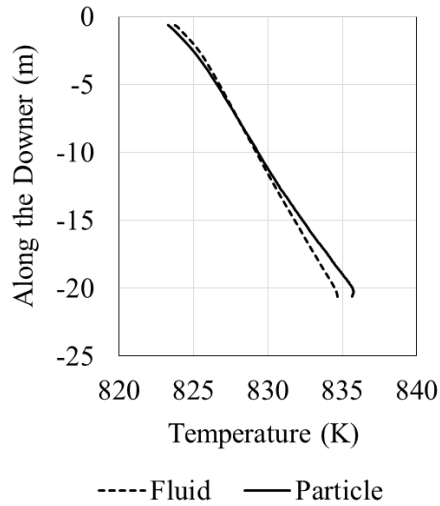
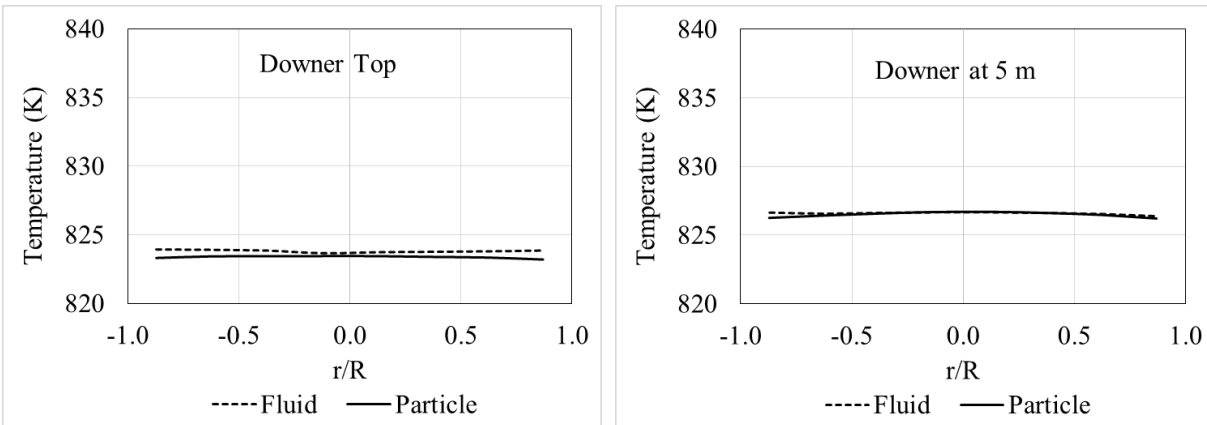


Figure 48: Fluid and Particle Temperature Increases along the Downer Length.

Figure 49 reports the radial temperature profiles in the downer unit for fluid and particle clusters. It is found that, at the downer top, fluid and particle temperatures are approximately 823 K. However, as the suspension moves towards the bottom of the downer and due to the overall exothermicity of the catalytic reactions, temperature differences between particle clusters and fluid augment slightly with the particle clusters having at slightly higher temperature than the fluid.



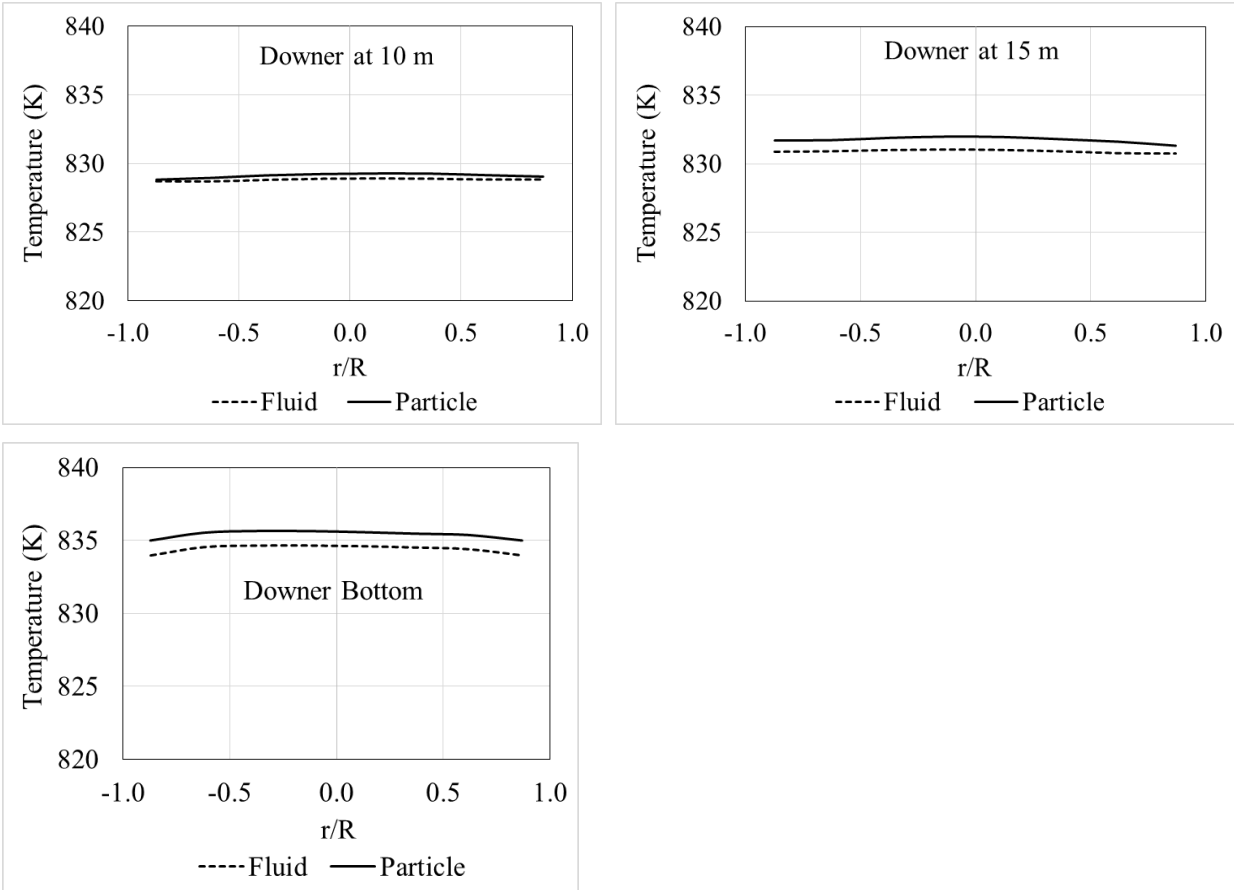


Figure 49: Radial Temperature Profiles for Fluid and Cluster Particle in the Downer.

7.3.6 Downer Simulation Results with the “Single Particle” Model

The proposed CPFD model of the downer for PODH includes particle flow as particle clusters. However, the CPFD can be run as well, with the “single” particle (absent of particle cluster) flow model for the PODH reaction.

Figure 50 reports the axial particle and fluid velocity profile along the downer for the “single” particle (absent of particle cluster) model. It is found that, in the fully developed region, particle velocity is nearly 2.5 m/s whereas fluid velocity is 1.5 m/s. These values are significantly smaller than the 3.5 m/s which were calculated for particle cluster velocity flows. At the bottom of the downer, the presence of the exit cyclone reduces particle and fluid velocity.

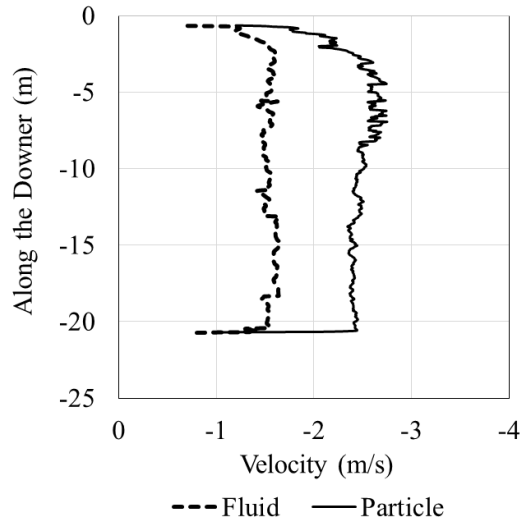


Figure 50: Axial Velocity Profiles for Fluid and Particles using the “Single Particle” (absent of particle clusters) Flow along the Downer Unit.

Figure 51 shows the Particle Volume Fraction along the downer length for “Single Particle” flow. It is found that “Single Particle” flow in the developed region of the downer yields 0.009. This is in clear contrast with the 0.005-0.006 solid fraction obtained in the downer fully developed region accounting for particle clusters.

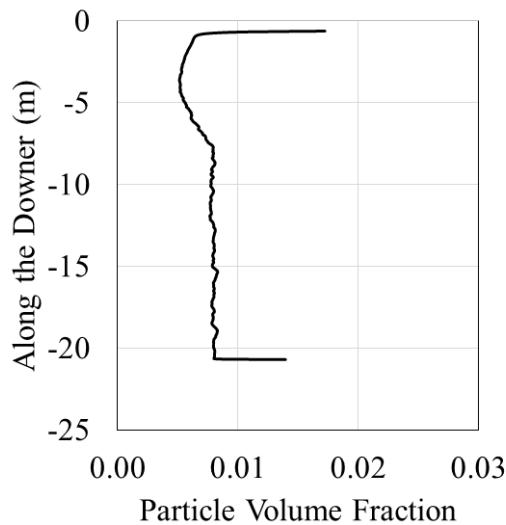


Figure 51: Particle Volume Fraction for the “Single” Particle Flow Model along the Downer.

Figure 52 reports the molar fraction for chemical species fluids using the “Single Particle” (absent of particle clusters) flow model. It can be observed that a propane conversion of 28% is calculated with a propylene selectivity of 93%.

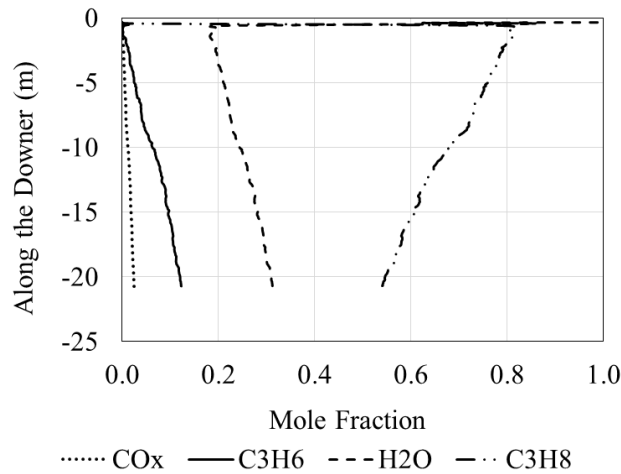


Figure 52: Chemical Species Molar Fraction along the Downer Using the “Single Particle” (absent of particle cluster) Flow Model.

Finally, and consistent with this, Figure 53 reports both fluid and particle temperatures using the “Single Particle” (absent of particle cluster) suspension model with temperature differences between the downer top and bottom reaching 20°C.

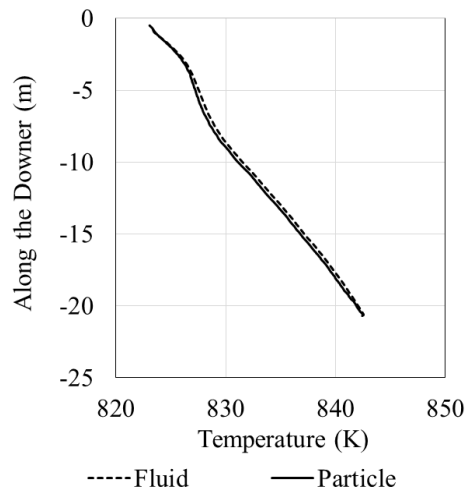


Figure 53: Fluid and Particle Temperature Profile along the Downer using the “Single Particle” (absent of particle cluster) Flow Model.

Thus, as one can see, the results obtained in this section show the significant differences between propane total conversions and temperatures using the “Single Particle” (absent of particle clusters) model and the more meaningful “Particle Cluster” model, reported in the present study.

Thus, and on the basis of the results of the present study, one can conclude that, hybrid CPFD including particle clusters is strongly recommended for simulation and progress with the implementation of large-scale downer reactor units for PODH and other catalytic processes.

7.4 Conclusions

- a) Industrial scale downer fluidized bed reactor simulation requires the use of hybrid CPFD computational models accounting for particle cluster flow.
- b) These CPFD models should consider particle drag coefficients based on non-spherical particle clusters, with particle clusters described as train of particles.
- c) These CPFD models should involve feeding and terminator cyclones which have a significant influence of the particle cluster flow.
- d) These CPFD models should include adequate PODH kinetics as the ones established using the CREC Riser Simulator unit in a previous contribution of our research team.
- e) The proposed CPFD model with realistic PODH kinetics has the potential to lead to accurate calculations of cluster particle velocity and cluster particle concentration, total pressure, temperature, propane conversion and propylene selectivity.

Chapter 8: Conclusions and Recommendations

8.1 Conclusions

The main contributions and findings of the present study can be summarized as follows:

1. It was shown that, the VO_x loaded ZrO₂-γAl₂O₃ catalysts perform advantageously in propane oxidative dehydrogenation under oxygen-free atmospheres. Reported results favor the use of a twin fluidized continuous process, which complies with the required PODH conditions and limited catalyst inventory.
2. It was established via XRD and Raman analyses that VO_x/ZrO₂-γAl₂O₃ catalysts do not show V₂O₅ crystals. The 2.5% and 5% V/ZrO₂-γAl₂O₃ exhibits tetragonal zirconia peaks and the 7.5% V on ZrO₂-γAl₂O₃ displays a monoclinic zirconia phase.
3. It was confirmed using TPR and XPS that, there are two vanadium achievable oxidation states on the catalyst surface: V⁺⁴ and V⁺⁵, with V⁺⁵ being reduced to V⁺⁴ in the presence of hydrogen.
4. It was shown using NH₃-TPD and pyridine-FTIR that the VO_x/γAl₂O₃ (considered as a reference) was more acidic than the VO_x/ZrO₂-γAl₂O₃ catalyst of the present study. This is the case given the VO_x/γAl₂O₃ catalysts, displayed Lewis acid dominant sites, while the VO_x/ZrO₂-γAl₂O₃ catalysts showed more abundant Brønsted acid sites.
5. It was proven that the TPD kinetics displayed the highest desorption energy when using the 7.5% V/ZrO₂-γAl₂O₃ catalyst. This is assigned to an increased vanadium-support interaction, which one can anticipate favors controlled PODH reaction.
6. It was shown employing consecutive propane injection runs in a fluidized CREC Riser Simulator, that the 7.5% V/ZrO₂-γAl₂O₃ catalyst yields a promising 93% propylene selectivity with 25% propane conversion (based on propane converted into gaseous carbon containing products) and 85% propylene selectivity with 28% propane conversion (based on propane converted into carbon containing gaseous products including coke). This was accomplished at a 550°C reaction temperature and 20 s reaction time using 0.76 g catalyst and 10 ml propane injections.
7. It was further established that 7.5% V/ZrO₂-γAl₂O₃ at 500-550°C and 10-20 s reaction times using 10 consecutive propane injections in the CREC Riser Simulator, achieved high propylene selectivity, with injections 4 to 10 yielding consistently the highest 94% propylene selectivity.

Coke formed was in all cases negligible. Following the 10th injection, the 7.5V/ZrO₂- γ Al₂O₃ catalyst was regenerated with lattice oxygen being replenished.

8. It was established that a parallel-series reaction network for the 7.5V/ZrO₂- γ Al₂O₃ (1:1) PODH catalyst was suitable. This heterogeneous kinetic model was based on a Langmuir-Hinshelwood model, with adsorption constants being involved in various catalytic reaction steps.
9. It was proven that for the large DOF (Data points >> kinetic parameters), the 6 independent kinetic parameters (k_1^0 , k_2^0 , k_3^0 , E_1 , E_2 and E_3) of the proposed kinetic model could be calculated successfully using non-linear least squares regression. To accomplish this, the propane, propylene and carbon oxides adsorption constants were determined independently in the CREC Riser Simulator. This led to calculated kinetic parameters with reduced spans for the 95% confidence intervals and low parameter cross-correlation.
10. It was observed that the calculated energy of activation for propylene combustion was higher than that the ones for propane ODH and propane combustion, with the frequency factors being much higher for PODH, as well. This shows the intrinsic ability of a 7.5V/ZrO₂- γ Al₂O₃ (1:1) catalyst to promote high propylene selectivities (94%) at important propane conversions (25%).
11. It was calculated using a CPFD Barracuda software that, 28% propane conversion with 93% propylene selectivity could be obtained in a 20 m downer unit using the “single particle” flow model. However, when particle clusters were accounted for, total propane conversion was reduced to 20% while the propylene selectivity remained at 94% level.
12. It was established that, including feeding and terminator cyclones with downer unit could have a significant influence on the particle cluster flow and increase the propane conversion. It was also proved that, a CPFD model with realistic PODH kinetics can accurately calculate the pressure and temperature profile along with reaction performance along the downer.

8.2 Recommendations

To be ready for industrial applications, the followings are recommended:

- a) The PODH catalyst evaluation should be extended to more than 3 complete consecutive cycles, as developed in the present study. Each reported oxidation-reduction cycle involved 10 successive PODH runs followed by one catalyst re-oxidation.
- b) The CPFD Barracuda simulation should be performed for the complete PODH process including both the downer PODH reactor and the riser re-oxidation unit.

References

- (1) bai, P. T.; Manokaran, V.; Saiprasad, P. S.; Srinath, S. Studies on Heat and Mass Transfer Limitations in Oxidative Dehydrogenation of Ethane Over $\text{Cr}_2\text{O}_3/\text{Al}_2\text{O}_3$ Catalyst. *Procedia Eng.* **2015**, *127*, 1338.
- (2) Khadzhiev, S. N.; Usachev, N. Y.; Gerzeliev, I. M.; Belanova, E. P.; Kalinin, V. P.; Kharlamov, V. V.; Kazakov, A. V.; Kanaev, S. A.; Starostina, T. S.; Popov, A. Y. Oxidative Dehydrogenation of Ethane to Ethylene in a System with Circulating Microspherical Metal Oxide Oxygen Carrier: 1. Synthesis and Study of the Catalytic System. *Pet. Chem.* **2015**, *55* (8), 651.
- (3) Bakare, I. A.; Mohamed, S. A.; Al-Ghamdi, S.; Razzak, S. A.; Hossain, M. M.; de Lasa, H. I. Fluidized Bed ODH of Ethane to Ethylene over $\text{VO}_x\text{-MoO}_x/\gamma\text{-Al}_2\text{O}_3$ Catalyst: Desorption Kinetics and Catalytic Activity. *Chem. Eng. J.* **2015**, *278*, 207.
- (4) Zhai, Z.; Wang, X.; Licht, R.; Bell, A. T. Selective Oxidation and Oxidative Dehydrogenation of Hydrocarbons on Bismuth Vanadium Molybdenum Oxide. *J. Catal.* **2015**, *325*, 87.
- (5) H.Zea, L. C. Oxidative Dehydrogenation of Propane on Pd-Mo/ $\gamma\text{-Al}_2\text{O}_3$ Catalyst: A Kinetic Study. **2015**, *9* (March), 78.
- (6) Khalil, Y. P. Propylene in Demand: Roadblocks and Opportunities.
- (7) Rebsdats, S.; Mayer, D. Ethylene Glycol. *Ullmann's Encycl. Ind. Chem.* **2012**, 547.

- (8) Darvishi, A.; Davand, R.; Khorasheh, F.; Fattahi, M. Modeling-Based Optimization of a Fixed-Bed Industrial Reactor for Oxidative Dehydrogenation of Propane. *Chinese J. Chem. Eng.* **2016**, *24* (5), 612.
- (9) Elbadawi, A. H.; Osman, M. S.; Razzak, S. A.; Hossain, M. M. VO_x-Nb/La- γ -Al₂O₃ Catalysts for Oxidative Dehydrogenation of Ethane to Ethylene. *J. Taiwan Inst. Chem. Eng.* **2016**, *61*, 106.
- (10) Ayandiran, A. A.; Bakare, idris A.; Binous, H.; Al-Ghamdi, S.; Razzak, S. A.; Hossain, M. M. Oxidative Dehydrogenation of Propane to Propylene over VO_x/CaO- γ -Al₂O₃ Using Lattice Oxygen. *Catal. Sci. Technol.* **2016**, *6* (13), 5154.
- (11) Bhasin, M. M. Is True Ethane Oxydehydrogenation Feasible? *Top. Catal.* **2003**, *23* (1–4), 145.
- (12) Al-Ghamdi, S. A.; de Lasa, H. I. Propylene Production via Propane Oxidative Dehydrogenation over VO_x/ γ -Al₂O₃ Catalyst. *Fuel* **2014**, *128*, 120.
- (13) Gao, Y.; Neal, L. M.; Li, F. Li-Promoted LaSrFeO Core–Shell Redox Catalysts for Oxidative Dehydrogenation of Ethane under a Cyclic Redox Scheme. *ACS Catal.* **2016**, *6* (11), 7293.
- (14) Setnička, M.; Tišler, Z.; Kubička, D.; Bulánek, R. Activity of Molybdenum Oxide Catalyst Supported on Al₂O₃, TiO₂, and SiO₂ Matrix in the Oxidative Dehydrogenation of n-Butane. *Top. Catal.* **2015**, *58* (14–17), 866.
- (15) Koirala, R.; Buechel, R.; Pratsinis, S. E.; Baiker, A. Silica Is Preferred over Various Single and Mixed Oxides as Support for CO₂-Assisted Cobalt-Catalyzed Oxidative Dehydrogenation of Ethane. *Appl. Catal. A Gen.* **2016**, *527*, 96.
- (16) Ren, T.; Patel, M.; Blok, K. Olefins from Conventional and Heavy Feedstocks: Energy Use in Steam Cracking and Alternative Processes. *Energy* **2006**, *31* (4), 425.
- (17) Barghi, B.; Fattahi, M.; Khorasheh, F. The Modeling of Kinetics and Catalyst Deactivation in Propane Dehydrogenation Over Pt-Sn/ γ -Al₂O₃ in Presence of Water as an

- Oxygenated Additive. *Pet. Sci. Technol.* **2014**, 32 (10), 1139.
- (18) Cavani, F.; Trifirò, F. The Oxidative Dehydrogenation of Ethane and Propane as an Alternative Way for the Production of Light Olefins. *Catal. Today* **1995**, 24 (3), 307.
- (19) Sanfilippo, D. Dehydrogenation of Paraffins; Key Technology for Petrochemicals and Fuels. *Cattech* **2000**, 4 (1), 56.
- (20) Cavani, F.; Ballarini, N.; Cericola, A. Oxidative Dehydrogenation of Ethane and Propane: How Far from Commercial Implementation? *Catal. Today* **2007**, 127 (1–4), 113.
- (21) Chu, B.; Truter, L.; Nijhuis, T. A.; Cheng, Y. Oxidative Dehydrogenation of Ethane to Ethylene over Phase-Pure M1 MoVNbTeO_x Catalysts in a Micro-Channel Reactor. *Catal. Sci. Technol.* **2015**, 5 (5), 2807.
- (22) Botková, Š.; Čapek, L.; Setnička, M.; Bulánek, R.; Čičmanec, P.; Kalužová, A.; Pastva, J.; Zúkal, A. VO_x Species Supported on Al₂O₃–SBA-15 Prepared by the Grafting of Alumina onto SBA-15: Structure and Activity in the Oxidative Dehydrogenation of Ethane. *React. Kinet. Mech. Catal.* **2016**, 119 (1), 319.
- (23) Koc, S. N.; Dayioglu, K.; Ozdemir, H. Oxidative Dehydrogenation of Propane with K-MoO₃/MgAl₂O₄ Catalysts. *J. Chem. Sci.* **2016**, 128 (1), 67.
- (24) Kong, L.; Li, J.; Zhao, Z.; Liu, Q.; Sun, Q.; Liu, J.; Wei, Y. Oxidative Dehydrogenation of Ethane to Ethylene over Mo-Incorporated Mesoporous SBA-16 Catalysts: The Effect of MoO_x Dispersion. *Appl. Catal. A Gen.* **2016**, 510, 84.
- (25) Jermy, B. R.; Ajayi, B. P.; Abussaud, B. A.; Asaoka, S.; Al-Khattaf, S. Oxidative Dehydrogenation of n-Butane to Butadiene over Bi–Ni–O/γ-Alumina Catalyst. *J. Mol. Catal. A Chem.* **2015**, 400, 121.
- (26) Gascón, J.; Valenciano, R.; Téllez, C.; Herguido, J.; Menéndez, M. A Generalized Kinetic Model for the Partial Oxidation of N-Butane to Maleic Anhydride under Aerobic and Anaerobic Conditions. *Chem. Eng. Sci.* **2006**, 61 (19), 6385.

- (27) Rubio, O.; Herguido, J.; Menéndez, M. Oxidative Dehydrogenation of n-Butane on V/MgO Catalysts-Kinetic Study in Anaerobic Conditions. *Chem. Eng. Sci.* **2003**, *58* (20), 4619.
- (28) Wu, Y.; Gao, J.; He, Y.; Wu, T. Preparation and Characterization of Ni–Zr–O Nanoparticles and Its Catalytic Behavior for Ethane Oxidative Dehydrogenation. *Appl. Surf. Sci.* **2012**, *258* (11), 4922.
- (29) Fattahi, M.; Kazemeini, M.; Khorasheh, F.; Rashidi, A. An Investigation of the Oxidative Dehydrogenation of Propane Kinetics over a Vanadium–graphene Catalyst Aiming at Minimizing of the CO_x Species. *Chem. Eng. J.* **2014**, *250*, 14.
- (30) Mukherjee, D.; Park, S.-E.; Reddy, B. M. CO₂ as a Soft Oxidant for Oxidative Dehydrogenation Reaction: An Eco Benign Process for Industry. *J. CO₂ Util.* **2016**, *16*, 301.
- (31) Frank, B.; Dinse, A.; Ovsitser, O.; Kondratenko, E. V.; Schomäcker, R. Mass and Heat Transfer Effects on the Oxidative Dehydrogenation of Propane (ODP) over a Low Loaded VO_x/Al₂O₃ Catalyst. *Appl. Catal. A Gen.* **2007**, *323*, 66.
- (32) Valverde, J. A.; Echavarría, A.; Eon, J.-G.; Faro, A. C.; Palacio, L. A. V–Mg–Al Catalyst from Hydrotalcite for the Oxidative Dehydrogenation of Propane. *React. Kinet. Mech. Catal.* **2014**, *111* (2), 679.
- (33) Fukudome, K.; Suzuki, T. Highly Selective Oxidative Dehydrogenation of Propane to Propylene over VO_x–SiO₂ Catalysts. *Catal. Surv. from Asia* **2015**, *19* (3), 172.
- (34) Siahvashi, A.; Chesterfield, D.; Adesina, A. A. Nonoxidative and Oxidative Propane Dehydrogenation over Bimetallic Mo–Ni/Al₂O₃ Catalyst. *Ind. Eng. Chem. Res.* **2013**, *52* (11), 4017.
- (35) Sinev, M. Y.; Fattakhova, Z. T.; Tulenin, Y. P.; Stennikov, P. S.; Vislovskii, V. P. Hydrogen Formation during Dehydrogenation of C₂–C₄ Alkanes in the Presence of Oxygen: Oxidative or Non-Oxidative? *Catal. Today* **2003**, *81* (2), 107.

- (36) Fu, B.; Lu, J.; Stair, P. C.; Xiao, G.; Kung, M. C.; Kung, H. H. Oxidative Dehydrogenation of Ethane over Alumina-Supported Pd Catalysts. Effect of Alumina Overlayer. *J. Catal.* **2013**, *297*, 289.
- (37) Carrero, C.; Kauer, M.; Dinse, A.; Wolfram, T.; Hamilton, N.; Trunschke, A.; Schlögl, R.; Schomäcker, R. High Performance $(VO_x)_n-(TiO_x)_m/SBA-15$ Catalysts for the Oxidative Dehydrogenation of Propane. *Catal. Sci. Technol.* **2014**, *4* (3), 786.
- (38) Carrero, C. A.; Schlögl, R.; Wachs, I. E.; Schomaecker, R. Critical Literature Review of the Kinetics for the Oxidative Dehydrogenation of Propane over Well-Defined Supported Vanadium Oxide Catalysts. *ACS Catal.* **2014**, *4* (10), 3357.
- (39) Dar, H. J.; Nanot, S. U.; Jens, K. J.; Jakobsen, H. a.; Tangstad, E.; Chen, D. Kinetic Analysis and Upper Bound of Ethylene Yield of Gas Phase Oxidative Dehydrogenation of Ethane to Ethylene. *Ind. Eng. Chem. Res.* **2012**, *51* (32), 10571.
- (40) Ahmed, S.; Rahman, F.; Al-Amer, A. M. J.; Al-Mutairi, E. M.; Baduruthamal, U.; Alam, K. Oxidative Dehydrogenation of Lower Alkanes over Metal Incorporated MCM-41 Catalysts. *React. Kinet. Mech. Catal.* **2012**, *105* (2), 483.
- (41) Schwarz, O.; Habel, D.; Ovsitser, O.; Kondratenko, E. V.; Hess, C.; Schomäcker, R.; Schubert, H. Impact of Preparation Method on Physico-Chemical and Catalytic Properties of $VO_x/\gamma-Al_2O_3$ Materials. *J. Mol. Catal. A Chem.* **2008**, *293* (1–2), 45.
- (42) Mishanin, I. I.; Kalenchuk, A. N.; Maslakov, K. I.; Lunin, V. V.; Koklin, A. E.; Finashina, E. D.; Bogdan, V. I. Deactivation of a Mixed Oxide Catalyst of Mo–V–Te–Nb–O Composition in the Reaction of Oxidative Ethane Dehydrogenation. *Russ. J. Phys. Chem. A* **2016**, *90* (6), 1132.
- (43) Ajayi, B. P.; Rabindran Jermy, B.; Abussaud, B. A.; Al-Khattaf, S. Oxidative Dehydrogenation of n-Butane over Bimetallic Mesoporous and Microporous Zeolites with CO_2 as Mild Oxidant. *J. Porous Mater.* **2013**, *20* (5), 1257.
- (44) Koirala, R.; Buechel, R.; Krumeich, F.; Pratsinis, S. E.; Baiker, A. Oxidative Dehydrogenation of Ethane with CO_2 over Flame-Made Ga-Loaded TiO_2 . *ACS Catal.*

- 2015**, 5 (2), 690.
- (45) Kowalska-Kuś, J.; Held, A.; Nowińska, K. Oxydehydrogenation of C₂–C₄ Hydrocarbons over Fe-ZSM-5 Zeolites with N₂O as an Oxidant. *Catal. Sci. Technol.* **2013**, 3 (2), 508.
- (46) Kondratenko, E. V.; Cherian, M.; Baerns, M.; Su, D.; Schlogl, R.; Wang, X.; Wachs, I. E. Oxidative Dehydrogenation of Propane over V/MCM-41 Catalysts: Comparison of O₂ and N₂O as Oxidants. *J. Catal.* **2005**, 234 (1), 131.
- (47) Védrine, J. Heterogeneous Partial (Amm)Oxidation and Oxidative Dehydrogenation Catalysis on Mixed Metal Oxides. *Catalysts* **2016**, 6 (2), 22.
- (48) Talati, A.; Haghghi, M.; Rahmani, F. Impregnation vs. Coprecipitation Dispersion of Cr over TiO₂ and ZrO₂ Used as Active and Stable Nanocatalysts in Oxidative Dehydrogenation of Ethane to Ethylene by Carbon Dioxide. *RSC Adv.* **2016**, 6 (50), 44195.
- (49) Liu, H.; Zhang, Z.; Li, H.; Huang, Q. Intrinsic Kinetics of Oxidative Dehydrogenation of Propane in the Presence of CO₂ over Cr/MSU-1 Catalyst. *J. Nat. Gas Chem.* **2011**, 20 (3), 311.
- (50) Qiao, A.; Kalevaru, V. N.; Radnik, J.; Martin, A. Oxidative Dehydrogenation of Ethane to Ethylene over Ni–Nb–M–O Catalysts: Effect of Promoter Metal and CO₂-Admixture on the Performance. *Catal. Today* **2016**, 264, 144.
- (51) Elfadly, A. M.; Badawi, A. M.; Yehia, F. Z.; Mohamed, Y. A.; Betiha, M. A.; Rabie, A. M. Selective Nano Alumina Supported Vanadium Oxide Catalysts for Oxidative Dehydrogenation of Ethylbenzene to Styrene Using CO₂ as Soft Oxidant. *Egypt. J. Pet.* **2013**, 22 (3), 373.
- (52) Ramesh, Y.; Thirumala Bai, P.; Hari Babu, B.; Lingaiah, N.; Rama Rao, K. S.; Prasad, P. S. S. Oxidative Dehydrogenation of Ethane to Ethylene on Cr₂O₃/Al₂O₃–ZrO₂ Catalysts: The Influence of Oxidizing Agent on Ethylene Selectivity. *Appl. Petrochemical Res.* **2014**, 4 (3), 247.

- (53) Raju, G.; Reddy, B. M.; Abhishek, B.; Mo, Y.; Park, S. Synthesis of C₄ Olefins from n-Butane over a Novel VO_x/SnO₂-ZrO₂ Catalyst Using CO₂ as Soft Oxidant. *Appl. Catal. A Gen.* **2012**, 423–424, 168.
- (54) Elbadawi, A. H.; Ba-Shammakh, M. S.; Al-Ghamdi, S.; Razzak, S. A.; Hossain, M. M.; de Lasa, H. I. Phenomenologically Based Kinetics of ODH of Ethane to Ethylene Using Lattice Oxygen of VO_x/Al₂O₃-ZrO₂ Catalyst. *Chem. Eng. Res. Des.* **2017**, 117, 733.
- (55) Al-Ghamdi, S.; Volpe, M.; Hossain, M. M.; de Lasa, H. VO_x/c-Al₂O₃ Catalyst for Oxidative Dehydrogenation of Ethane to Ethylene: Desorption Kinetics and Catalytic Activity. *Appl. Catal. A Gen.* **2013**, 450, 120.
- (56) Elbadawi, A. H.; Ba-Shammakh, M. S.; Al-Ghamdi, S.; Razzak, S. A.; Hossain, M. M.; de Lasa, H. I. A Fluidizable VO_x/γ-Al₂O₃-ZrO₂ Catalyst for the ODH of Ethane to Ethylene Operating in a Gas Phase Oxygen Free Environment. *Chem. Eng. Sci.* **2016**, 145, 59.
- (57) Sedor, K. E.; Hossain, M. M.; De Lasa, H. I. Reduction Kinetics of a Fluidizable Nickel-Alumina Oxygen Carrier for Chemical-Looping Combustion. *Can. J. Chem. Eng.* **2008**, 86 (3), 323.
- (58) Khan, M. Y.; Al-Ghamdi, S.; Razzak, S. A.; Hossain, M. M.; de Lasa, H. Fluidized Bed Oxidative Dehydrogenation of Ethane to Ethylene over VO_x/Ce-γAl₂O₃ catalysts: Reduction Kinetics and Catalyst Activity. *Mol. Catal.* **2017**.
- (59) Rostom, S.; de Lasa, H. I. Propane Oxidative Dehydrogenation Using Consecutive Feed Injections and Fluidizable VO_x/γAl₂O₃ and VO_x/ZrO₂-γAl₂O₃ Catalysts. *Ind. Eng. Chem. Res.* **2017**, 56 (45), 13109.
- (60) Rostom, S.; de Lasa, H. High Propylene Selectivity via Propane Oxidative Dehydrogenation Using a Novel Fluidizable Catalyst: Kinetic Modeling. *Ind. Eng. Chem. Res.* **2018**, 57 (31), 10251.
- (61) Hossain, M. M. Kinetics of Oxidative Dehydrogenation of Propane to Propylene Using Lattice Oxygen of VO_x/CaO/γAl₂O₃ Catalysts. *Ind. Eng. Chem. Res.* **2017**, 56 (15), 4309.

- (62) Fukudome, K.; Ikenaga, N. O.; Miyake, T.; Suzuki, T. Oxidative Dehydrogenation of Alkanes over Vanadium Oxide Prepared with $V(t\text{-BuO})_3O$ and $Si(OEt)_4$ in the Presence of Polyethyleneglycol. *Catal. Today* **2013**.
- (63) Fukudome, K.; Ikenaga, N.; Miyake, T.; Suzuki, T. Oxidative Dehydrogenation of Propane Using Lattice Oxygen of Vanadium Oxides on Silica. *Catal. Sci. Technol.* **2011**, *1* (6), 987.
- (64) Rischard, J.; Antinori, C.; Maier, L.; Deutschmann, O. Oxidative Dehydrogenation of n-Butane to Butadiene with Mo-V-MgO Catalysts in a Two-Zone Fluidized Bed Reactor. *Appl. Catal. A Gen.* **2016**, *511*, 23.
- (65) Rodríguez, M. L.; Ardisson, D. E.; López, E.; Pedernera, M. N.; Borio, D. O. Reactor Designs for Ethylene Production via Ethane ODH : Comparison of Performance. *Engineering* **2010**, *2010* (Imccre), 45.
- (66) Chalakov, L.; Rihko-Struckmann, L. K.; Munder, B.; Sundmacher, K. Oxidative Dehydrogenation of Ethane in an Electrochemical Packed-Bed Membrane Reactor: Model and Experimental Validation. *Chem. Eng. J.* **2009**, *145* (3), 385.
- (67) Zaynali, Y.; Alavi-Amleshi, S. M. Comparative Study of Propane Oxidative Dehydrogenation in Fluidized and Fixed Bed Reactor. *Part. Sci. Technol.* **2016**, *6351* (August), 1.
- (68) Torabi, A.; Kazemeini, M.; Fattahi, M. Developing a Mathematical Model for the Oxidative Dehydrogenation of Propane in a Fluidized Bed Reactor. *Asia-Pacific J. Chem. Eng.* **2016**, *11* (3), 448.
- (69) Smith, J. M.; Van Ness, H. C.; Abbott, M. M. *Introduction to Chemical Engineering Thermodynamics*; 2005; Vol. 27.
- (70) Hossain, M. M. Chemical-Looping Combustion With Gaseous Fuels: Thermodynamic Parametric Modeling. *Arab. J. Sci. Eng.* **2014**, *39* (5), 3415.
- (71) De Lasa, H.; Salaices, E.; Mazumder, J.; Lucky, R. Catalytic Steam Gasification of

- Biomass: Catalysts, Thermodynamics and Kinetics. *Chem. Rev.* **2011**, *111* (9), 5404.
- (72) Grant, J. T.; Love, A. M.; Carrero, C. A.; Huang, F.; Panger, J.; Verel, R.; Hermans, I. Improved Supported Metal Oxides for the Oxidative Dehydrogenation of Propane. *Top. Catal.* **2016**.
- (73) Zea, H.; Carballo, L. M. Kinetic Evaluation of Pd Alumina Supported Catalyst for the Reaction of Oxidative Dehydrogenation of Propane. *ARPJ. Eng. Appl. Sci.* **2015**, *10* (2), 896.
- (74) Oyama, S. T.; Somorjai, G. A. Effect of Structure in Selective Oxide Catalysis: Oxidation Reactions of Ethanol and Ethane on Vanadium Oxide. *J. Phys. Chem.* **1990**, *94* (12), 5022.
- (75) Ciambelli, P.; Galli, P.; Lisi, L.; Massucci, M. A.; Patrono, P.; Pirone, R.; Ruoppolo, G.; Russo, G. TiO₂ Supported Vanadyl Phosphate as Catalyst for Oxidative Dehydrogenation of Ethane to Ethylene. *Appl. Catal. A Gen.* **2000**.
- (76) Fukudome, K.; Ikenaga, N.; Miyake, T.; Suzuki, T. Oxidative Dehydrogenation of Propane Using Lattice Oxygen of Vanadium Oxides on Silica. *Catal. Sci. Technol.* **2011**, *1* (3), 987.
- (77) Dinse, A.; Schomäcker, R.; Bell, A. T. The Role of Lattice Oxygen in the Oxidative Dehydrogenation of Ethane on Alumina-Supported Vanadium Oxide. *Phys. Chem. Chem. Phys.* **2009**, *11* (29), 6119.
- (78) Al-Ghamdi, S.; Volpe, M.; Hossain, M. M.; De Lasa, H. VO_x/c-Al₂O₃ Catalyst for Oxidative Dehydrogenation of Ethane to Ethylene: Desorption Kinetics and Catalytic Activity. *Appl. Catal. A Gen.* **2013**.
- (79) Xu, B.; Zhu, X.; Cao, Z.; Yang, L.; Yang, W. Catalytic Oxidative Dehydrogenation of n-Butane over V₂O₅/MO-Al₂O₃ (M = Mg, Ca, Sr, Ba) Catalysts. *Chinese J. Catal.* **2015**, *36* (7), 1060.
- (80) Martínez-Huerta, M. V.; Gao, X.; Tian, H.; Wachs, I. E.; Fierro, J. L. G.; Banares, M. A.

- Oxidative Dehydrogenation of Ethane to Ethylene over Alumina-Supported Vanadium Oxide Catalysts: Relationship between Molecular Structures and Chemical Reactivity. *Catal. Today* **2006**, *118* (3–4 SPEC. ISS.), 279.
- (81) Enache, D. I.; Bordes-Richard, E.; Ensuque, A.; Bozon-Verduraz, F. Vanadium Oxide Catalysts Supported on Zirconia and Titania I. Preparation and Characterization. *Appl. Catal. A Gen.* **2004**.
- (82) Gao, X. In Situ UV–vis–NIR Diffuse Reflectance and Raman Spectroscopic Studies of Propane Oxidation over ZrO₂-Supported Vanadium Oxide Catalysts. *J. Catal.* **2002**, *209* (1), 43.
- (83) Rossetti, I.; Mancini, G. F.; Ghigna, P.; Scavini, M.; Piumetti, M.; Bonelli, B.; Cavani, F.; Comite, A. Spectroscopic Enlightening of the Local Structure of VO_x Active Sites in Catalysts for the ODH of Propane. *J. Phys. Chem. C* **2012**, *116* (42), 22386.
- (84) Weckhuysen, B. M.; Keller, D. E. Chemistry, Spectroscopy and the Role of Supported Vanadium Oxides in Heterogeneous Catalysis. *Catal. Today* **2003**, *78* (1–4 SPEC.), 25.
- (85) Wu, Z.; Kim, H. S.; Stair, P. C.; Rugmini, S.; Jackson, S. D. On the Structure of Vanadium Oxide Supported on Aluminas: UV and Visible Raman Spectroscopy, UV-Visible Diffuse Reflectance Spectroscopy, and Temperature-Programmed Reduction Studies. *J. Phys. Chem. B* **2005**.
- (86) Argyle, M. D.; Chen, K.; Bell, A. T.; Iglesia, E. Effect of Catalyst Structure on Oxidative Dehydrogenation of Ethane and Propane on Alumina-Supported Vanadia. *J. Catal.* **2002**.
- (87) Klose, F.; Wolff, T.; Lorenz, H.; Seidel-morgenstern, A.; Suchorski, Y.; Piorkowska, M.; Weiss, H. Active Species on γ -Alumina-Supported Vanadia Catalysts: Nature and Reducibility. *J. Catal.* **2007**, *247* (2), 176.
- (88) Murgia, V.; Sham, E.; Gottifredi, J. C.; Torres, E. M. F. Oxidative Dehydrogenation of Propane and n-Butane over Alumina Supported Vanadium Catalysts. *Lat. Am. Appl. Res.* **2004**, *34* (2), 75.

- (89) Wachs, I. E.; Jehng, J.-M.; Deo, G.; Weckhuysen, B. M.; Guliants, V. V.; Benziger, J. B. In Situ Raman Spectroscopy Studies of Bulk and Surface Metal Oxide Phases during Oxidation Reactions. *Catal. Today* **1996**, *32* (1–4), 47.
- (90) Wachs, I. E.; Weckhuysen, B. M. Structure and Reactivity of Surface Vanadium Oxide Species on Oxide Supports. *Appl. Catal. A Gen.* **1997**, *157* (1–2), 67.
- (91) Deo, G.; Wachs, I. E. Reactivity of Supported Vanadium Oxide Catalysts: The Partial Oxidation of Methanol. *Journal of Catalysis*. 1994.
- (92) Blasco, T.; Nieto, J. M. L.; Dejoz, A.; Vázquez, M. I. Influence of the Acid-Base Character of Supported Vanadium Catalysts on Their Catalytic Properties for the Oxidative Dehydrogenation of n-Butane. *J. Catal.* **1995**.
- (93) Nieto, J. L. The Selective Oxidative Activation of Light Alkanes. From Supported Vanadia to Multicomponent Bulk V-Containing Catalysts. *Top. Catal.* **2006**, *41* (1–4), 3.
- (94) Blasco, T.; Lopez-Nieto, J. M. Oxidative Dehydrogenation of Short Chain Alkanes on Supported Vanadium Oxide Catalysts. *Appl. Catal. A Gen.* **1997**, *157* (1–2), 117.
- (95) Galli, A.; López Nieto, J. M.; Dejoz, A.; Vazquez, M. I. The Effect of Potassium on the Selective Oxidation of n-Butane and Ethane over Al₂O₃-Supported Vanadia Catalysts. *Catal. Letters* **1995**.
- (96) Chen, K.; Bell, A. T.; Iglesia, E. The Relationship between the Electronic and Redox Properties of Dispersed Metal Oxides and Their Turnover Rates in Oxidative Dehydrogenation Reactions. *J. Catal.* **2002**, *209* (1), 35.
- (97) Lemonidou, A. A.; Nalbandian, L.; Vasalos, I. A. Oxidative Dehydrogenation of Propane over Vanadium Oxide Based Catalysts: Effect of Support and Alkali Promoter. *Catal. Today* **2000**, *61* (1–4), 333.
- (98) Ayandiran, A.; Bakare, idris A.; Binous, H.; Al-Ghamdi, S.; Razzak, S.; Hossain, M. M. Oxidative Dehydrogenation of Propane to Propylene over VO_x/CaO-γAl₂O₃ Using Lattice Oxygen. *Catal. Sci. Technol.* **2016**, *6*, 17.

- (99) Baerns, M.; Buyevskaya, O. V. Simple Chemical Processes Based on Low Molecular-Mass Alkanes as Chemical Feedstocks. *Catal. Today* **1998**, *45* (1–4), 13.
- (100) Dinse, A.; Frank, B.; Hess, C.; Habel, D.; Schomäcker, R. Oxidative Dehydrogenation of Propane over Low-Loaded Vanadia Catalysts: Impact of the Support Material on Kinetics and Selectivity. *J. Mol. Catal. A Chem.* **2008**, *289* (1–2), 28.
- (101) Al-Ghamdi, S.; Moreira, J.; de Lasa, H. Kinetic Modeling of Propane Oxidative Dehydrogenation over $\text{VO}_x/\gamma\text{-Al}_2\text{O}_3$ Catalysts in the Chemical Reactor Engineering Center Riser Reactor Simulator. *Ind. Eng. Chem. Res.* **2014**, *53* (40), 15317.
- (102) Daniell, W.; Ponchel, A.; Kuba, S.; Anderle, F.; Weingand, T.; Gregory, D. H.; Kno, H. Characterization and Catalytic Behavior of $\text{VO}_x\text{-CeO}_2$ Catalysts for the Oxidative Dehydrogenation of Propane. *Top. Catal.* **2002**, *20* (July), 65.
- (103) Yang, S.; Iglesia, E.; Bell, A. T. Oxidative Dehydrogenation of Propane over $\text{V}_2\text{O}_5/\text{MoO}_3/\text{Al}_2\text{O}_3$ and $\text{V}_2\text{O}_5/\text{Cr}_2\text{O}_3/\text{Al}_2\text{O}_3$: Structural Characterization and Catalytic Function. *J. Phys. Chem. B* **2005**, *109* (18), 8987.
- (104) Grabowski, R.; Słoczyński, J. Kinetics of Oxidative Dehydrogenation of Propane and Ethane on VO_x/SiO_2 Pure and with Potassium Additive. *Chem. Eng. Process. Process Intensif.* **2005**, *44* (10), 1082.
- (105) Chen, K.; Iglesia, E.; Bell, A. T. Kinetic Isotopic Effects in Oxidative Dehydrogenation of Propane on Vanadium Oxide Catalysts. *J. Catal.* **2000**, *192* (1), 197.
- (106) Balcaen, V.; Sack, I.; Olea, M.; Marin, G. B. Transient Kinetic Modeling of the Oxidative Dehydrogenation of Propane over a Vanadia-Based Catalyst in the Absence of O_2 . *Appl. Catal. A Gen.* **2009**, *371* (1–2), 31.
- (107) Vannice, M. A. An Analysis of the Mars–van Krevelen Rate Expression. *Catal. Today* **2007**, *123* (1–4), 18.
- (108) Fattahi, M.; Kazemeini, M.; Khorasheh, F.; Rashidi, A. Kinetic Modeling of Oxidative Dehydrogenation of Propane (ODHP) over a Vanadium–graphene Catalyst: Application

- of the DOE and ANN Methodologies. *J. Ind. Eng. Chem.* **2014**, *20* (4), 2236.
- (109) You, R.; Zhang, X.; Luo, L.; Pan, Y.; Pan, H.; Yang, J.; Wu, L.; Zheng, X.; Jin, Y.; Huang, W. NbO_x/CeO₂-Rods Catalysts for Oxidative Dehydrogenation of Propane: Nb–CeO₂ Interaction and Reaction Mechanism. *J. Catal.* **2017**, *348*, 189.
- (110) Wang, L.; Chu, W.; Jiang, C.; Liu, Y.; Wen, J.; Xie, Z. Oxidative Dehydrogenation of Propane over Ni-Mo-Mg-O Catalysts. *J. Nat. Gas Chem.* **2012**, *21* (1), 43.
- (111) Fattahi, M.; Kazemeini, M.; Khorasheh, F.; Darvishi, A.; Rashidi, A. M. Fixed-Bed Multi-Tubular Reactors for Oxidative Dehydrogenation in Ethylene Process. *Chem. Eng. Technol.* **2013**, *36* (10), 1691.
- (112) Kotanjac, Ž. S.; van Sint Annaland, M.; Kuipers, J. A. M. A Packed Bed Membrane Reactor for the Oxidative Dehydrogenation of Propane on a Ga₂O₃/MoO₃ Based Catalyst. *Chem. Eng. Sci.* **2010**, *65* (1), 441.
- (113) Che-Galicia, G.; Ruiz-Martínez, R. S.; López-Isunza, F.; Castillo-Araiza, C. O. Modeling of Oxidative Dehydrogenation of Ethane to Ethylene on a MoVTeNbO/TiO₂ Catalyst in an Industrial-Scale Packed Bed Catalytic Reactor. *Chem. Eng. J.* **2015**, *280*, 682.
- (114) Al-Ghamdi, S. A.; Hossain, M. M.; de Lasa, H. I. Kinetic Modeling of Ethane Oxidative Dehydrogenation over VO_x/Al₂O₃ Catalyst in a Fluidized-Bed Riser Simulator. *Ind. Eng. Chem. Res.* **2013**, *52* (14), 5235.
- (115) Elbadawi, A. H.; Khan, M. Y.; Quddus, M. R.; Razzak, S. A.; Hossain, M. M. Kinetics of Oxidative Cracking of N-Hexane to Olefins over VO_x/Ce-Al₂O₃ under Gas Phase Oxygen-Free Environment. *AIChE J.* **2017**, *63* (1), 130.
- (116) Argyle, M.; Bartholomew, C. Heterogeneous Catalyst Deactivation and Regeneration: A Review. *Catalysts* **2015**, *5* (1), 145.
- (117) Lasa, D. Riser Simulator. **1992**.
- (118) Elbadawi, A. H.; Ba-Shammakh, M. S.; Al-Ghamdi, S.; Razzak, S. A.; Hossain, M. M.

Reduction Kinetics and Catalytic Activity of VO_x/γ-Al₂O₃-ZrO₂ for Gas Phase Oxygen Free ODH of Ethane. *Chem. Eng. J.* **2016**, *284*, 448.

- (119) Kunii, D.; Levenspiel, O. Introduction. In *Fluidization Engineering*; Elsevier, 1991; pp 1–13.
- (120) Tu, Q.; Wang, H. CPFD Study of a Full-Loop Three-Dimensional Pilot-Scale Circulating Fluidized Bed Based on EMMS Drag Model. *Powder Technol.* **2018**, *323*, 534.
- (121) Deng, R.; Wei, F.; Liu, T.; Jin, Y. Radial Behavior in Riser and Downer during the FCC Process. *Chem. Eng. Process.* **2002**, *41* (3), 259.
- (122) Zhang, H.; Zhu, J. X.; Bergougnou, M. A. Hydrodynamics in Downflow Fluidized Beds (1): Solids Concentration Profiles and Pressure Gradient Distributions. *Chem. Eng. Sci.* **1999**, *54* (22), 5461.
- (123) Zhang, H.; Zhu, J. X. Hydrodynamics in Downflow Fluidized Beds (2): Particle Velocity and Solids Flux Profiles. *Chem. Eng. Sci.* **2000**, *55* (19), 4367.
- (124) Zhu, J.; Yu, Z.; Jin, Y.; Grace, J. R.; Issangya, A. Cocurrent Downflow Circulating Fluidized Bed (Downer) Reactors - A State of the Art Review. *Can. J. Chem. Eng.* **1995**, *73* (5), 662.
- (125) Koratiya, V. K.; Kumar, S.; Sinha, S. Modeling, Simulation and Optimization of FCC Downer Reactor. *Pet. Coal* **2010**, *52* (3), 183.
- (126) Lanza, A.; Islam, M. A.; de Lasa, H. Particle Clusters and Drag Coefficients in Gas-Solid Downer Units. *Chem. Eng. J.* **2012**, *200–202*, 439.
- (127) Ashraful Islam, M.; Krol, S.; De Lasa, H. I. The CREC-GS-Optiprobes and Its Focal Region. Gas-Solid Flow Measurements in down Flow Reactors. *Chem. Eng. Sci.* **2011**, *66* (8), 1671.
- (128) Nova, S.; Krol, S.; De Lasa, H. Particle Velocity and Particle Clustering in Down-Flow Reactors. In *Powder Technology*; 2004; Vol. 148, pp 172–185.

- (129) Krol, S.; Pekediz, A.; De Lasa, H. Particle Clustering in down Flow Reactors. *Powder Technol.* **2000**, *108* (1), 6.
- (130) Liang, Y.; Zhang, Y.; Li, T.; Lu, C. A Critical Validation Study on CPFD Model in Simulating Gas–solid Bubbling Fluidized Beds. *Powder Technol.* **2014**, *263*, 121.
- (131) Andrews, M. J.; O'Rourke, P. J. The Multiphase Particle-in-Cell (MP-PIC) Method for Dense Particulate Flows. *Int. J. Multiph. Flow* **1996**, *22* (2), 379.
- (132) Li, F.; Song, F.; Benyahia, S.; Wang, W.; Li, J. MP-PIC Simulation of CFB Riser with EMMS-Based Drag Model. *Chem. Eng. Sci.* **2012**, *82*, 104.
- (133) Rourke, P. J.; Snider, D. M. Inclusion of Collisional Return-to-Isotropy in the MP-PIC Method. *Chem. Eng. Sci.* **2012**, *80*, 39.
- (134) Abbasi, A.; Islam, M. A.; Ege, P. E.; de Lasa, H. I. CPFD Flow Pattern Simulation in Downer Reactors. *AIChE J.* **2013**, *59* (5), 1635.
- (135) Lewandowska, A. E.; Bañares, M. A.; Khabibulin, D. F.; Lapina, O. B. Precursor Effect on the Molecular Structure, Reactivity, and Stability of Alumina-Supported Vanadia. *J. Phys. Chem. C* **2009**, *113* (48), 20648.
- (136) Carrero, C. A.; Schloegl, R.; Wachs, I. E.; Schomaecker, R. Critical Literature Review of the Kinetics for the Oxidative Dehydrogenation of Propane over Well-Defined Supported Vanadium Oxide Catalysts. **2014**.
- (137) Friedman, J. S. *History of Color Photography*; Joseph Solomon Friedman, 1934.
- (138) Ahmed, I.; Rostom, S.; Lanza, A.; Lasa, H. De. Computational Fluid Dynamics Study of the CREC Riser Simulator : Mixing Patterns . In *Powder Technology*; 2016.
- (139) D'Ippolito, S. A.; Bañares, M. A.; Fierro, J. L. G.; Pieck, C. L. Propane Oxidative Dehydrogenation on V–Sb/ZrO₂ Catalysts. *Catal. Letters* **2008**, *122* (3–4), 252.
- (140) Fabi, L.; Cede, L. V Loading Effect on V₂O₅/ZrO₂ Catalysts for Oxidative Desulfurization. **2011**, 2659.

- (141) Meira, D. M.; Cortez, G. G.; Monteiro, W. R.; Rodrigues, J. A. J. Vanadium Oxides Supported on Hydrotalcite-Type Precursors: The Effect of Acid-Base Properties on the Oxidation of Isopropanol. *Brazilian J. Chem. Eng.* **2006**, *23* (3), 351.
- (142) Kazemeini, M. Physicochemical Properties and Catalytic Performances of Nanostructured V_2O_5 over TiO_2 and $\gamma-Al_2O_3$ for Oxidative Dehydrogenation of Propane. *Chem. Biochem. Eng. Q. J.* **2016**, *30* (1), 9.
- (143) Tonetto, G.; Atias, J.; De Lasa, H. FCC Catalysts with Different Zeolite Crystallite Sizes: Acidity, Structural Properties and Reactivity. *Appl. Catal. A Gen.* **2004**, *270* (1–2), 9.
- (144) W., C. a. Zeolite Characterization and Analysis : A Tutorial. **2009**, 373.
- (145) Khodakov, A.; Olthof, B.; Bell, A. T.; Iglesia, E. Structure and Catalytic Properties of Supported Vanadium Oxides: Support Effects on Oxidative Dehydrogenation Reactions. *J. Catal.* **1999**, *181* (2), 205.
- (146) Pieck, C. L.; Bañares, M. A.; Fierro, J. L. G. Propane Oxidative Dehydrogenation on VO_x/ZrO_2 Catalysts. *J. Catal.* **2004**, *224* (1), 1.
- (147) Naumenko, a P.; Berezovska, N. I.; Biliy, M. M.; Shevchenko, O. V. Vibrational Analysis and Raman Spectra of Tetragonal Zirconia. *Phys. Chem. Solid State* **2008**, *9*, 121.
- (148) Bartholomew, C. . H.; Farrauto, R. J. Fundamentals of Industrial Catalytic Processes, 2nd Edn. *Focus Catal.* **2006**.
- (149) Putra, M. D.; Al-Zahrani, S. M.; Abasaheed, A. E. Kinetics of Oxidehydrogenation of Propane over Alumina-Supported Sr-V-Mo Catalysts. *Catal. Commun.* **2012**, *26*, 98.
- (150) Farjoo, A.; Khorasheh, F.; Niknaddaf, S.; Soltani, M. Kinetic Modeling of Side Reactions in Propane Dehydrogenation over Pt-Sn/ $\gamma-Al_2O_3$ Catalyst. *Sci. Iran.* **2011**, *18* (3), 458.
- (151) Barsan, M. M.; Thyron, F. C. Kinetic Study of Oxidative Dehydrogenation of Propane over Ni-Co Molybdate Catalyst. *Catal. Today* **2003**, *81* (2), 159.

- (152) Chen, K.; Bell, A. T.; Iglesia, E. Kinetics and Mechanism of Oxidative Dehydrogenation of Propane on Vanadium, Molybdenum, and Tungsten Oxides. *J. Phys. Chem. B* **2000**, *104* (6), 1292.
- (153) Islam, M. A.; Krol, S.; De Lasa, H. I. Slip Velocity in Downer Reactors: Drag Coefficient and the Influence of Operational Variables. *Ind. Eng. Chem. Res.* **2010**, *49* (15), 6735.
- (154) Lanza, A.; de Lasa, H. Scaling-up down Flow Reactors. CFPD Simulations and Model Validation. *Comput. Chem. Eng.* **2017**, *101*, 226.
- (155) Snider, D. M.; Clark, S. M.; O'Rourke, P. J. Eulerian-Lagrangian Method for Three-Dimensional Thermal Reacting Flow with Application to Coal Gasifiers. *Chem. Eng. Sci.* **2011**, *66* (6), 1285.
- (156) Snider, D.; Banerjee, S. Heterogeneous Gas Chemistry in the CFPD Eulerian-Lagrangian Numerical Scheme (Ozone Decomposition). *Powder Technol.* **2010**, *199* (1), 100.
- (157) O'Rourke, P. J.; Snider, D. M. An Improved Collision Damping Time for MP-PIC Calculations of Dense Particle Flows with Applications to Polydisperse Sedimenting Beds and Colliding Particle Jets. *Chem. Eng. Sci.* **2010**, *65* (22), 6014.
- (158) O'Rourke, P. J.; Zhao, P. (Pinghua); Snider, D. A Model for Collisional Exchange in Gas/Liquid/Solid Fluidized Beds. *Chem. Eng. Sci.* **2009**, *64* (8), 1784.
- (159) Anderson, T. B.; Jackson, R. Fluid Mechanical Description of Fluidized Beds. Equations of Motion. *Ind. Eng. Chem. Fundam.* **1967**, *6* (4), 527.
- (160) Jackson, R.; Shattuck, M. D. The Dynamics of Fluidized Particles. *Am. J. Phys.* **2001**, *69* (10), 1118.
- (161) O'Rourke, P. Collective Drop Effects on Vaporizing Liquid Sprays, 1981.
- (162) Stairmand, C. J. Design and Performance of Cyclone Separators. *Inst. Chem. Eng. -- Trans.* **1951**, *29* (3), 356.
- (163) Chandimal Bandara, J.; Sørflaten Eikeland, M.; Moldestad, B. M. E. Analyzing the

Effects of Particle Density, Size, Size Distribution and Shape for Minimum Fluidization Velocity with Eulerian-Lagrangian CFD Simulation; 2017; pp 60–65.

- (164) Abbasi, A.; Ege, P. E.; de Lasa, H. I. CPFD Simulation of a Fast Fluidized Bed Steam Coal Gasifier Feeding Section. *Chem. Eng. J.* **2011**, *174* (1), 341.
- (165) Wen, C. Y.; Yu, Y. H. Mechanics of Fluidization. *Chem. Eng. Progress, Symp. Ser.* **1966**, *62* (1), 100.
- (166) Patel, M. K.; Pericleous, K.; Cross, M. Numerical Modelling of Circulating Fluidized Beds. *Int. J. Comput. Fluid Dyn.* **1993**, *1* (2), 161.
- (167) Chhabra, R. P.; Agarwal, L.; Sinha, N. K. Drag on Non-Spherical Particles: An Evaluation of Available Methods. *Powder Technol.* **1999**, *101* (3), 288.
- (168) Wang, Z.; Bai, D.; Jin, Y. Hydrodynamics of Cocurrent Downflow Circulating Fluidized Bed (CDCFB). *Powder Technol.* **1992**, *70* (3), 271.
- (169) Fogler, H. S. Elements of Chemical Reaction Engineering. *Elem. Chem. React. Eng.* **1999**, 646.

9 Appendices

9.1 Appendix A: GC Calibration Curves

In PODH experiments, the possible product gases are CO, CH₄, CO₂, C₂H₄, C₂H₆, C₃H₆ and unconverted C₃H₈. The purpose of the gas calibration is to correlate the component concentration with the GC peak area for each gas. Calibration curves of for each component were carried by a gas chromatograph (Shimadzu GC-2010) (where the carrier gas is Argon) equipped with a methanizer and a packed column HayeSepD 100/120 mesh. The methanizer allows one to detect very low concentrations of carbon monoxide and carbon dioxide. It consists of a flame ionization detector which can detect all hydrocarbons as well as CO and CO₂ and methane. Furthermore, hydrogen is detected by TCD.

The calibration gases used in this study were certified standards of pure gases and gas mixtures. The concentrations of the different certified gas standards used in the calibration are given in Table A. 1.

Table A. 1: Concentrations of calibration gas standards

Standard Gas/Mixture	Concentration
H ₂ , CO, CH ₄ and CO ₂	50% H ₂ , 20% CO, 10% CH ₄ and 20% CO ₂
Ethylene (C ₂ H ₄)	10.2 % C ₂ H ₄ balance with He
Ethane (C ₂ H ₆)	99.99% C ₂ H ₆
Propylene (C ₃ H ₆)	10% C ₃ H ₆ balance with He
Propane (C ₃ H ₈)	99.99% C ₃ H ₈

For each component, different concentration levels were achieved by injecting different volumes of gas/mixture standard using a calibrated gas syringe into the Shimadzu GC-2010 at standard conditions (25°C and 1 atmosphere). Three different concentration levels were considered for each component and each concentration point was repeated three times to secure data reproducibility. Plots of the component's response peak area vs their concentration in micro moles are given in the below Figure A. 1-Figure A. 8.

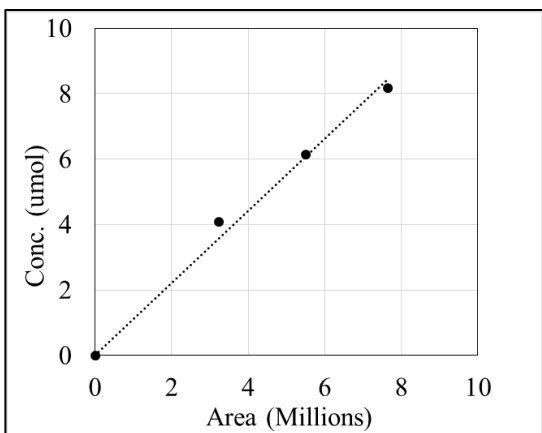


Figure A. 1: Calibration curve for hydrogen.

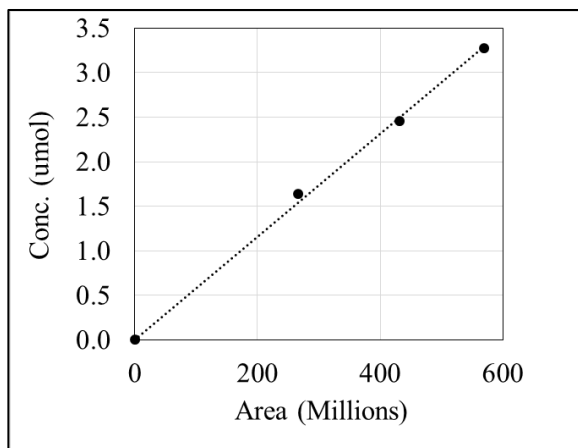


Figure A. 2: Calibration curve for carbon monoxide

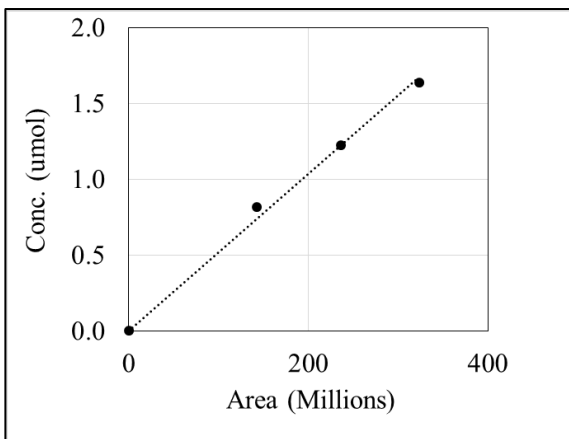


Figure A. 3: Calibration curve for methane

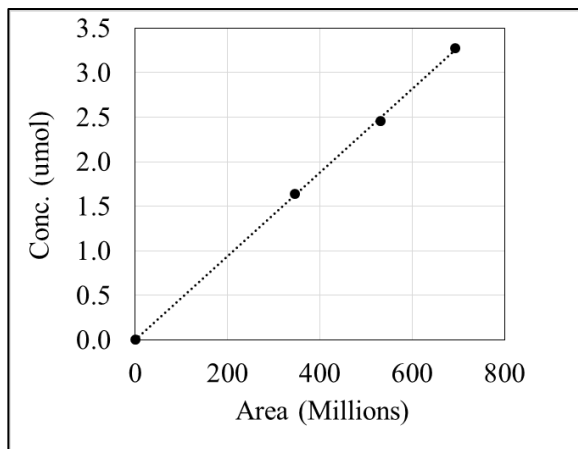


Figure A. 4: Calibration curve for carbon dioxide

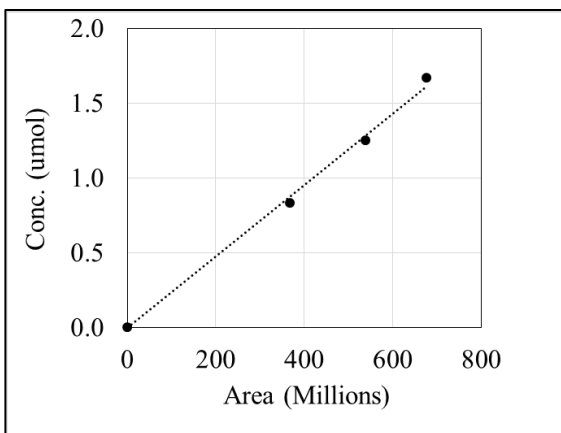


Figure A. 5: Calibration curve for ethylene

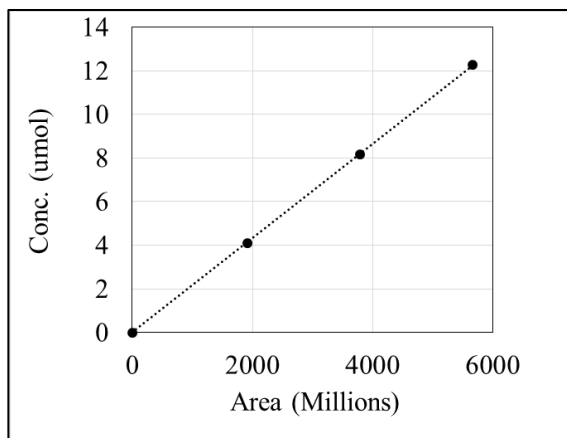


Figure A. 6: Calibration curve for ethane

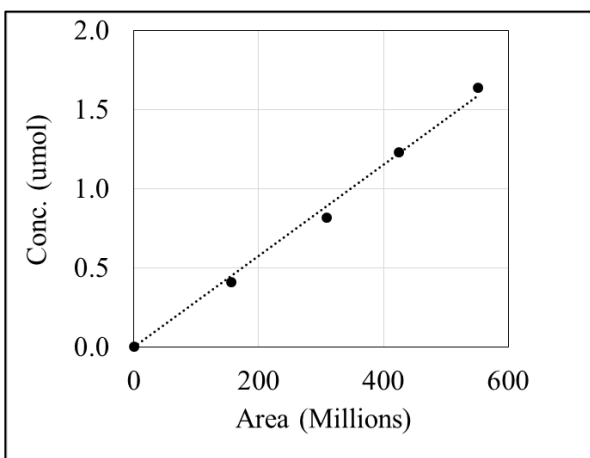


Figure A. 7: Calibration curve for propylene

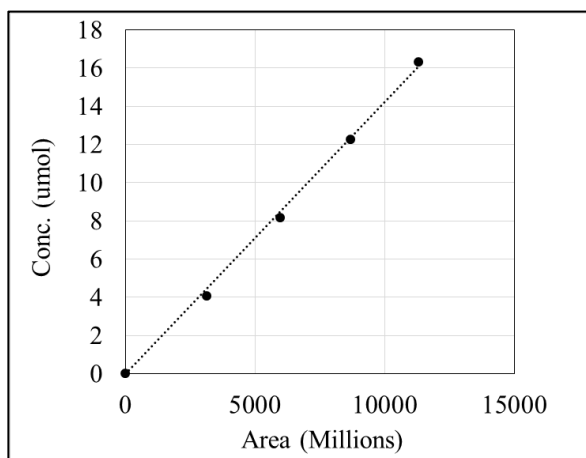


Figure A. 8: Calibration curve for propane

9.2 Appendix B: Conversion and Products Distribution Results

Table B. 1 reports propane conversion and product selectivities for 4 to 10 successive propane injections ODH experiments over 7.5 wt. % vanadium supported on $ZrO_2-\gamma Al_2O_3$ (1:1 wt. %) catalyst at various reaction times and temperatures. One should notice that, only identifiable carbon-containing products other than propylene were CO, CH_4 , CO_2 , C_2H_4 and C_2H_6 .

Table B. 1: Propane conversion and product distribution results for 4 to 10 consecutive propane injections over 7.5V/ $ZrO_2-\gamma Al_2O_3$ (1:1 wt. %) catalyst at different reaction times and temperatures.

Time (s)	Temperature (°C)	Cycle (#)	$X_{C_3H_8}$ (%)	Selectivity (%)					$Y_{C_3H_6}$ (%)
				C_3H_6	CO_x	CH_4	C_2H_4	C_2H_6	
10	500	4	8.68	90.49	7.80	0.91	0.74	0.06	7.80
10	500	5	8.91	90.54	7.64	1.02	0.73	0.07	7.64
10	500	6	8.80	91.39	6.77	1.06	0.71	0.07	8.04
10	500	7	8.68	92.25	5.89	1.10	0.69	0.07	8.01
10	500	8	9.04	91.74	6.37	1.07	0.74	0.08	8.29
10	500	9	8.69	92.25	6.08	0.94	0.67	0.06	8.02
10	500	10	8.52	92.39	5.98	0.90	0.67	0.06	7.88
10	525	4	12.48	90.91	6.43	1.30	1.13	0.21	11.31
10	525	5	12.52	91.00	6.27	1.37	1.15	0.22	11.18
10	525	6	12.36	91.50	5.89	1.40	1.17	0.20	11.31
10	525	7	12.06	91.85	5.39	1.35	1.12	0.19	11.08
10	525	8	12.37	91.60	5.60	1.42	1.29	0.20	11.33
10	525	9	11.88	91.63	5.63	1.36	1.20	0.19	10.89
10	525	10	11.75	91.80	5.50	1.34	1.28	0.18	10.79
10	550	4	16.22	91.34	5.07	1.69	1.53	0.36	14.81
10	550	5	16.09	91.45	4.89	1.72	1.58	0.36	14.71
10	550	6	16.05	91.34	4.99	1.71	1.62	0.35	14.66
10	550	7	15.40	91.50	4.96	1.64	1.58	0.32	14.10
10	550	8	15.51	91.40	4.77	1.74	1.76	0.33	14.18
10	550	9	14.82	91.05	5.23	1.70	1.71	0.31	13.50
10	550	10	14.72	91.15	4.98	1.73	1.83	0.31	13.42
15	500	4	10.46	91.86	6.59	0.82	0.67	0.06	9.61
15	500	5	10.90	92.08	6.31	0.93	0.62	0.08	9.85
15	500	6	10.89	92.85	5.60	0.91	0.59	0.07	10.11
15	500	7	10.85	93.22	5.23	0.93	0.58	0.07	10.11
15	500	8	11.00	92.78	5.67	0.92	0.60	0.06	10.21
15	500	9	10.90	93.66	4.85	0.85	0.61	0.07	10.21
15	500	10	10.70	93.35	5.16	0.87	0.60	0.06	9.99
15	525	4	14.87	92.51	5.25	1.19	0.88	0.18	13.41
15	525	5	14.81	92.43	5.17	1.31	0.91	0.18	13.08
15	525	6	14.88	93.10	4.58	1.27	0.96	0.19	13.85
15	525	7	14.65	93.26	4.34	1.21	0.96	0.18	13.66
15	525	8	14.70	93.24	4.35	1.23	1.03	0.19	13.71
15	525	9	14.25	93.30	4.33	1.21	1.02	0.19	13.30
15	525	10	13.96	93.42	4.30	1.17	1.03	0.17	13.04
15	550	4	21.53	92.45	3.40	2.00	1.59	0.57	19.91
15	550	5	22.11	91.73	3.67	2.20	1.83	0.58	20.28

Time (s)	Temperature (°C)	Cycle (#)	X _{C₃H₈} (%)	Selectivity (%)					Y _{C₃H₆} (%)
				C ₃ H ₆	CO _x	CH ₄	C ₂ H ₄	C ₂ H ₆	
15	550	6	21.98	92.04	3.40	2.16	1.84	0.56	20.23
15	550	7	20.38	91.85	3.76	2.10	1.79	0.50	18.72
15	550	8	19.99	91.65	3.77	2.11	1.99	0.47	18.32
15	550	9	19.28	91.51	3.85	2.15	2.04	0.46	17.64
15	550	10	18.92	91.74	3.77	2.07	1.97	0.45	17.36
20	500	4	12.24	93.24	5.38	0.73	0.60	0.06	11.41
20	500	5	12.88	93.61	4.97	0.83	0.50	0.08	12.06
20	500	6	13.01	94.25	4.45	0.78	0.44	0.08	12.27
20	500	7	13.00	94.16	4.52	0.79	0.46	0.08	12.24
20	500	8	13.00	93.76	4.94	0.77	0.46	0.07	12.19
20	500	9	13.09	95.09	3.52	0.75	0.56	0.08	12.45
20	500	10	12.68	94.23	4.32	0.82	0.54	0.08	11.95
20	525	4	17.25	94.11	4.07	1.07	0.62	0.14	15.51
20	525	5	17.10	93.87	4.07	1.25	0.66	0.15	14.99
20	525	6	17.38	94.69	3.24	1.13	0.76	0.18	16.46
20	525	7	17.21	94.65	3.27	1.10	0.80	0.19	16.29
20	525	8	17.06	94.90	3.09	1.04	0.78	0.19	16.19
20	525	9	16.59	94.92	3.01	1.04	0.84	0.18	15.74
20	525	10	16.10	95.02	3.07	0.98	0.76	0.17	15.30
20	550	4	25.53	93.99	2.95	1.52	1.11	0.44	23.99
20	550	5	25.50	94.53	2.34	1.51	1.17	0.45	24.74
20	550	6	25.70	94.50	2.27	1.52	1.25	0.46	24.47
20	550	7	24.79	94.51	2.31	1.47	1.27	0.44	23.43
20	550	8	24.72	94.35	2.57	1.45	1.23	0.40	23.32
20	550	9	24.70	93.61	2.63	1.71	1.65	0.40	23.21
20	550	10	24.20	93.70	2.67	1.72	1.72	0.38	22.68

9.3 Appendix C: Internal and External Mass Transfer Limitations

The effect of external mass transfer through the gas film surrounding every single particle in downers can be considered negligible while developing a kinetic model, if the following condition is satisfied¹⁶⁹:

$$W_{C_3H_8r} \gg -r_{C_3H_8obs} \quad (78)$$

with $W_{C_3H_8r}$ representing the propane flux across the boundary film surrounding one catalyst and $-r_{C_3H_8obs}$ the observed rate of the PODH reduction reaction.

Regarding the propane flux through the gas film surrounding every particle in the CREC Riser Simulator, it can be calculated using the following mass equation:

$$W_{C_3H_8r} = k_g(C_{C_3H_8b} - C_{C_3H_8s}) \quad (79)$$

with k_g being the mass transfer coefficient; $C_{C_3H_8b}$ the propane concentration in the bulk fluid and $C_{C_3H_8s}$ the propane concentration at the catalyst outer surface.

Furthermore, the k_g mass transfer coefficient can be calculated using the Sherwood number, as follows:

$$Sh = \frac{k_g D'}{D_{AB}} \quad (80)$$

where, D_{AB} represents propane diffusivity in argon, and D' the diameter of the oxygen carrier particle.

This Sh number for a single spherical particle can be established using the Frossling correlation¹⁶⁹:

$$Sh = 2 + 0.6Re^{0.5}Sc^{0.33} \quad (81)$$

where, Re= Reynolds number and Sc= Schmidt number.

However for small 87 micron particles as in the present study and negligible shear stress at the fluid boundary, the Frossling correlation reduces to $Sh = 2$. Thus, one could evaluate Sh or the k_g , should under the worst possible scenario by considering that the fluid surrounding the particles is stagnant.

By combining equations (79) and (80), it gives:

$$W_{C_3H_8r} = \frac{2D_{AB}}{D'} (C_{C_3H_8b} - C_{C_3H_8s}) \quad (82)$$

As well given that the CREC Riser Simulator operates in the batch mode, so the observed rate of reaction can be expressed as:

$$-r_{C_3H_8obs} = \frac{N_{C_3H_80} dX_p}{wS_{ex} dt} \quad (83)$$

where, $N_{C_3H_80}$ = number of moles of propane injected; X_p = conversion of Propane, S_{ex} = external surface area per gram of sample and w = weight of the oxygen carrier sample tested.

Thus, and to perform this evaluation, the various parameters reported in the enclosed Table C. 1 can be used.

Table C. 1: Parameters used to evaluate external mass transfer effect at t=0 s which is the most demanding condition for transport limitations.

D_{AB} (m ² /s)	10 ⁻⁵
D' (μm)	87
$C_{C_3H_8b}$ (mol/m ³)	1.48
$C_{C_3H_8s}$ (mol/m ³)	0
$N_{C_3H_80}$ (mole)	7.4×10 ⁻⁵
$\left. \frac{dX_p}{dt} \right _{t=0}$ (s ⁻¹)	0.0192
w (g)	0.4
S_{ex} (m ² /g)	50
$W_{C_3H_8r}$ (mol/m ² s)	0.34
$-r_{C_3H_8obs}$ (mol/m ² s)	7.1×10 ⁻⁸

From Table C. 1, it can also be observed that, the radial flux of propane through the gas film is 10⁸ times higher than the observed rate of reaction. Thus, this shows that, propane diffusion through the gas film does not limit the overall reduction rate⁵⁷, and can be neglected in the development of the kinetic model.

Additionally, and for assessing potential influence of internal transport limitations, the Weisz-Prater criterion can be used to determine if internal diffusion transport should be considered¹⁶⁹. The Weisz-Prater criterion can be defined as:

$$C_{WP} = \frac{-r'_{C_3H_8obs} \rho_{OC} \left(\frac{D'}{2}\right)^2}{D_{eff} C_{C_3H_8s}} \quad (84)$$

where, ρ_{OC} = oxygen carrier particle density and D_{eff} = effective diffusivity.

One should notice that, if the dimensionless $C_{WP} \ll 1$; then one can discard the internal mass transport diffusion in the development of the kinetic model. Table C. 2 reports the various parameters considered for application of Equation (84).

Table C. 2: Parameters used to evaluate the effect of internal mass transport limitations at $t= 0$ s which is the most demanded condition for transport limitations.

$-r'_{C_3H_8_{obs}}$ (mol/g s)	3.96×10^{-6}
ρ_{OC} (kg/m ³)	1800
$D_{eff} = 0.1D_{AB}$ (m ² /s)	10^{-6}
$C_{C_3H_8s}$ (mol/m ³)	1.48
C_{WP}	9.1×10^{-6}

From the data in Table C. 2, one can observe that, the Weisz-Prater parameter is 10^5 times smaller than 1. Therefore, no internal diffusion transport or significant propane concentration gradients within the oxygen carrier pellet are required to be considered in the kinetic model.

In summary, given the above calculations, both external and internal transport processes can be neglected while developing the kinetic model, then the PODH rates measured in the CREC Riser Simulator represent intrinsic PODH rates.

9.4 Appendix D: Adsorption Constant Calculation

Adsorption tests were performed in the CREC Riser Simulator for individual gases. These tests were done for different temperatures and different contact times. Here, a sample calculation is reported for propane adsorption on 0.40 g γ -Al₂O₃ at 500°C temperature and 15 sec contact time.

Table D. 1 reports the different amount of propane injections and the corresponding coverage on alumina surface.

Table D. 1: Coverage and partial pressure of propane for different amount of feed injections.

Feed	Reactor Pressure during Injection	Corresponding Amount	Reactor Pressure after Injection	Reactor Pressure should be after Injection	Difference at High Temp.	Difference at Room Temp.	Corresponding Amount	Coverage (V)	$P_{C_3H_8}$	1/V	1/ $P_{C_3H_8}$
(ml)	(Psia)	(μmol)	(Psia)	(Psia)	(Psia)	(Psia)	(μmol)	($\mu\text{mol}/g_{\text{cat}}$)	(atm)	($g_{\text{cat}}/\text{mol}$)	(atm^{-1})
3	14.60	121.80	16.56	16.84	0.28	0.11	15.27	38.17	0.152	2.62E+04	6.56
5	14.59	202.86	17.81	18.32	0.51	0.20	27.85	69.62	0.254	1.44E+04	3.94
7	14.60	284.20	18.97	19.83	0.86	0.33	46.68	116.70	0.356	8.57E+03	2.81
10	14.57	405.17	20.78	22.02	1.24	0.48	67.64	169.10	0.507	5.91E+03	1.97

The fraction of the sites occupied by propane is:

$$\theta = \frac{V}{V_m} = \frac{K_{C_3H_8} P_{C_3H_8}}{1 + K_{C_3H_8} P_{C_3H_8}} \dots (85)$$

$$\frac{1}{V} = \frac{1}{K_{C_3H_8} * V_m} * \frac{1}{P_{C_3H_8}} + \frac{1}{V_m} \dots (86)$$

Plotting 1/V vs 1/ $P_{C_3H_8}$ will give a straight line with slope = $\frac{1}{K_{C_3H_8} * V_m}$ and intercept = $\frac{1}{V_m}$

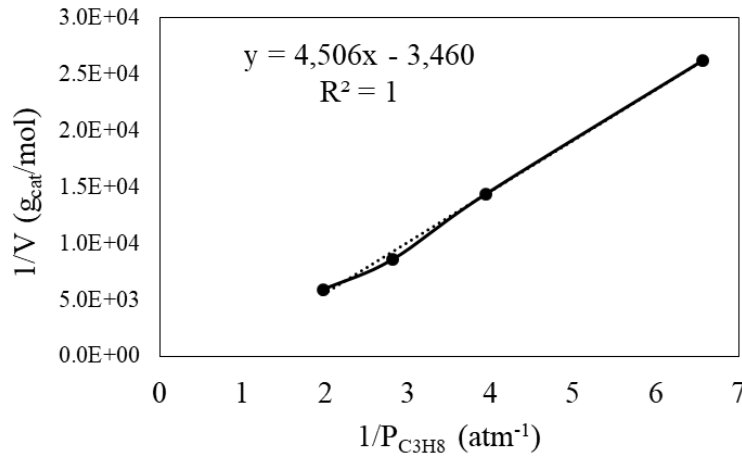


Figure D. 1: 1/V vs 1/ $P_{C_3H_8}$ plot

From Figure D. 1, using slope and intercept, $K_{C_3H_8} = 0.77 \text{ atm}^{-1}$. Adsorption constants for other gases are calculated based on above described method at different temperatures and contact times.

9.5 Appendix E: Grid Discretization Analysis

CPFD modeling in Barracuda 17.3.0 requires a CAD mesh module to be built-in. To establish the adequacy of the selected mesh, a discretization sensibility analysis was performed as follows:

- First, a grid of $13 \times 13 \times 3250$ (549,250) (Mesh 1) cell was used. This grid was chosen given that it provides reasonable grid meshing and fast computational times.
- Following this, a second grid with cell size increased approximatively 1.5 times or $15 \times 15 \times 3750$ (843,750) (Mesh 2) was considered.
- Results of the computations between the smaller grid (Mesh 1) and the larger one (Mesh 2) were compared as reported in Figure E. 1.

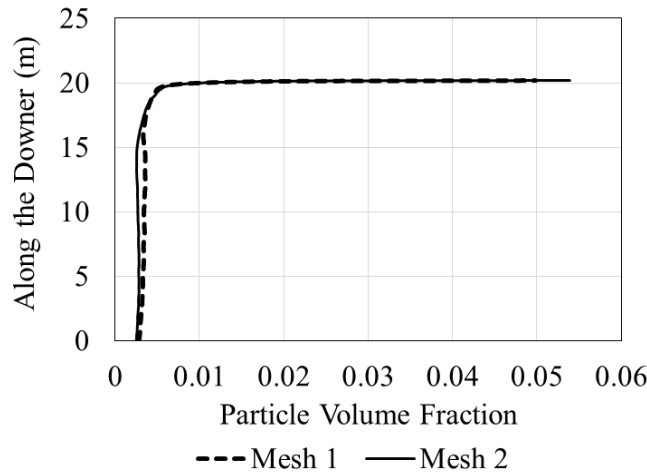


Figure E. 1: Influence of the Grid Size on the Cluster Particle Volume Fraction along the Downer. Comparison effected at the Centre Line of Downer. Simulation Time Step: 0.01s.

Figure E. 1 shows a close Cluster Particle Volume Fraction using Mesh 1 and Mesh 2. Given the essentially identical cluster particle velocity, gas velocity, total pressure and temperature, Mesh 1 with the smaller number of cells (549,250) and with a 0.01 s simulation incremental time interval was selected for the various calculations of the present study.

Furthermore, Figure E. 2 reports the almost identical values for cluster particle velocity, gas velocity, cluster particle volume fraction and temperature observed while analysing the simulation time step effect on the calculated Total Pressure along the downer using 0.01s or 0.005s simulation times. Therefore, the 0.01s simulation time step and the Mesh 1 were selected as they were

determined to be adequate for the various CPFD calculations of the present study.

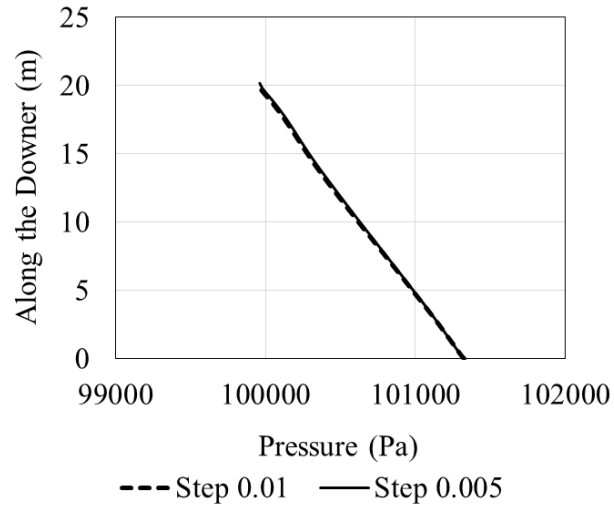


Figure E. 2: Effect of Incremental Simulation Time on the Calculated Total Pressure at the Centre Line along of Downer. Selected Mesh: 549,250 (Mesh 1).

9.6 Appendix F: Gas and Particle Cluster Flow in Entry and Exit Cyclones

As particles circulate between downer reactor and regenerator, they are carried by steam. Thus, before entering the downer section, it is necessary to separate catalyst particles from the steam. With this end, a feeding cyclone was placed on top of the downer reactor. As well, a terminator cyclone was considered at the downer exit to disengage the catalyst particles from the product gases.

Calculations developed are illustrated in Figure F. 1. This figure compares the calculated total gas molar flowrate fed at the inlet and top outlet of the terminator cyclone. As reported at more than 30 s of simulation time, calculations show a 98% gas separation efficiency. As well, for particle flows, 99% particle separation efficiency was observed.

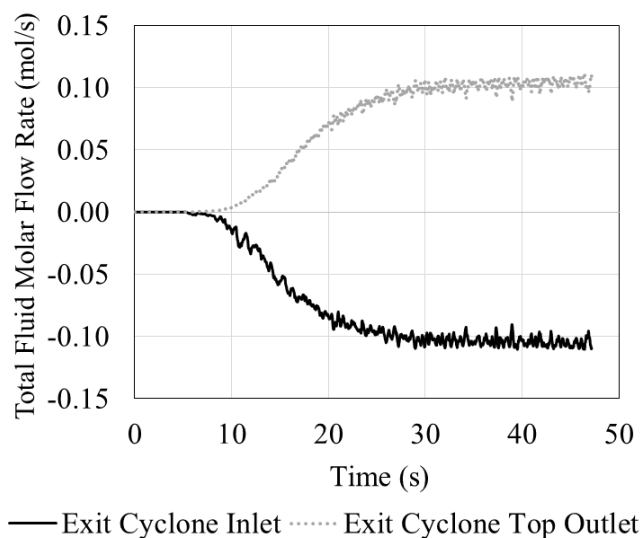


Figure F. 1: Total Fluid Molar Flowrate at the Inlet and Top Outlet of the Terminator Cyclone.

Furthermore, similar calculations were developed for the Feeding Cyclone with particles fed being 0.145 kg/s and the calculated particle flowrate at the cyclone dipleg being 0.143 kg/s. This means that the feeding cyclone displayed a 90% and 99% gas and particle separation efficiency, respectively.

9.7 Appendix G: Copyright/Permission from Journals

- **Rostom, S.; de Lasa, H. I.** Propane Oxidative Dehydrogenation Using Consecutive Feed Injections and Fluidizable $\text{VO}_x/\gamma\text{Al}_2\text{O}_3$ and $\text{VO}_x/\text{ZrO}_2-\gamma\text{Al}_2\text{O}_3$ Catalysts. *Ind. Eng. Chem. Res.* 2017



Title: Propane Oxidative
Dehydrogenation Using
Consecutive Feed Injections and
Fluidizable VOx/ γ Al₂O₃ and
VOx/ZrO₂- γ Al₂O₃ Catalysts

Author: Samira Rostom, Hugo I. de Lasa

Publication: Industrial & Engineering
Chemistry Research

Publisher: American Chemical Society

Date: Nov 1, 2017

Copyright © 2017, American Chemical Society

LOGIN

If you're a **copyright.com**
user, you can login to
RightsLink using your
copyright.com credentials.

Already a **RightsLink user** or
want to [learn more?](#)

PERMISSION/LICENSE IS GRANTED FOR YOUR ORDER AT NO CHARGE

This type of permission/license, instead of the standard Terms & Conditions, is sent to you because no fee is being charged for your order. Please note the following:

- Permission is granted for your request in both print and electronic formats, and translations.
 - If figures and/or tables were requested, they may be adapted or used in part.
 - Please print this page for your records and send a copy of it to your publisher/graduate school.
 - Appropriate credit for the requested material should be given as follows: "Reprinted (adapted) with permission from (COMPLETE REFERENCE CITATION). Copyright (YEAR) American Chemical Society." Insert appropriate information in place of the capitalized words.
 - One-time permission is granted only for the use specified in your request. No additional uses are granted (such as derivative works or other editions). For any other uses, please submit a new request.
-
- **Rostom, S.;** de Lasa, H. I. High Propylene Selectivity via Propane Oxidative Dehydrogenation Using a Novel Fluidizable Catalyst: Kinetic Modeling. Ind. Eng. Chem. Res. 2018



Title: High Propylene Selectivity via Propane Oxidative Dehydrogenation Using a Novel Fluidizable Catalyst: Kinetic Modeling

Author: S. Rostom, H. de Lasa

Publication: Industrial & Engineering Chemistry Research

Publisher: American Chemical Society

Date: Aug 1, 2018

Copyright © 2018, American Chemical Society

LOGIN

If you're a **copyright.com user**, you can login to RightsLink using your copyright.com credentials.

Already a **RightsLink user** or want to [learn more?](#)

PERMISSION/LICENSE IS GRANTED FOR YOUR ORDER AT NO CHARGE

This type of permission/license, instead of the standard Terms & Conditions, is sent to you because no fee is being charged for your order. Please note the following:

- Permission is granted for your request in both print and electronic formats, and translations.
- If figures and/or tables were requested, they may be adapted or used in part.
- Please print this page for your records and send a copy of it to your publisher/graduate school.
- Appropriate credit for the requested material should be given as follows: "Reprinted (adapted) with permission from (COMPLETE REFERENCE CITATION). Copyright (YEAR) American Chemical Society." Insert appropriate information in place of the capitalized words.
- One-time permission is granted only for the use specified in your request. No additional uses are granted (such as derivative works or other editions). For any other uses, please submit a new request.

Curriculum Vitae

SAMIRA ROSTOM

EDUCATION

Ph.D. Candidate in Chemical Engineering

Jan 2015–Nov 2018

University of Western Ontario, London, ON, Canada

- Dissertation: Synthesize a novel fluidizable catalyst to increase propylene production from propane via oxidative dehydrogenation technique in a downer fluidized bed reactor, subsequently develop a kinetic model and analyze industrial scale performance of the catalyst.
- Major Courses: Adv. Chemical Reaction Engineering, Adv. Particle and Fluidization Technology, Chemical Process Safety, Adv. Statistical Process Analysis; Adv. Chemical Engineering Thermodynamics; CGPA: 3.7/4.0

B. Sc. in Chemical Engineering

June 2007–Mar 2012

Bangladesh University of Engineering and Technology (BUET), Dhaka, Bangladesh

CGPA: 3.5/4.0

- Thesis: Design a PID controller accompanied by a data acquisition software to control multiple interacting heating processes using Decoupler technique.
- Project: Construct a heat and mass balance model for crude oil refining process to maximize diesel and kerosene production using Aspen-HYSYS software and design the major infrastructure equipment including PFD and P&ID.
- Co-op Experience: Analyzed daily operations data of the Ammonia and Urea Plant Operation, Karnaphuli Fertilizer Company Limited (KAFCO), Bangladesh.

AWARD

- Western Graduate Research Scholarship; Travel Grant Award for Young Scientist (ISCRE 25 Conference)
 - Bangladesh Government Technical Scholarship
-

WORK EXPERIENCES

Graduate Teaching Assistant | University of Western Ontario, London, ON, Canada

(Sep 2015-Dec 2018)

- Supervised undergraduate students, delivered lectures, conducted tutorials to solve problems, and graded exam papers. Was nominated for Graduate Student TA Award for outstanding teaching contribution.
- Guided several first year engineering students to apply systematic thinking processes and problem solving techniques for validating their engineering projects.

Assistant Manager | Local Sourcing Department | Bata Shoe Company, Bangladesh

(Dec 2013-Nov 2014)

- Conducted market research to identify potential third party contract manufacturers. Conducted on-site visits to determine production capacity and quality control measures. Short-listed candidates for further negotiation.
- Assisted senior management to negotiate production contracts. Developed costing models to determine pricing at different production volumes.
- Evaluated supplier performance through review of reports and customer feedback; coordinated with supplier to remove production bottlenecks and addressed any negative supplier performance.

Senior Officer | Costing & Efficiency Department | Bata Shoe Company, Bangladesh

(May 2012-Nov 2013)

- Coordinated with production manager to determine the machinery capacity and labor productivity of the newly established rubber production factory. Prepared periodic reports on capacity utilization to assist production planning.
- Developed costing models for multiple product lines. Coordinated with production manager and materials purchasing manager to collect reliable data. Prepared and presented variance reports to senior management for ongoing monitoring.
- Assisted the product development team to evaluate chemical processes and formulation of several product lines. Provided chemical engineering knowledge to enhance quality and/or reduce cost of materials.

JOURNAL PUBLICATIONS AND CONFERENCES ATTENDED

- **Rostom, S.;** de Lasa, H. I. High Propylene Selectivity via Propane Oxidative Dehydrogenation Using a Novel Fluidizable Catalyst: Kinetic Modeling. *Ind. Eng. Chem. Res.* 2018
Poster presentation at ISCRE 25 Conference (Florence, Italy, May 20-23, 2018)
- **Rostom, S.;** de Lasa, H. I. Propane Oxidative Dehydrogenation Using Consecutive Feed Injections and Fluidizable $\text{VO}_x/\gamma\text{Al}_2\text{O}_3$ and $\text{VO}_x/\text{ZrO}_2-\gamma\text{Al}_2\text{O}_3$ Catalysts. *Ind. Eng. Chem. Res.* 2017
Oral presentation at 67th CSChE Conference (Edmonton, AB, October 22-25, 2017)
- Ahmed, I.; **Rostom, S.;** Lanza, A.; Lasa, H. de. Computational Fluid Dynamics Study of the CREC Riser Simulator: Mixing Patterns. *Powder Technology.* 2016